Supplementary materials

On the origin and evolution of the asteroid Ryugu: A comprehensive geochemical perspective

Contents

List of Figures

List of Tables

ST1. Supplementary text: Analytical methods

All analyses were undertaken at the Pheasant Memorial Laboratory for Geochemistry and Cosmochemistry (PML), Institute for Planetary Materials, Okayama University at Misasa, Japan, following the procedures outlined by Nakamura et al. [2, 189, 250], and newly developed protocols, especially for the analysis of Ryugu particles.

ST1.1. Density measurement

Density is a fundamental parameter, related to the physical properties and behavior of matter. In particular, it is an essential parameter in the physicochemical interpretation of the macroscopic formation process and subsequent evolution of small solar system bodies and their microscopic chemical evolution in the solar system. The bulk density of materials of extraterrestrial origin has been measured mainly using meteorites [e.g. 30]. However, it is not clear whether meteorites retain the structure of the materials they originated from, due to various processes such as break-up and melting that occur during passage through the Earth's atmosphere and impact with its surface, as well as post-fall alteration. In addition, the original so-called "parent body" of meteorites is completely unknown, therefore, discussing the link between the measured densities and the physical properties of the parent body requires substantial assumptions. In contrast, the samples used in this study were clearly collected from near the surface of the asteroid Ryugu. Thus the result reported here is the bulk density of matter from a primitive body in the solar system, which is extremely important for enabling a more complete understanding the evolutionary process of matter in the solar system. Here, the actual bulk density estimation was examined based on the volumetric measurement of each particle by 3D imaging and the particle weight measurement for each of the 16 particles (20 aliquots). The measurement results of all aliquots are summarized in Table S3.

In order to estimate the porosity (ϕ) of each particle, grain densities (ρ_{grain}), which correspond to only the volume occupied by solid matter, omitting interior cracks and voids, were calculated based on the modal abundance of phases. For this estimation, the density of each phase was assumed based on the typical chemical composition of each particle (Tables S4 and S5). The difference between the bulk and the grain density was assumed to depend entirely on the difference in the porosity of particles. The estimated porosity ranges from 19 to 54 %, and its average is 41 vol% (Table S3). The porosity of a particle is given by the equation,

$$\phi = 1 - \frac{\rho_{bulk}}{\rho_{grain}} \qquad [1]$$

, where ρ_{bulk} is the bulk density of a particle. Although the bulk density of the particles is mainly governed by the volume of void space in the matrix part, the estimated porosity values also depend on uncertainties relating to the parameters, such as the modal abundances and the density variation of each mineral phase.

The accurate density of asteroidal materials is very important to deducing the structure of the asteroid, its dynamics, and the processes surrounding its formation. With the return of samples from the asteroid Ryugu by Hayabusa2, we are now able to directly measure the density of samples from a small-objects surface, which have been under microgravity conditions. Here we describe the results concerning the bulk density measured for the 16 particles we cataloged in the P2C-PML.

To reduce sample contamination as much as possible when measuring particle density, the particle volume was determined from a three-dimensional shape model obtained by non-contact optical profilometry. Particles picked up from the sample container were placed on a clean ceramic plate, and three-dimensional optical images were captured by a digital microscope, OLYMPUS, DSX1000. A ×20 objective lens (WD: 20 mm, NA: 0.4) was used for imaging in dark field mode. The field of view of the ×20 objective lens is 969 μm × 969 μm, and the number of pixels in a single image is 1200 pixel × 1200 pixel, resulting in a resolution of ~0.8 μm per pixel, which is comparable to the theoretical optical resolution. The vertical (z-axis) step size of the focal plane is automatically calculated due to a sample height, and typically is within a the 5–10 μm range. To image the entire particle, multiple images are stitched together to construct a three-dimensional image, then the particle volume was calculated by the analysis application software (DSX-10, Ver. 1.1) provided with the digital microscope. After imaging, the particles were transferred to a clean stainless-steel container and weighed by a precision balance. The particle densities calculated from the particle volumes and weights are shown in Table S3. The frequency distribution of the particles is shown in Fig. 9.

At the P1C, the bulk volume of particles was determined from a spheroid model volume based on optically obtained major and minor Feret diameters, and the thickness of a particle, with a factor (0.928) to correct the irregularity of particle, which was empirically determined 251). In this case, the uncertainty of the factor representing the surface roughness has a very large impact on the particle volume estimate. Although, we estimated bulk volume based on a 3D surface model directory measured with a spatial resolution of 5–10 μm, our method may lead to an overestimation of the bulk volume caused by the irregularity of the optically shaded area of the fragment. Thus, the overestimated error was minimized by placing the sample fragment on the smoothest surface with the largest area, then creating the 3D model. The uncertainty of bulk volume measurement, determined by repeated measurements of the analogue sample, was <10%. As a reference, repeated measurements on the Orgueil (CI1) fragments ($n = 5$) yielded a density of 1650 ± 70 kg/m^3 (1SE), which is consistent with the literature value 29). Therefore, it can be considered that our measurement is more accurate in determining the bulk volume of particles than the density determined by the empirical volume estimate. Nevertheless, we cannot completely rule out the possibility of underestimating the volume.

ST1.2. Textural observation

To elucidate the differences among the aliquots of the 16 Ryugu particles systematically, an aliquot (0.3–2 mm in size) of a given particle was mounted on an indium substrate, and processed to create a planar surface using an ultra-microtome, Leica Microsystems, EM UC7, with a diamond knife, SYNTEC, Sym Knife XAC. The resulting shaving was recovered with a custom-made metal container and used for chemical analysis and spectroscopic analysis. Some of the severely-fragile particles were mounted in an epoxy resin, Struers, SpeciFix-40, and were planned using the ultra-microtome to make a planar surface.

The cross-section created by using the ultra-microtome was smooth enough to perform microscopic observation (Fig. 3). The sectioned solid materials (e.g., coarse-grained silicate minerals) were occasionally striated by the diamond knife (Fig. 3c), and chipped to yield a fish-scale-like texture at the sub-μm scale (e.g., Fig. SA2a). However, the cross-section created by the ultra-microtome, under dry conditions, has the advantages of not removing any soluble materials, and preserving primary internal textures, such as the forms of void space, on the sectioned surface (Fig. 3d).

Both unprocessed and planed surfaces were observed with a digital microscope, OLYMPUS, DSX1000, and a field-emission scanning electron microscope (FE-SEM), JEOL JSM-7001F (Figs. 1, 3, 4, 6, and SA2). The SEM operation was conducted on the non-coated surface, of the particle aliquots, with 10 kV acceleration voltage, 5 nA beam current. The vacuum conditions in the sample chamber were maintained at ~50 Pa in low-vacuum mode and ~10^{-4} Pa in high-vacuum mode. The aliquot mounted in the resin was coated with carbon to give a 6-nm thick coat, and observed in the high-vacuum mode.

To identify mineral phases, semi-quantitative analysis was performed using a FE-SEM, equipped with an energy dispersive X-ray spectrometer (EDS), Oxford, INCA X-act, under conditions of 10 kV acceleration voltage, 5 nA beam current, and 50 seconds integration time.

Raman spectroscopy, XRD analysis (Fig. SA3), and transmission electron microscopy (TEM) (Fig. 4) were also applied to identify mineral phases. The Raman spectroscopy was performed using a Thermo Fisher Scientific, DXR Raman microscope, equipped with a 532-nm Nd-YVO4 laser and a confocal optical microscope. The spectra were collected using a 0.5 mW laser to reduce the degradation of OM in the particle. The XRD patterns were obtained using a microfocus X-ray diffractometer, Rigaku, RINT RAPID II, with a Cu target at an operating voltage of 40 kV, current of 30 mA, a beam diameter of 50–100 μm, and an acquisition time of 10–20 minutes. The nm-scale observation was conducted on an electron transparent film of the particle, which was fabricated by a focused ion beam (FIB) system, JEOL JIB-4500, equipped with a gallium ion gun. The FIB ion milling was performed at an ion beam voltage of 30 kV. Scanning transmission electron microscope (STEM) images and electron diffraction patterns were acquired by using a 200 kV transmission electron microscope, JEOL, JEM-2100F, equipped with an EDS system, JEOL, JED-2300, in standard operational mode. For high-resolution TEM imaging, a high-resolution CCD equipped with an energy filtered imaging system, GATAN, GIF Tridiem 863, was employed.

ST1.3. *In situ* analyses

ST1.3.1. Major and trace elements

Major element abundances (Si, Ti, Al, Cr, Fe, Ni, Mn, Mg, Ca, Na, K, P, and S) in mineral phases were measured by using the FE-SEM-EDS, under conditions of 10 kV acceleration voltage, 5 nA beam current, and 50 seconds integration time for spot analysis, and 20 minutes for elemental mapping; the vacuum conditions were maintained at $\sim 10^{-4}$ Pa in high-vacuum mode. The operation was performed on a non-coated surface for the indium-mounted aliquot, and on a 6-nm thick carbon-coated surface for the resin-mounted aliquot. Integrating spot analysis for individual phases and elemental mapping for an area of 0.01–1.46 mm^2 allowed us to produce a phase-distribution map and estimate the modal abundance of the phases for each particle (Fig. SB). The phase map was constructed by using a public domain image analysis program, Lispix (`https://www.nist.gov/services-resources/software/lispix`). The image resolution of the phase map was estimated to be 0.3–1.6 μm/pixel, indicating that a phase of 1–2 μm can be identified on the phase map.

As for the carbon-coated sample on a resin mount, the measurement was also performed by a field-emission electron probe microanalyzer (FE-EPMA), JEOL, JXA-8530F, with15 kV acceleration voltage and 12 nA beam current. The oxide ZAF method was employed for matrix correction. Natural minerals and a synthetic alloy in ASTIMEX and MINM25-53, were analyzed for calibration.

Trace element abundances (Li, Sr, Y, Zr, Nb, Ba, La, Ce, Pr, Nd, Sm, Eu, Gd, Dy, Er, Yb, and Lu) in the major constituent phases were determined by secondary-ion mass-spectrometry (SIMS; Cameca, ims-5f). Samples were coated with 30-nm gold to avoid the effects of charging. A beam of O^- was used to sputter the samples with a current of 5 nA and an impact energy of -17 keV. Secondary ions were accelerated to +4.5 keV and kinetic energy filtering (-45 eV bias of the sample accelerating voltage) was employed to reduce oxide-ion interferences. The secondary ions were counted using an electron multiplier and magnetic peak jumping. The acquisition time for each spot was 40 minutes, resulting in sputtered craters being approximately 10×15 μm^2 on the sample surface. The ion intensities measured, the yields of metal and oxide ions relative to the reference isotopes, ^{30}Si (for silicate), ^{42}Ca (for carbonate and apatite), ^{26}Mg (for magnesite), and ^{56}Fe (for magnetite and pyrrhotite), and [SiO_2], [CaO], [MgO], and [FeO] that have been determined by SEM-EDS in advance, were used to estimate elemental abundances. The metal and oxide yields were estimated by a series of analyses on in-house reference materials, including homogenized basaltic glass, clinopyroxene, orthopyroxene, plagioclase, and apatite. The reference calcite and pyrrhotite were analyzed to confirm ionization efficiency and mass interferences, compared with the silicate analysis. These reference materials cover a large range of elemental abundances ($0.05\leq$ [CI-chondrite] ≤500), which have been determined by conventional solution analyses with ICP-MS 252). Further details are described by references 189, 252).

Since the size of the target phase was often comparable to or smaller than the SIMS spot size, and closely associated with surrounding phases, the analytical area straddled mineral phases, which yielded mixed compositions corresponding to multiple phases. Thus, the analyses straddled by multiphase except for the phyllosilicate-dominated matrix (mixture of phyllosilicate, Fe-sulfide particle, and OM) and phyllosilicate nodules (interlayered smectite- and serpentine-group minerals), were excluded after reviewing the data. The nodule of magnetite was large enough in size, but [Sr], [Y], and [Zr] in magnetite, and [Nd] and [Sm] besides those elements in Fe-sulfide were overestimated, since significant interferences from molecular ions of Fe-oxide and -sulfide could not be corrected appropriately. Thus, analyses of the elements that could not be corrected were also excluded. The available data are shown in Table S4 and Table S5.

ST1.3.2. Oxygen isotope

The oxygen isotopic compositions of magnetite, dolomite, and olivine grains were determined by SIMS with Cameca ims-1280, using a procedure similar to that described in the literature 28). Polished thick sections of C0008-16 and A0022-15 were coated with 75 nA of Au to avoid charging. At the same surface condition, isotopic compositions were determined relative to that of a working standard (San Carlos olivine). The isotope matrix-effect of minerals were estimated based on analyses of in-house mineral standards (magnetite and dolomite) relative to working standard on a different mount. The magnetite is from Kamaishi, Japan. It was reported that the matrix effect of δ^{18}O varies by ±2–3‰ (2SD) depending on crystal orientation 253). To estimate the mean matrix effects of magnetite accurately, the magnetite was mounted as two grains on a mount and multiple analyses were carried out for each grain. The matrix effect of magnetite on samples were corrected using the average. Analyses of magnetite grains in samples may include variation due to the crystal orientation. Dolomite is from Oujda, Morocco with its chemical composition (Ca : Mg : Fe = 49 : 50 : 1 in mol ratio). Although it was suggested that the matrix effect of δ^{18}O varies according to Fe content 254), the matrix effect of dolomites in samples were corrected using acquisitions on the dolomite only. No matrix effect correction relative to the working standard was applied for olivine.

A Cs^+ primary beam (100 pA) of 20 keV was focused and irradiated on the sample surface without scanning, yielding a typically 3 to 5 μm crater. Secondary O^- was accelerated to −10 kV and a normal incident electron gun was used to compensate positive charging on the sputtered area. To minimize the generation of $^{16}OH^-$ secondary ions, a pressure of less than 1.5×10^{-9} Torr was maintained in the specimen chamber using a cold trap filled with liquid nitrogen. A contrast aperture of 400 μm was used and an optical gate of $3000 \times 3000\ \mu m^2$, which corresponds to $23 \times 23\ \mu m^2$ on the sample surface, was inserted and an energy bandpass was set from −10 to 40 eV. The mass-resolution was set to 7000 for $^{17}O^-$ and 2400 for $^{16}O^-$ and $^{18}O^-$. The contribution of $^{16}OH^-$ to the $^{17}O^-$ signal is expected to be non-negligible. By scanning the low-mass side of the $^{16}O^-$ peak, we estimated the ratio of the counts of the low-mass tail to the counts of the peak. At the end of each analysis, the $^{16}OH^-$ signal was measured automatically by deflecting the beam into an axial EM using the DSP2-X deflector. The contribution of the hydride tail to the $^{17}O^-$ signal was estimated based on the established ratio and typically a correction of 0.2‰ (and at most 0.9‰) was applied. The pre-sputtering time, including auto peak-centering, was 190 seconds. Signal intensities were simultaneously determined by a Faraday cup mounted on trolley L2 ($^{16}O^-$) and pulse counting was done using electron multipliers located on axial ($^{17}O^-$) and trolley H1 ($^{18}O^-$). Typical ion intensities for $^{16}O^-$, $^{17}O^-$, and $^{18}O^-$ were 50 M, 20 k, and 100 k cps, respectively. The ion-integration times were 14.5 seconds in each cycle, and each run consisted of 40 cycles. Typical external precision, estimated by repeated analyses of a working standard, was 0.3‰ (1SD) for both $\delta^{18}O$ and $\delta^{17}O$.

ST1.3.3. Carbon and N isotopes

The spatial distribution of C and N isotopic compositions in the matrices was determined by SIMS with Cameca ims-1280. An aliquot with a plane created by the ultra-microtome technique was embedded in an indium pool and was coated with 75 nA of Au to avoid charging (A0073-5, A0078-12, A0085-1, C0019-10, and C0053-1). A Cs^+ primary beam (100 pA) of 20 keV was focused and the surface of the chunk with scanning area of $15 \times 15\ \mu m^2$ (or $50 \times 50\ \mu m^2$) was irradiated. Secondary $^{12}C^{12}C^-$, $^{12}C^{14}N^-$, $^{12}C^{15}N^-$, $^{13}C^{14}N^-$ and $^{28}Si^-$ were accelerated to −10 kV and a normal incident electron gun was used to compensate for positive charging of the sputtered area. A contrast aperture of 400 μm was used and an optical gate of $3000 \times 3000\ \mu m^2$, which corresponds to $23 \times 23\ \mu m^2$ on the sample surface, was inserted and an energy bandpass set from −10 to 40 eV. The mass-resolution was set to 13500 to separate $^{12}C^{15}N^-$ and $^{13}C^{14}N^-$, and to exclude interference from $^{11}B^{16}O^-$. The pre-sputtering time, including auto B-field-centering, was set to 20 minutes (or 150 minutes for $50 \times 50\ \mu m^2$ area) to let the ion intensity ratio, $^{12}C^{14}N^-/^{12}C^{12}C^-$, reach a plateau. Signal intensities were determined by peak jumping with imaging mode using the axial EM. Carbon and nitrogen isotopic compositions ($\delta^{13}C$ and $\delta^{15}N$) were determined from ion intensity ratios, $^{13}C^{14}N^-/^{12}C^{14}N^-$ and $^{12}C^{15}N^-/^{12}C^{14}N^-$, respectively. The N to C molar ratio (N/C) was determined by the ion intensity ratio, $^{12}C^{14}N^-/^{12}C^{12}C^-$. Matrix effects for C and N isotopic compositions and N/C were estimated by comparison to whole rock analyses (Table S14). Multiple areas were probed on each sample and matrix effects were estimated so that average values meet whole-rock values. Two particles (A0085-1 and C0053-1) lack whole rock analyses. The matrix effects were estimated from that of the other samples analyzed in the same session.

Ion maps are processed in two algorithms so that both whole area analysis and pixel-by-pixel analysis were carried out from a single acquisition. Area analysis discards two-dimensional information. Ions detected on an ion map by a cycle are accumulated to generate an ion intensity. Isotopic composition and N/C are estimated by the average of ion-intensity ratios of all cycles. Pixel-by-pixel analysis discards cycle-to-cycle information. Ions detected on maps by cycles are accumulated by each pixel to generate an ion-intensity map. The isotopic composition and N/C are estimated by two ion-intensity maps. Ion maps obtained from 15 μm × 15 μm (or 50 μm × 50 μm) consist of 32 pixel × 32 pixel (or 64 pixel × 64 pixel) thus the dimension of the pixel is 0.5 μm (or 0.8 μm), respectively. The primary beam diameter is estimated to be 1 μm. Thus, actual spatial resolution of pixel-by-pixel analysis is ~1 μm.

The matrix effect correction was carried out so that the average C and N isotopic compositions of the matrix region determined by SIMS are equal to those determined by the whole-rock compositions for each particle. In cases of A0085-1 and C0053-1, which lacked whole-rock C and N isotopic compositions, the matrix effect was estimated to be identical to those for particles analyzed in the same session. The uncertainties associated with the correction are dominated by the counting statistics in the SIMS analysis. In the case of A0085-1 and C0053-1, which are the smallest and the largest total numbers of analyses, the statistic errors deriving from counting were ~2.9 and ~0.6‰ (1SE) for δ^{13}C value and ~4.0 and 0.8‰ (1SE) for δ^{15}N value, respectively.

ST1.3.4. Hydrogen, Li, and B isotopes

The spatial distribution of H, Li, and B in the matrices were also determined by SIMS with Cameca ims-1280. Areas probed for aliquots (C0053-1, C0019-10, A0078-12, and A0073-5) for carbon and nitrogen that includes OM were re-probed in two sessions. In the first session, hydrogen isotopic compositions were determined. The aliquots were loaded into a vacuum chamber and heated to 110°C for more than 16 hours. A Cs^+ primary beam (100 pA) of 20 keV was focused and the surface of the aliquot irradiated with a scanning area of 20 × 20 μm^2. Secondary $^1H^-$, $^2H^-$, and $^{13}C^-$ were accelerated to −10 kV and a normal incident electron gun was used to compensate positive charging on the sputtered area. A contrast aperture of 400 μm was used and an optical gate of 3000 × 3000 μm^2, which corresponds to 23 × 23 μm^2 on the sample surface, was inserted and an energy bandpass was set from −10 to 40 eV. The mass resolution was set to 1800 to exclude $^1H_2^-$ interference. The pre-sputtering time, including auto peak-centering and auto B-field-centering, was set to 7 minutes. Signal intensities were determined by peak jumping with imaging mode using the axial EM. The isotope matrix effects for δ^2H were estimated by analyzing an in-house standard (serpentine) in the same analytical session. In the second session, Li and B isotopic compositions were determined. An O^- primary beam (100 pA) of 23 keV was focused and irradiated on the surface of the aliquot with a scanning area of 20 × 20 μm^2. Secondary $^6Li^+$, $^7Li^+$, $^{10}B^+$, $^{11}B^+$, $^{12}C^+$, and $^{28}Si^+$ were accelerated to −10 kV. A contrast aperture of 400 μm was used and an optical gate of 5000 × 5000 μm^2, which corresponds to 38 × 38 μm^2 on the sample surface, was inserted and an energy band pass was set from −10 to 40 eV. The mass-resolution was set to 1200 to exclude $^6LiH^+$ and $^{10}BH^+$ Interferences. The pre-sputtering time, including auto B-field-centering, was set to 6 minutes. Signal intensities were determined by peak jumping with imaging mode using the axial EM. The isotope matrix effects for δ^7Li and δ^{11}B were estimated by analyzing an in-house standard (basaltic glass) in the same analytical session.

ST1.3.5. Chromium isotope and ^{53}Mn-^{53}Cr *chronology*

Chromium isotopic composition and $^{55}Mn/^{52}Cr$ were determined for dolomites in A0022-15, A0033-15, and C0008-16 by SIMS with Cameca ims-1280. A 13 keV $^{16}O^-$ beam was focused to yield a spot-size of ~3 μm in diameter using a current of 100 pA. The positive secondary ions were accelerated with 10 kV. A contrast aperture of 400 μm was used and an optical gate of 3000 × 3000 μm^2, which corresponds to 23 × 23 μm^2 on the sample surface, was inserted and an energy bandpass was set from −10 to 40 eV. Secondary ions were collected by the axial EM by peak-jumping. Counting time for $^{43}Ca^+$, $^{52}Cr^+$, $^{53}Cr^+$, and $^{55}Mn^+$ were 1, 10, 30, and 3 seconds, respectively, in each cycle. The mass resolving power was set to 7000 to exclude the contribution of the interfering species $^{52}CrH^+$ from $^{53}Cr^+$. The analysis area was pre-sputtered using a focused beam for 10 minutes with a scanning area of 5 × 5 μm^2, after which isotopic measurement was carried out over 200 cycles (2 hours) without scanning. The Cr count rate often showed a rapid increase during an acquisition because of the sputtering of inclusions which had shown up during an acquisition. Ion signals in such cycles were not included in data reduction.

The Cr isotopic composition and $^{55}Mn/^{52}Cr$ were estimated using a total-counts algorithm to minimize a positive bias during low ion-intensity analysis 255). The measured $^{53}Cr^+/^{52}Cr^+$ were corrected for instrumental mass fractionation determined by repeated analyses of the synthesized Cr carbonate, which is assumed to have a terrestrial $^{53}Cr/^{52}Cr$ of 0.113459 256). The relative sensitivity factor [RSF ≡ ($^{55}Mn^+/^{52}Cr^+$)/($^{55}Mn/^{52}Cr$)] was estimated from repeated analyses on the

Cr-bearing Ca carbonate synthesized for this study, following the method in the literature [257]. The Mn/Cr in the vicinity of the individual SIMS analysis spots on the Cr-bearing Ca carbonate were determined using FE-EPMA, JEOL, JXA-8530F. The analytical conditions were 15 kV acceleration voltage, 12 nA beam current and a defocused 10 μm beam to reduce beam damage. The RSF was estimated to be 0.829 (± 0.045, 1SD). The ^{55}Mn/^{52}Cr was estimated using ^{55}Mn$^+$/^{52}Cr$^+$ and the RSF before and after the analytical session. The RSF may include a systematic error because of the lack of dolomite standards [258]. The reported uncertainty in both Cr isotopic composition and ^{55}Mn/^{52}Cr was estimated from counting statistics.

ST1.3.6. Organic matter

Raman spectroscopy is sensitive to the nature of the carbon bonds within organic materials. Two main vibrational modes are present within disorganized carbonaceous materials, such as those within primitive extraterrestrial samples [67]. The G band is related to the relative movement of SP^2 pairs in carbon-carbon bonds and can occur in aromatic and aliphatic material alike, but is known for its strong response in graphitic materials, hence the name graphite or G band. Meanwhile, the D band arises only from aromatic rings that are either bound to aliphatic material or contain heteroatoms, hence the name disorder or D band. As such aromatic rich OM tends to give a strong G and D band during Raman spectroscopic analysis [70]. Fundamental parameters relating to the G and D band, such as the G/D, peak width or peak center position, can be used to tell important information about the type of carbon bonding present in OM. For example, if OM has been heated or irradiated the G/D ratio and the peak positions and widths will change and the changes will be different for these two processes [68]. In particular, confocal Raman micro-spectroscopy is an important technique for the non-destructive evaluation of the properties of organic materials in samples at μm-level spatial resolution. Taking advantage of this feature, a two-dimensional Raman analysis was performed on the 16 Ryugu particles to describe the characteristics of their OM.

2D Raman spectral analyses for surfaces of aliquots of every Ryugu particle were made. Raman data were acquired using a Thermo Fisher Scientific DXR confocal micro-Raman spectrometer with a 532 nm laser. In order to obtain a spectrograph, a 900 lines/mm grating and 50 μm pinhole aperture were used, and 5.4–8.3 cm^{-1} of spectral resolution in 53 to 3500 cm^{-1} range was obtained. A 5 or 10 μm-step stage scan mode was applied to acquire spectrum for 2D-areas, and the typical analytical area for a single analysis was ~10000 μm^2 on a microtomed surface, except for A0033. In the case of the A0033, a microtomed aliquot was not available, so the measurement was performed on a near-flat fracture surface. The spectrum of each analytical point was taken at 0.5 mW laser power and 60 seconds of integration, where the intensity and characteristics of the G and D bands did not change during analysis based on preliminary experiments with the Orgueil meteorite. About 0.7 μm of spatial resolution was theoretically expected by using a ×50 objective lens. Data was collected using OMNIC 9 software, then data processing was conducted using the "hyperspec" package on R. Baseline corrections were made applying a fifth-order polynomial fitting to the obtained spectra in the 1000–1800 cm^{-1} range to evaluate G and D band signatures.

After the baseline correction, the D and G band were fitted using a combination of one Lorentzian and one Breit-Wigner-Fano (BWF) functions to account for the composite nature of the D-bands and G-band, respectively. The Lorentzian spectra is given by;

$$I_{Lorenz}(\omega_s) = I_D \frac{\Gamma_D/(2*\pi)}{(\omega_s - \omega_D)^2 + (\Gamma_D/2)^2} \qquad [2]$$

Here ω_s, ω_D, Γ_D, and I_D are the Raman shift, the spectral peak position of composite D-bands, the spectral width, and the maximum intensity of the Lorenzian spectra.

The BWF spectra is given by;

$$I_{BWF}(\omega_s) = I_G\left[\frac{1}{q_{BWF}^2} + \frac{1 - 1/q_{BWF}^2}{1 + s^2} + \frac{2s/q_{BWF}}{1 + s^2}\right] \quad [3]$$

, where $s = (\omega_s - \omega_G)/\Gamma_G$. Here ω_s, ω_G, $1/\mathrm{q}_{BWF}$, Γ_G, and I_G are the Raman shift, the spectral peak position, the asymmetric factor, the spectral width (FMWD: the full width of half maximum), and the maximum intensity of the BWF spectra, respectively 259).

ST1.3.7. Soluble organic matter

In situ analysis of SOM was performed by using a Desorption Electrospray Ionization-Orbitrap-Mass spectrometry (DESI-OT-MS). The analytical procedure of DESI-OT-MS was modified after Potiszil et al. 78). The C0008 Ryugu particle and an interior fragment of the Orgueil (CI1) chondrite were chipped to expose a new surface. The chipped samples were then placed into a crater on top of a mound of indium within an aluminum holder. The indium was then pressed round the base of the chips to fix them in place. The particles had been kept under a nitrogen atmosphere in the ultimate clean room set-up for the Ryugu particles before and after the sample preparation.

For DESI-OT-MS analysis was performed using a DESI apparatus (Prosolia Inc.) attached to an Orbitrap Fusion Mass Spectrometer (Thermo Fisher Scientific) applying the following parameters: a custom 10 μm ID capillary emitter, 74° emitter angle, 1 μL/minute MeOH solvent flow rate, the distance between the emitter and inlet ion transfer tube of ~0.5 mm, the distance between the emitter and sample surface of ~1 mm, 0.45 mPa N_2 gas pressure, a scan rate of 31.06 μm/s (x axis) and a step size of 10 μm (y axis). The resulting spatial resolution was $10 \times 10\ \mu\mathrm{m}^2$, which is much better than the previous study ($50 \times 50\ \mu\mathrm{m}^2$) 78).

The DESI-OT-MS data were examined for the surface of the C0008-15, A0048-10 and Orgueil samples, and the data reduction was performed using the MSiReader software (`https://msireader.wordpress.ncsu.edu/`) to search for patterns indicative of an indigenous compound. Once a list of ion masses had been generated, the corresponding ion intensity maps from the blank (a serpentinite chip placed in the same holder as the sample) were extracted to allow an assessment of any terrestrial contamination induced during the sample preparation and analytical procedures.

ST1.4. Bulk analyses

Elemental abundances of up to 70 elements and isotopic compositions of up to 8 elements were determined from up to 11 different aliquots (session I to XI) for each particle, which are:

I : [Li], [Be], [Na], [Mg], [Al], [Si], [P], [K], [Ca], [Sc], [V], [Mn], [Fe], [Co], [Ni], [Cu], [Zn], [Ga], [Rb], [Sr], [Y], [Cd], [In], [Cs], [Ba], [La], [Ce], [Pr], [Nd], [Sm], [Eu], [Gd], [Tb], [Dy], [Ho], [Er], [Tm], [Yb], [Lu], [Tl], [Pb], [Bi], [Th], and [U]
II: [B], [Ti], [Zr], [Nb], [Mo], [Sn], [Sb], [Hf], [Ta], and [W]
III: [Cr] and [S]
IV: [Ru], [Pd], [Re], [Os], [Ir], and [Pt] and $^{187}\mathrm{Os}/^{188}\mathrm{Os}$
V: [Ge], [As], [Se], and [Te]
VI: $\delta^{48}\mathrm{Ca}$ and $\delta^{54}\mathrm{Cr}$
VII: [H] and $\delta\mathrm{D}$
VIII: $[\mathrm{C}]_{\mathrm{TC}}$, [N], $\delta^{13}\mathrm{C}_{\mathrm{TC}}$, and $\delta^{15}\mathrm{N}$
IX: $[\mathrm{C}]_{\mathrm{TOC}}$ and $\delta^{13}\mathrm{C}_{\mathrm{TOC}}$
X: $\delta^{17}\mathrm{O}$ and $\delta^{18}\mathrm{O}$
XI: [Ne], $^{20}\mathrm{Ne}/^{22}\mathrm{Ne}$, and $^{21}\mathrm{Ne}/^{22}\mathrm{Ne}$.

The [Si] was calculated by applying the [Mg] determined by ICP-MS to the correlation factor between [Mg] and [Si] determined by SEM-EDS analysis. Sample preparation for all particles and chemical and isotopic analyses for aliquots I to VI were carried out at a clean room for chemistry (measured class: ISO 5) described in the literature 250), analysis of aliquots VII to X in a stable isotope laboratory 201), and aliquot XI in a noble gas laboratory. Details of the reagents, standards, and spikes used in this study can be found in the literature 250) and in the papers on the analytical methods listed below, except for 60% $HClO_4$ (Ultrapure, Kanto Kagaku, Japan) used in this study. Where synthetic solutions were used as standard materials for analyses, mono-element standard solution (for JCSS chemical analysis, for atomic absorption spectrometry and ICP analysis, Kanto Kagaku, Japan) or Plasma standard solution (Specpure®, Alfa Aesar, Lancashire, UK) were gravimetrically mixed.

ST1.4.1. Sample preparation and weighing for inorganic chemistry

Sample aliquots were prepared as either ultra-microtomed ("m" in Table S11) or hand-picked ("h" in Table S11). The ultra-microtome aliquots were cut from the indium-fixed particle or fragment, collected directly into a custom-made metal container set on the cutting knife, and weighed together with the container. The cut surfaces were used for inorganic *in situ* analysis by SEM-EDS and SIMS, and/or for organic *in situ* analysis by Raman and others and so on. When the hand-picked aliquots, fragments of the particle were transferred directly from the container to a stainless-steel cup or pan using stainless-steel tweezers and weighed with the cup/pan. The weighed aliquots were immediately placed in 7 mL round-bottom PFA vials (Savillex) pre-filled with liquid (0.1 mL of further deionized milli-Q© water (USQ), or mannitol solution) for sessions I to VI, Ag capsules for VII, Sn foil for VIII and IX, and Ni capsules for X and XI.

As well as Ryugu particles, Orgueil (CI1) prepared as ultra-microtomed or hand-picked (0.5–0.1 mg each) or powdered (1–2 mg) from small fragments after removal of the fusion crust, and 1–9 mg of Smithsonian Allende powder (CV3, USNM 3529) were also analyzed along with the Ryugu particles in sessions I to V (Tables S11 and S12) .

A maximum of about 3 mg was used to determine all the data; 70 elemental abundances and 8 isotopic compositions from individual Ryugu particles. The total amount used in the destructive analysis of all 16 particles was 25.63 mg (Table S11). The analysis of 66 elements (I-V) was performed on particles around 1 mg in total (e.g., A0022, A0033, A0048, C0008, C0019 and C0079 in Table S12). An average of 0.2 mg (0.05–0.4 mg) was used for the analysis of each aliquot (Table S11). The systematic error in weighing was less than 0.002 mg, and the resulting weighted error is considered to be 0.4–4% (1% on average).

The hand-picked fragments were fragile and they autobreaked up immediately when placed in a vial of liquid after weighing. The phyllosilicates that constitute the matrix may be bound together by water-soluble organic materials. Sub-aliquots were separated from several aliquots used in the session I and confirmed by SEM-EDS, no digestion residues were observed. Each individual Ryugu aliquot was basically analyzed only once due to the limited volume of the analytical solution. Repeated analyses of individual Orgueil aliquot gave an analytical reproducibility about 3% for major elemental abundances, and about 5% for trace element abundances, except relatively lower concentration trace elements such as [B], [Mo], [Sb], [W], [Re] and [U] (10–20%).

Duplicate analyses of C0053 (C0053-F1 and -F2, analysis-I in Table S12) yielded 5–50% differences in elemental abundances, some of which exceed the reproducibility obtained from repeated analyses of individual Orgueil aliquots. The analytical variation of elemental abundances in Orgueil (1σ% in Table S12, number of analyzed aliquots and their total weight in Table S11) obtained by the small sample-size analysis as well as the ultra-microtomed and hand-picked Ryugu particles did not correlate with the counting statistics during ICP-MS analysis. In addition, analysis of small amounts of Smithsonian Allende showed inconsistencies with [Bi] and [Tl] reference values, suggesting sample heterogeneity due to small sample digestions (4–7 mg), despite the use of powder samples, however analysis using samples larger than 10 mg showed [Tl] and [Bi] of 0.0561 and 0.0446 g g^{-1}, respectively ($n = 4$), which matched within 7% of the reference values. This suggests that heterogeneity in phase distribution in a sample shown by the petrographic observation (e.g., high or low carbonate mode abundance), affects the variability of analytical error not only among16 particles, but also in individual aliquots.

[In] of the ultra-microtomed aliquots was not determined. This is because indium is used for sample fixation in the ultra-microtome work, and contamination of the sample with indium was unavoidable and not constant in the preliminary tests. However, it was also confirmed that the contamination of indium did not affect the other elements. The results of the hand-picked aliquots showed a large variation in [In]. Since the initial preparation was proceeded at the same place as the fixation of indium, although at different times, the possibility of contamination cannot be excluded. Therefore, the correlations between [In] and [Fe], [S] and [Cd] were investigated based on the FeS being the main phase of indium during condensation from solar gas 44). The data were examined carefully, and [In] from A0022, and C0008, C0027, and C0053 were applied in bulk [In] calculations in TD1 and TD2, respectively. [Ta] in C0019 and C0081 is an order of magnitude higher than in the other particles, suggesting the contamination by the tantalum projectile used at the time of touch-down during the sampling operation 260). [Ta] data reduction was performed based on the correlation of [Ta] with [Ti] and [Nb], and the bulk [Ta] in TD1 was calculated using data from A0033, A0048, and A0078, and in TD2 using data from C0008, C0027, C0053, C0079, and C0082. In contrast, the influence of the Cu used in the Small Carry-on Impactor (SCI) 261) was not identified by the [Cu] of particles.

ST1.4.2. I: Major, minor & trace elements

After adding the ^{149}Sm-enriched spikes, the aliquot was digested with 0.1 mL of 60% $HClO_4$ and twice distilled (2D) 30M HF at 120°C for more than 12 hours 262). The solution was dried stepwise at 90, 120, and 140°C. The dried aliquot was heated with the mixture of 0.1 mL of 60% $HClO_4$, 0.1 mL of once distilled (1D) 6M HCl, and 0.05 ml of 1D 16M HNO_3 for >12 hours, then dried stepwise to >140°C to achieve complete dryness. Following that, 0.1 mL of 1D 6M HCl was added to the aliquot and dried again at 110°C, then dissolved in 0.5M HNO_3 to make the solution up to a dilution factor (DF) of 2000. To minimize the contamination, a closed evaporation apparatus named "MUKADE" 250) was used for all drying procedures.

The abundances of 28 trace elements (Li, Be, Rb, Sr, Y, Cd, In, Cs, Ba, REE, Tl, Pb, Bi, Th and U) were determined by ICP-QMS (Thermo Fisher Scientific iCAP TQ) using aliquots adjusted to DF2000. JB3 (Geochemical Reference Samples of The Geological Survey of Japan (GSJ)) adjusted to DF2000 after decomposition and a mixed standard solution of In, Cd, Sm, Tl, and Bi were repeatedly measured with every single sample. [Sm] was determined by the isotope dilution method (ID), and other trace element abundances were determined by the Sm internal standardization method (Sm-IS) following the literature 263). JB3 was used as an analytical standard for mass discrimination of Sm isotopic compositions, correction of intensity drift during analysis, and determination of elemental abundances except for [In], [Cd], [Tl], and [Bi]. The mixed standard solution was used as an analytical standard for the determination of [In], [Cd], [Tl], and [Bi].

The 15 major and minor element abundances (Na, Mg, Al, P, K, Ca, Sc, V, Mn, Fe, Co, Ni, Cu, Zn, Ga) were determined by ICP-SFMS (Thermo Fisher Scientific ELEMENT XR), applying the Sr-IS method after analysis of the trace elements 263). Standard solutions of 17 elements (Na, Mg, Al, P, K, Ca, Sc, V, Mn, Fe, Co, Ni, Cu, Zn, Ga, Sr and Sm) were mixed, and 2 solutions with different dilutions were used as analytical standards, and these were repeatedly measured for every 2 samples. During the measurement, the most suitable detector mode (pulse counting, analog counting, or Faraday cup) was automatically selected according to the ionic intensity of the analytes. Although the sensitivity difference between detectors was corrected by applying a predetermined conversion factor, it was insufficient (difference of 5% or more) and caused inferior measurement reproducibility. To eliminate this effect, and because there were large differences in the major and minor element abundances in the samples, the data counted in the same detector mode (pulse counting mode) from 4 combinations of 2 aliquots with different dilution factors and 2 standards as well were selected and used for elemental abundance determination. As a result, the measurement results of DF200000 solution for [Mg] and [Fe], DF20000 solution for [K], and both dilutions for other elements were used.

The [Si] was determined using SEM-EDS elemental mapping of the entire particle cross-section, prepared using an ultra-microtome, and the [Mg] determined by ICP-MS analysis. Phase analysis by SEM-EDS shows that the major phase in the particles is phyllosilicate within the matrix (Fig. 2), which correlates with [Si] and [Mg]. On the other hand, the other accessory phases either do not correlate with [Si] and [Mg] (e.g. Mg can be a main component of carbonates, but Si is not) or do not have any effect due to their small modal abundances. As can be recognized from the petrography, the particle is a complex and fine-fibrous or -grained assemblage (Fig. 5), and it is extremely difficult to separate and analyze them as a single phase. Therefore, instead, the [Si] was obtained from the bulk surface mapping results by excluding the Mg contribution of the accessory phase to improve the precision of the Mg-Si fitting. In practice, the oxygen as the atomic ratio was first corrected using the map analysis results obtained as molar ratios of 15 elements (C, O, Na, Mg, Al, Si, P, S, K, Ca, Ti, Cr, Mn, Fe, and Ni). Since all cations are given as oxides, the Fe/S value obtained by the spot analyses of sulfides was applied to exclude the oxygen assigned as SO_3 and FeO from the corresponding sulfides. The Ca in phosphates were then subtracted from the total Ca using the Ca/P value obtained from the spot analyses of phosphates, assuming that all phosphorus is a component of phosphates. The Mg/Ca value of carbonate (dolomite) was then applied to exclude the Mg in carbonate from the remaining Ca. Finally, the correlation coefficients between Si and Mg were obtained by recalculating the bulk mapping data corrected for O, Mg, Ca, and other elements to a total of 100 wt%. The correlation coefficient between [Si] and [Mg] was determined. The [Si] was determined from this coefficient and [Mg] obtained by ICP-MS.

ST1.4.3. II: Boron, high field strength elements, and Ti

Four sets of spike solutions enriched in ^{11}B, ^{91}Zr-^{179}Hf, ^{97}Mo-^{119}Sn-^{121}Sb, and ^{183}W and mannitol solution were mixed with the aliquot, then, digested with B-free 30M HF (B-HF) in an ultrasonic bath for >12 hours. For some aliquots (noted in Table S11), an appropriate amount of aluminum was added prior to the addition of B-HF to prevent yield reduction due to fluoride co-precipitation of the target element [264)]. This was prepared as 0.25% solution using Al plasma standards (Specpure® 10000 μg/mL, Alfa Aesar, Lancashire, UK) after reducing the blank by through addition of HF (30M once, 0.5M 3 times), centrifugation, and supernatant removal repeatedly. The aliquot was dried in a B-free evaporation box at <80°C, dissolved in 0.5M B-HF, then the fluoride precipitate was removed by centrifugation. The supernatant of aliquot (~DF2000) was used for the determination of 9 trace element abundances by ICP-QMS (Thermo Fisher Scientific iCAP TQ). The [B], [Zr], [Mo], [Sn], [Sb], [Hf], and [W] were determined by ID, while [Nb] and [Ta] were determined by Zr-IS and Hf-IS, respectively [265)]. JB3 decomposed solution adjusted to DF2000 was used repeatedly for every 2 samples as an analytical standard for correction of mass discrimination, intensity drift, and determination of elemental abundances.

The [Ti] was measured by ICP-SFMS (Thermo Fisher Scientific ELEMENT XR) by applying the Nb-IS method using DF2000–4000 aliquots after ICP-QMS [265)]. The standard solution of Ti and Nb mixed at approximately 1000:1 was used as an analytical standard, and the signal of aliquots and standard were detected in pulse counting mode.

ST1.4.4. III: Chromium & S

Sample preparation and analysis were performed based on the literature [266, 267)] with some improvements. The aliquot was mixed with 0.06 mL of 2D 8.8M HBr, followed immediately by ^{34}S- and ^{53}Cr-enriched spike solutions, 0.03 mL of 1D 16M HNO_3, and 0.06 ml of 2D 30M HF, then digested at 80°C for >12 hours. The aliquot was dried at 80°C for 5–8 hours, then 0.1 mL of USQ and 0.06 mL of 1D 16 M HNO_3 were added and dried again. Finally, the decomposed aliquot was dissolved in 0.5M HNO_3, centrifugated and the supernatant was used for the determination of [S] and [Cr] by ICP-SFMS (Thermo Fisher Scientific ELEMENT XR) by applying the ID method. The decomposed reference sample (JA3; Geochemical Reference Samples of the GSJ) was used as an analytical standard to correct the mass discrimination. To detect the aliquot and standard S and Cr in the same detector mode, the aliquots and standard were adjusted as DF20000 and 300, respectively.

ST1.4.5. IV: Highly siderophile elements

Sample preparation and analysis were performed based on the literature [46)] with some improvements. The weighed aliquot and a mixed spike solution enriched in ^{101}Ru, ^{105}Pd, ^{185}Re, ^{189}Os, ^{191}Ir and ^{195}Pt were installed in a borosilicate carious tube (CT: 13 mm OD, 9 mm ID, 120 mm long) containing a frozen inverse aqua regia (0.15 mL of 9.5M HCl and 0.45 ml of 16M HNO_3), then flame-sealed. This procedure was carried out by placing the CT in an ethanol slush. After 72 hours of digestion at 240°C, the CT was opened and the aliquot was transferred into a PFA vial. Osmium was extracted with 0.5 mL of CCl_4 3 times, and the remaining solution was heated at 90°C to near-dryness. This ($\sim$10 μL) was then repeatedly digested once with 0.03 mL of 20M HF, twice with 0.1 mL of 8M HCl, and once with 0.1 mL of 1.5M HCl. Finally, the aliquot was dissolved in 0.1 mL of 0.5M HNO_3 for HSE purification.

The purification of HSE (except Os) from matrix elements was carried out in 2 stages on 3 different columns. In the first stage, tandem columns were used to separate HSE from major cations, Y, Zr, and Hf. The upper (polyethylene, 4 mm ID, 1.6 mm length, 2 mL reservoir) and lower columns (PTFE, 3 mm ID, 2.4 mm length, 2 mL reservoir) were packed with 0.2 mL of Bio-Rad AG50W-X12 resin (200–400 mesh; Bio-Rad Laboratories, Hercules, CA, USA) and 0.17 mL of Eichrom-Ln resin (100–150 μm size; Eichrom Technologies, Lisle.), respectively. After loading the aliquot on the upper column, 0.2 mL of 0.5M HNO_3 was loaded. After removal of the upper column, 0.9 mL of 0.5M HNO_3 was loaded on the lower column. All eluted fractions, dissolved in 1.2 mL of 0.5M HNO_3 were collected.

In the second stage, the aliquot collected in the first stage was directly loaded onto a custom-made column (PTFE, 3 mm ID, 1.5 mm length and a 2 mL reservoir) packed with 0.1 mL of Bio-Rad AG50W-X8 resin (200–400 mesh) to remove the remaining Cr. Then, 0.2 mL of 0.5M HNO_3 were loaded, and eluted fractions, a total of 1.4 mL solution, were collected. The eluted solution was heated to evaporate HNO_3 at 90°C till the solution yielded nearly 1 drop (0.03 mL), then 0.3 mL of 0.5M HNO_3 was added. The recovery yields of HESs were >80%.

The [Ru], [Pd], [Re], [Ir], and [Pt] measurement was performed by ID method using ICP-QMS (Thermo Fisher Scientific iCAP TQ) using kinetic energy discrimination (SQ-KED) with helium gas. Precious metals plasma standard solution (Specpure®, Alfa Aesar, Lancashire, UK) was used as an analytical standard for mass discrimination correction of each element. Oxide formation monitored using Ce was <0.4%. All interfering elements (Cr, Zr, Y, Cd and Hf) were monitored during the measurements and compared with the measurements of the synthetic solutions before and after the running of the samples, but they were below the detection limit or negligible.

Osmium extracted into a total of 1.5 mL of CCl_4 was back-extracted at least 3 times with 1 mL of 2D 8.8M HBr, evaporated to one drop at 100°C, and then purified by micro-distillation optimized for this study. In Os analysis of trace samples, optimization of micro-distillation is important to prevent loss of Os [268)]. In this study, both the amount of extracted Os and the amount of sample (matrix) are extremely small, so conditions that maintain the Os yield (>90%) and prevent evaporative contamination of Cr from the oxidant, which may interfere with Os ionization during analysis, were pre-examined, and micro-distillation performed as follows. The aliquot reduced to 1.5 μL as 2D 8.8M HBr was mixed with 20 μL of CrO_3-H_2SO_4 solution (8% m/v CrO_3 in 12 M H_2SO_4) and placed on a conical PFA vial cap, then Os was vaporized at ~60°C for 3 hours and captured in 20 μL of 2D 8.8M HBr at the tip of a conical vial (same as Fig.1 in the literature [269)]). After purification, the Os was loaded onto platinum filaments (0.76 mm × 0.03 mm; purity 99.995% m/m; H. Cross Company, Moonachie, NJ, USA,) and covered with $Ba(OH)_2$-NaOH activator [270, 271)]. The Pt filaments were pre-cleaned with 16M HNO_3 and air-baked at 3 A for 20 minutes.

Osmium isotopic analysis was performed in the negative mode of TIMS (Thermo Fisher Scientific TRITON plus) with Os detected as OsO_3^-. The amount of Os used in the analysis of each aliquot was only about 0.1 ng at most, even at 100% extraction yield. The secondary electron multiplier was used for the measurement and the peak jumping mode was applied [46)]. The $^{186}Os/^{188}Os$, $^{187}Os/^{188}Os$ and $^{190}Os/^{188}Os$ ratios for DROsS (Durham Romil Osmium Standard supplied by IA-Geo Limited) yielded 0.12040 ± 0.00118 (9.8‰), 0.16122 ± 0.00085 (5.3‰) and 1.98453 ± 0.00617 (3.1‰), respectively, using 0.1 ng of Os (2s and 2 RSD, n = 11).

The weights used in this analysis were 0.254–0.139 mg (an average of 0.175 mg), and the total amounts of Re and Os are 6–11 pg and 72–100 pg, respectively. The total procedural blank for Re averaged 0.78 ± 0.68 pg (78% of 1RSD, n = 9) and for Os 0.83 ± 0.05 pg (6.5% of RPD, n = 2), which corresponds to 7–13% and 0.8–1.1% of the Re and Os in the aliquots, respectively. In particular, the blank correction effect of [Re] is beyond the reproducibility of ICP-MS analysis, and its influence on the accuracy of $^{187}Re/^{188}Os$ cannot be negligible. Therefore, 2SE of $^{187}Re/^{188}Os$ (Table S13) was determined as follows. The uncertainty in the [Re] was calculated by error propagation of the reproducibility (repeated analysis of one aliquot of Orgueil: 2.7%, n = 4) and the deviation of the procedural blank by ICP-MS; [Os] uncertainty was calculated similarly using the precision of the individual aliquot and the deviation of the blank analyses by N-TIMS. From these, an uncertainty of the $^{187}Re/^{188}Os$ was determined. Note that weighing errors were not considered, because Re and Os were extracted from the same aliquot. Blank correction was also performed for $^{187}Os/^{188}Os$ using the obtained blank isotopic ratios (0.307 ± 0.185, n = 2) and the uncertainty was estimated using the precision of the individual aliquot and the deviation of the blank.

In addition, the Fe-sulfide fraction (several tens of μm in sized euhedral pyrrhotites), which was picked up from the C0019-19 using a micro-manipulator, was analyzed. Since the total weight of Fe-sulfide was ~4 μg, large weighing errors would be significant. Therefore, analytical values are presented as concentration ratios based on [Ru] to cancel the uncertainty caused by the weighing (Table S13). [Re]/[Ru] was not obtained due to the extremely small amount of [Re] in the fraction.

ST1.4.6. V: Germanium, As, Se, and Te

Sample preparation and analysis was performed based on the literature [266, 267)] with some improvements. The aliquot was mixed with 0.03 mL of 2D 8.8M HBr, followed immediately by ^{73}Ge, ^{77}Se and ^{125}Te enriched mixed spike solutions, 0.05 mL of 1D 16M HNO_3, and 0.1 mL of

2D 30M HF, and digested at 80°C for >12 hours. After drying the aliquot at 80°C for ~5 hours, 0.3 ml of 0.5M HF was added to dissolve, centrifuged, and the supernatant was dried again. Finally, the aliquot was dissolved in 0.5 M HNO_3 as DF1000–2000.

The measurements were performed using the triple quadrupole mode with the mass filter of ICP-QMS (Thermo Fisher Scientific iCAP TQ), using oxygen as the reaction gas (TQ-O_2 mode). Germanium, As and Se were detected in mass shift mode, i.e., as $^{72}Ge^{16}O$, $^{73}Ge^{16}O$, $^{75}As^{16}O$, $^{77}Se^{16}O$ and $^{78}Se^{16}O$, respectively, and Te as ^{125}Te and ^{126}Te in on-mass mode. The ID method was applied to [Ge], [Se] and [Te], while the Ge-IS method was applied to [As]. A mixed standard solution of Ge, As, Se, and Te was used as an analytical standard. To correct for the interference of Fe on Ge, ^{56}Fe and ^{57}Fe were monitored during the measurement of samples and the Fe solution was measured before and after every 6 samples to estimate the interference and perform the correction to $^{72}Ge^{16}O$ and $^{73}Ge^{16}O$.

ST1.4.7. VI: Calcium and Cr isotopes

Two Ryugu particles (0.444 mg for A0022 and 0.459 mg for C0081) were digested with HF-HNO_3 at 195°C for four days. Then the dried aliquots were re-dissolved in aqua regia for two days at 170°C. Chromium and Ca were purified using a sample aliquot containing ~0.4 μg of Cr and ~4.5 μg of Ca by ion-exchange chromatography. In the first separation step, Ca and Cr were separated with AG50W-X8 cation exchange resin (Bio-Rad Laboratories, USA, 200–400 mesh size) using hydrochloric and nitric acids. The Cr fraction was then purified twice using 1 mL of AG50W-X8 cation exchange resin using hydrofluoric, hydrochloric, and oxalic acids. The Ca-rich fraction after the first ion chromatography step was purified using DGA (Eichrom Technologies Inc, Normal) and AG1-X8 (Bio-Rad Laboratories, USA, 200–400 mesh size) resins using nitric and hydrochloric acids respectively. Recovery of Ca and Cr was >90% and the total procedural blanks were <0.2 ng for Cr and <13 ng for Ca, thus negligible for all particles analyzed in this study.

The Cr isotopic composition was determined using a Thermal Ionization Mass Spectrometer (Thermo Fisher Scientific TRITON plus) using a single W filament (Nilaco, 99.95% W) geometry. The Cr isotopic measurement was performed by the total evaporation method combined with a standard-sample bracketing method modified after the literature 272). For each single W filament, 0.02–0.04 μg of Cr and the same amount of Nb-H_3PO_4 activator 273) were loaded, and eight to ten samples and standards (NIST SRM 979) were measured for each sample. The measurement was performed using seven Faraday cups for ^{49}Ti (L3), ^{50}Cr (L2), ^{51}V (L1), ^{52}Cr (Center), ^{53}Cr (H1), ^{54}Cr (H2), and ^{54}Fe (H4) equipped with 10^{11} Ω feedback resistors. The ^{49}Ti, ^{51}V, and ^{54}Fe were monitored to apply interference correction for ^{50}Ti, ^{50}V, and ^{54}Fe, respectively. The proportion of total ions derived from the sum of ^{50}Ti and ^{50}V was typically <0.3 ppm on m/z = 50 and from ^{54}Fe on m/z = 54 was typically <50 ppm. The gain calibration was performed once a day at the beginning of the analytical session. The baseline measurement was performed for 600 seconds before each run. The instrumental mass fractionation effect was corrected according to an exponential law using $^{50}Cr/^{52}Cr = 0.051859$ 274). The average and standard error of individual measurements were calculated using a 2SD outlier rejection. The $^{54}Cr/^{52}Cr$ data are expressed in the ε notation according to the following formula;

$$\varepsilon^{54}\mathrm{Cr} = \left[(^{54}\mathrm{Cr}/^{52}\mathrm{Cr})_{sample}/(^{54}\mathrm{Cr}/^{52}\mathrm{Cr})_{SRM\ 979} - 1\right] \times 10^4 \qquad [4]$$

The $\varepsilon^{54}Cr$ values for JP1 (peridotite), Orgueil (CI1), Murchison (CM2), Allende (CV3) measured in this study are 0.17 ± 0.16 ($n = 9$), 1.52 ± 0.16 ($n = 10$), 1.11 ± 0.16 ($n = 23$), and 0.89 ± 0.19 ($n = 10$), respectively.

The Ca isotopic compositions (^{42}Ca, ^{43}Ca, ^{44}Ca, ^{46}Ca, and ^{48}Ca) were determined by TIMS (Thermo Fisher Scientific TRITON plus) using a double Re filaments geometry (H. Cross, zone-refined >99.999% Re). On the Re filament, 1–2 μg of Ca and the same amount of Cs activator were loaded. The Ca isotopic compositions were acquired in static mode using six Faraday cups for ^{42}Ca (L4), ^{43}Ca (L2), ^{44}Ca (L1), m/z = 44.325 (Center), ^{46}Ca (H1), and ^{48}Ca (H4), equipped with one (C) of $10^{11}\Omega$, two (L4 and L1) of 10^{12} Ω, and three (L2, H1, and H4) of 10^{13} Ω feedback resistors. The zoom lens was acquired. Before and after the Ca isotopic measurement, intensities of ^{46}Ca$^+$, ^{87}Sr^{2+} and ^{49}Ti$^+$ were measured by electron multiplier using a peak-jumping mode to monitor the potential interferences of ^{84}Sr^{2+} on ^{42}Ca$^+$, ^{86}Sr^{2+} on ^{43}Ca$^+$, ^{88}Sr^{2+} on ^{44}Ca$^+$, ^{46}Ti$^+$ on ^{46}Ca$^+$, and ^{48}Ti$^+$ on ^{48}Ca$^+$. Typically, two or three standards (SRM 915a) and two unknown samples were measured in each day. The gain calibration that takes 3.5 hours was performed once a day at the beginning of the analytical session. The baseline measurement was performed for 600 seconds before each run. For the interference correction, the IUPAC values of ^{46}Ti/^{49}Ti = 1.5251, ^{84}Sr/^{87}Sr = 0.07961, ^{86}Sr/^{87}Sr = 1.4078, ^{88}Sr/^{87}Sr = 11.795 were used. The instrumental mass fractionation effect was corrected according to an equilibrium law using ^{42}Ca/^{44}Ca = 0.31221.

The measurement of unknown samples was performed using more than two individual filaments and the average value and 2SE error were calculated. In the case of duplicated measurements, the larger value between the relative difference and the propagated 2SE internal precision is expressed as the error. The ^{48}Ca/^{44}Ca data are expressed in the ε notation according to the following formula:

$$\varepsilon^{48}\mathrm{Ca} = \left[({}^{48}\mathrm{Ca}/{}^{44}\mathrm{Ca})_{sample}/({}^{48}\mathrm{Ca}/{}^{44}\mathrm{Ca})_{SRM\ 915a} - 1\right] \times 10^4 \qquad [5]$$

The ε^{48}Ca values for BCR2 (basalt), Murchison, Allende, and Orgueil measured in this study are −0.11 ± 0.39 (n = 6, 2SE), 3.81 ± 0.11 (n = 5), 3.10 ± 0.14 (n = 4), and 2.49 ± 0.47 (n = 3), respectively.

ST1.4.8. VII: Hydrogen isotopes

Whole-rock [H] and D/H were determined by thermal-conversion elemental-analysis isotope-ratio-mass-spectrometry (TCEA-IRMS) system consisting of an autosampler (Costech ZeroBlank), a TCEA (Thermo Fisher Scientific TC/EA), a universal continuous flow interface (Thermo Fisher Scientific ConFlo IV), and an IRMS (Thermo Fisher Scientific MAT253). The detailed analytical method is described elsewhere [189, 201]. Aliquots of Ryugu and Orgueil (CI1) as well as geological reference sample SCo-1 (Cody Shale, USGS) and in-house talc working standard were placed into 0.012 mL Ag cupules (99.9%, Lüdiswiss) under atmospheric condition, then heated at 110°C for 6 hours *in vacuo* in a vacuum chamber. To minimize the absorption of moisture, Ryugu and Orgueil aliquots were not powdered as discussed previously [189]. Then, the vacuum chamber was opened in the glove box under an Ar atmosphere and the Ag capsules were cold-sealed.

The D/H is expressed by deviation from international standard VSMOW-SLAP in a linear scale (δD). The δD value of the reference gas was calibrated using VSMOW and SLAP2 shielded in silver tubes distributed by the US Geological Survey. The [H] blank of the Ag capsule treated in the same way as the unknown samples was 7–9 ng, and the blank correction was performed for all samples. The calibration curve for [H] was obtained by analyzing various amounts of benzoic acid. The [H] of an in-house talc standard, (Talc-1: SiO_2 = 63.2 wt%, MgO = 32.0 wt%, FeO = 0.04 wt%, CaO = 0.03 wt%, and the stoichiometric composition of H_2O = 4.74 wt%) and of SCo-1 were 0.555 ± 0.029 wt% (n = 11, 2SD) and 0.643 ± 0.055 wt% (n = 5, 2SD), which agrees with the stoichiometric value (0.527 wt%) and is within the range of the published data (0.562–0.712 wt%) [275, 276], respectively. The measured δD value of GISP, an IAEA international reference water, was −188.7 ± 5.4‰ (2SD, n = 27), which is within the range of reference value

(−189.5 ± 2.4‰, 2SD). The measured δD value of rock samples were −38.1 ± 14.5 ‰ (n = 11, 2SD, 0.96–9.52 μg of H) for Talc-1 and −69.3 ± 6.1‰ (n = 5, 2SD, 1.28–3.58 μg of H) for SCo-1. The 2SD relative intermediate deviation of [H] for unknown samples applied as 5% based on the data for Talc-1 and the 2SD intermediate deviation of 2SD of δD value as 6‰ based on the SCo-1 data.

ST1.4.9. VIII and IX: Carbon and nitrogen isotope

The [C] ($[C]_{TC}$ and $[C]_{TOC}$, where TC and TOC stand for total carbon and total organic carbon, respectively), [N], $^{13}C/^{12}C$ (both for TC and TOC), and $^{15}N/^{14}N$ of the samples were determined by an elemental-analysis IRMS (EA-IRMS) system consisting of an autosampler (Costech ZeroBlank), a flash combustion elemental analyzer (Thermo Fisher Scientific Flash 2000), a universal continuous flow interface (Thermo Fisher Scientific ConFlo IV), and an IRMS (Thermo Fisher Scientific MAT253). From the original configuration of the EA, oxidation and reduction tubes were replaced to narrow-diameter quartz tubes 277). Bulk samples and standards wrapped in Sn capsules were combusted in the oxidation column heated at 1020°C. The combusted gas was then transferred to the reduction column heated at 650°C. After removing water by magnesium perchlorate, CO_2 and N_2 were separated by GC, and the gases were transferred to the mass spectrometer via the continuous flow interface. The total procedural blank of [C] and [N] measured by combusting the Sn foil was 0.77 ± 0.11 μg and 0.034 ± 0.013 μg (2SD, n = 21), respectively. For the total organic carbon ($[C]_{TOC}$) measurement, the Ag capsules containing the weighted aliquots were reacted with 6M HCl at 65°C three times followed by H_2O at 65°C three times. Then, the Ag capsule was wrapped in Sn foil. Total procedural blank of $[C]_{TOC}$ and [N] for the TOC measurements were 1.14 ± 0.11 μg and 0.039 ± 0.007 μg (2SD, n = 5), respectively. A blank correction was performed for all measurements.

Calibration curves for [C] and [N] were obtained by analyzing various amounts of working isotope standard Urea (IVA Analysentechnik GmbH). International and working isotope standards, IAEA-602, IAEA-N-2, and IVA-urea, were used to calibrate the $\delta^{13}C$ and $\delta^{15}N$ values of unknown samples. Isotopic compositions of C and N are expressed by deviation from V-PDB ($\delta^{13}C$) and the air ($\delta^{15}N$). The calibration curves were monitored by measuring international reference materials IAEA-CH7 and IAEA-N-1, yielding $\delta^{13}C$ = −32.05 ± 0.08 ‰ (2SD, n = 5) and $\delta^{15}N$ = 0.39 ± 0.22 ‰ (2SD, n = 4), respectively, which agreed with the IAEA reference values ($\delta^{13}C$ = −32.15 ± 0.10 for IAEA-CH7 and 0.4 ± 0.4 for IAEA-N1).

The analytical uncertainty for $\delta^{13}C$ and $\delta^{15}N$ values were determined by analyzing an in-house epoxy resin standard, resin-specifix ([C] = 70.9 wt% and [N] = 2.60 wt%). The $\delta^{13}C$ and $\delta^{15}N$ values did not vary systematically when analyzing samples that contain 7–153 μg of C and 0.5–11.7 μg of N, yielding $\delta^{13}C$ = −29.92 ± 0.06 ‰ (2SD, n = 8) and $\delta^{15}N$ = −0.28 ± 0.46 ‰ (2SD, n = 12), respectively. When the amount of N used in the analysis was < 0.5 μg, the $\delta^{15}N$ values exceeded the 2SD of the data measured for > 0.5 μg of N. Thus, the data for unknown samples measured using the <0.5 μg of N will be omitted.

The international geological reference material, SCo-1 (Cody Shale, USGS) was measured along with unknown samples. The SCo-1 contains 6 vol% of dolomite 278), 57 vol% of phyllosilicates 278), ~0.96 wt% of $[C]_{TC}$ 276), ~0.28 wt% of $[C]_{TOC}$ 276), and ~0.05 wt% of [N] 276). Mineral assemblages of SCo-1 resemble those of the Ryugu particles and the $[C]_{TC}$ and [N] in SCo-1 are approximately 20–50% of the Ryugu particles. Thus, SCo-1 was selected as an adequate reference material to evaluate the analytical precision of Ryugu particles. The measured result for SCo-1, using a mass range of 0.07–2.10 mg (n = 18), is as follows: $[C]_{TC}$ = 0.956 ± 0.080 wt% (2SD, n = 18, 0.4–36 μg of C), N = 0.051 ± 0.004 wt% (2SD, n = 18, 0.07–2.1 μg of N), $\delta^{13}C_{TC}$ = −8.71 ± 0.73 ‰ (2SD, n = 18, 0.4–36 μg of C), and $\delta^{15}N$ = 3.7 ± 3.5 ‰ (2SD, n = 15, 0.57–2.1

μg of N) for bulk samples and $[C]_{TOC}$= 0.224 ± 0.012 wt%, [N] = 0.052 ± 0.017 wt%, $\delta^{13}C_{TOC}$ = −25.23 ± 0.32 ‰, and $\delta^{15}N$ = 0.82 ± 0.21 ‰ for decarbonated samples (2SD, 6.7–7.8 μg of C and 1.5–2.0 μg of N, n = 4). These measured values agree with the literature data [276)] within the 2SD range except for $\delta^{13}C_{TC}$ (−6.18 ± 0.26 ‰) and $[C]_{TOC}$ (0.283 ± 0.006 wt‰). As observed for the resin-specifix, when the amount of N used in the analysis was <0.5 μg, the $\delta^{15}N$ values for SCo-1 exceeded the 2SD of the data measured for >0.5 μg [N]. For C, the $\delta^{13}C_{TC}$ values of SCo-1 and those measured using >0.4 μg of C do not show any systematic difference. Thus, all the measured data of unknown samples were adopted. The larger 2SD values of all data for SCo-1 relative to those of resin-specifix could be due to the larger sample heterogeneity for the former relative to the latter.

The 2SD relative intermediate precision (2SD%) of [C] and [N] for unknown sample measurements are applied as 8 % and the 2SD intermediate precision of $\delta^{13}C$ and $\delta^{15}N$ values as 0.73‰ and 3.5 ‰, respectively, based on the data for SCo-1.

Abundance and isotopic composition of carbonate C ($[C]_{carb}$ and $\delta^{13}C_{carb}$) were calculated as

$$[C]_{carb} = [C]_{TC} - [C]_{TOC} \qquad [6]$$

and

$$\delta^{13}\mathrm{C}_{carb} = \frac{[C]_{TC} \times \delta^{13}\mathrm{C}_{TC} - [C]_{TOC} \times \delta^{13}\mathrm{C}_{TOC}}{[C]_{carb}}. \qquad [7]$$

ST1.4.10. X: Oxygen isotope

The oxygen of the samples was extracted using the laser fluorination method. The isotopic compositions in the extracted O_2 gas were determined using a gas-source mass spectrometer (Thermo Fisher Scientific MAT253) in dual inlet mode. The detailed analytical method is described elsewhere [201, 279, 280)]. Aliquots of unknown samples (Ryugu and Orgueil) were installed in the individual vacuum chamber. In each chamber, one standard (UWG-2 garnet [281)]) and one blank container were also placed. In other chambers, reference garnet standards UWG-2 were installed. After installing the samples, the chambers were baked at 180°C for 6 hours *in vacuo*, followed by the samples, which were prefluorinated by BrF_5 for 1 hour. After evacuation, the O_2 in the sample was extracted using a CO_2 laser with BrF_5 as an oxidation agent. In each chamber which contains an unknown sample, laser fluorination was performed in the following order: unknown sample, standard, and blank. Blank measurements were performed by the same procedure for samples without sample in the container. The extracted O_2 was purified in the extraction line, then trapped with a 13Å molecular sieve at the temperature of liquid N_2. After warming the molecular sieve at 100°C then cooling to room temperature, the O_2 was expanded into the bellows of the dual inlet system. Before oxygen isotopic measurements, impurity of CF_4 and NF_4 were monitored by measuring the intensities of m/z = 50 (CF_2^+) and m/z = 52 (NF_2^+) relative to m/z = 32 ($^{16}O_2^+$). The intensity ratios of m/z = 50/32 and 52/32 for oxygen extracted from Orgueil and Ryugu were within the range of those from UWG-2 and in the reference tank gas. Thus, no further purification of O_2 was performed. The total procedural O_2 blank was <4 nmol. The proportion of O_2 blank in the sample O_2 was <0.3%, which was negligible. Thus, no blank correction was performed. The integration time was eight seconds and the measurement was performed for 50 to 100 cycles. The O isotopic compositions of working reference gas were previously calibrated by VSMOW2 and SLAP2, and all data were expressed using the VSMOW2/SLAP2 scale. The $^{18}O/^{16}O$ and $^{17}O/^{16}O$ of the sample were expressed as the common delta notation relative to VSMOW2 as $\delta^{17 \text{ or } 18}O = (^{17 \text{ or } 18}O/^{16}O_{\text{sample}})/(^{17 \text{ or } 18}O/^{16}O_{\text{VSMOW2}}) - 1$. The excess ^{17}O value relative to the terrestrial silicate fractionation line (TSFL) is defined as $\Delta^{17}O = \delta^{17}O' - 0.528 \times \delta^{18}O'$, where $\delta^{17}O' = \ln(\delta^{17}O^* + 1)$, $\delta^{17}O^* = \delta^{17}O + 0.033 \times 10^{-3}$, and $\delta^{18}O' = \ln(\delta^{18}O + 1)$. Mean value of the oxygen isotopic compositions of UWG-2 extracted from 0.629–1.035 mg (mean = 0.77 mg) of samples are $\delta^{17}O = 2.954 \pm 0.058$ ‰, $\delta^{18}O = 5.708 \pm 0.051$ ‰, and $\Delta^{17}O = -0.022 \pm 0.037$‰ (2SD, $n = 3$) and from 0.240–0.422 mg (mean = 0.33 mg) of samples are $\delta^{17}O = 3.015 \pm 0.114$ ‰, $\delta^{18}O = 5.789 \pm 0.163$ ‰, and $\Delta^{17}O = -0.004 \pm 0.054$ ‰ (2SD, $n = 8$). Because the amounts of unknown samples used for O isotopic measurements are 0.247 and 0.568 mg, the intermediate precision (2SD) of unknown sample measurements are applied to the latter values: i.e. 0.11‰, 0.16‰, and 0.054‰ for $\delta^{17}O$, $\delta^{18}O$, and $\Delta^{17}O$ values.

ST1.4.11. XI: Neon

Ryugu particles (<0.13 mg) were individually weighed and placed in Ni cylinders ($\phi = 4$ mm, 15-mm length with a hole of $\phi = 2$ mm and 5-mm depth) 201).

Most samples were selected from tiny pieces scattered around larger grain(s) in a sample container. Exceptions are particles A0035-7, A0035-8, A0035-10, and A0035-11. Those aliquots were fragments separated from a plane, created by an ultra-microtome, on the grain (A0035) using a tweezer. The cylinders with the aliquots were mounted on a base plate in a sample chamber sealed with a viewport (Kodial Zero Length VPZ38LA, Torr Scientific Ltd., UK) and joined with a gas-handling system (HORIVAC PEG-0150, Horiguchi Ironworks, Ltd., Japan) via an actuated bellows valve (Swagelok®SS-4H-TW welded with an ICF flange, Horiguchi Ironworks, Ltd., Japan). Samples and the gas-handling system were baked at 200°C for 3 days to ensure the removal of terrestrial volatiles adsorbed during sample manipulation.

Neon and the other volatiles (e.g., Ar and H_2O) were extracted by complete sample fusion with laser radiation (wavelength of 1064 nm). A fiber laser (redEnergy®G4, SPI Laser, UK) was employed in continuous wave operation with an output power of 3–9 W. Noble gases were purified by exposure of extracted volatiles to non-evaporable getters (Al-Zr alloy, SAES®NP-10). Neon was separated from the other noble gases using charcoal traps cooled with liquid N_2 and a stainless-steel (SUS) trap cooled with a He-circulation cryocooler (Mini-Stat CRT-006-0000, Iwatani Industrial Gases Corp., Ltd., Japan). Neon was adsorbed on a SUS trap at 20 K, and other noble gases were eliminated by evacuation (He) or adsorption onto charcoal traps (Ar, Kr, and Xe). Then, Ne was released from a SUS trap at 50 K (controlled by internal heating elements) and admitted into a static-vacuum mass spectrometer (Helix SFT, Thermo Fisher Scientific).

Prior to this study, the internal elements of the mass spectrometer were cleaned by bakeout at 350°C, including the ion source, flight tube, and collector housing. The collector used is a secondary electron multiplier (Balzers SEV217, in ion pulse-counting mode), and the equivalent ion currents for $^{20}Ne^{+}$, $^{21}Ne^{+}$, $^{22}Ne^{+}$, $^{40}Ar^{+}$, and $^{44}CO_2^{+}$ were measured sequentially by magnetic peak jumping. The trap current was adjusted to be 200 or 400 μA, so as to suppress ion currents of $^{20}Ne^{+}$ <200 fA (corresponding to 1.25 Mcps). The electron energy for ionization was 80–87 eV, and the electric potential for ion acceleration was 4.5 kV. The sensitivity ($S \equiv I/Q$ where I is Ne^{+} signal and Q is Ne quantity) of the instrument and correction factor for mass-bias effect were calibrated in reference to analyses of atmospheric Ne in air doses ($[^{20}Ne] = 2 \times 10^{-12}$ to 1×10^{-9} ccSTP). Interferences of $^{40}Ar^{++}$ on $^{20}Ne^{+}$ and $^{44}CO_2^{++}$ on $^{22}Ne^{+}$ were suppressed by a charcoal trap equipped with an ion source, and those effects were corrected following the literature 282). Interference from $^{20}NeH^{+}$ to $^{21}Ne^{+}$ was negligible in our system. The blank of Ne has a typical abundance of 1×10^{-12} ccSTP (≡ 0.05 fmol), and its $^{20}Ne/^{22}Ne$ and $^{21}Ne/^{22}Ne$ are indistinguishable from atmospheric Ne 245).

The contribution of blank to sample Ne varies from <1 to 25% with a mean of 6 (±7) %, and was corrected for in all analyses.

Deconvolution of Ne into that from distinct components was performed with the following assumptions; (1) three components were involved, which were Ne from solar wind (denoted as

"SW") implantation, Ne intrinsically trapped in Ryugu constituents ("trap"), and Ne produced by reactions between Ryugu constituents and cosmic rays ("cos"); (2) $^{20}Ne/^{22}Ne$ and $^{21}Ne/^{22}Ne$ of each component were: $(^{20}Ne/^{22}Ne)_{SW} = 13.78$ and $(^{21}Ne/^{22}Ne)_{SW} = 0.0329$ [63]; $(^{20}Ne/^{22}Ne)_{trap} = 8.5–8.9$ and $(^{21}Ne/^{22}Ne)_{trap} = 0.029$, similar to compositions of the trapped noble-gas components Q [283] or HL [63, 283, 284] in carbonaceous chondrites; and (3) $(^{20}Ne/^{22}Ne)_{cos} = 0.72–2.3$ and $(^{21}Ne/^{22}Ne)_{cos} = 1.0–0.7$, estimated from physical models of nuclear reactions [237, 238, 285]. The variable $(^{20}Ne/^{22}Ne)_{cos}$ and $(^{21}Ne/^{22}Ne)_{cos}$ in assumption 3 are due to the varying production rates of cosmogenic Ne nuclides via reactions with cosmic rays of different origins and at different depths.

Two origins of cosmic rays are known. One is from outside of the solar system, termed galactic cosmic rays (GCR). Another is from the sun, and termed solar cosmic rays (SCR). These cosmic rays have different penetration depths; GCR can penetrate to depths equivalent to ~500 g cm^{-2}, while SCR penetration is confined to a few tens of g cm^{-2}. The depths of Ryugu particles during exposure to SCR/GCR are hardly constrained. We examined cosmogenic production at depths (as shielding depth) varying from 0 to 270 g cm^{-2}. That depth interval corresponds to 0–1.7 m (section 2.2.) with $\rho = 1.53$ g cm^{-3} (Supplementary Text ST1.1). The depth may also be comparable to the thickness of the layer (a few meters) in which surface and sub-surface materials were mixed to each other via impacts, thermal fatigue, and mass wasting [13].

Relative contributions of SCR and GCR in Ne production vary with depths. A critical depth is 15 g cm^{-2} at which SCR effect becomes insignificant. Two scenarios were examined (Table S22): GCR + SCR spallation at shielding depths <15 g cm^{-2} (Scenario 1), and sole GCR spallation at shielding depths of >15 g cm^{-2} (Scenario 2). For each scenario, options for different depth intervals were examined; Option 1 (0–1.5 g cm^{-2}), Option 2 (1.5–5 g cm^{-2}), Option 3 (5–10 g cm^{-2}) and Option 4 (10–15 g cm^{-2}) for Scenario 1, and Option 5 (15–20 g cm^{-2}), Option 6 (45–50 g cm^{-2}), Option 7 (100–120 g cm^{-2}) and Option 8 (250–270 g cm^{-2}) for Scenario 2. It is noted that the choice of different options yields different production rates of ^{20}Ne, ^{21}Ne and ^{22}Ne [$P(^{20,21,22}Ne)$], hence different $(^{20}Ne/^{22}Ne)_{cos}$ and $(^{21}Ne/^{22}Ne)_{cos}$.

Results of deconvolution are summarized in Tables S24–S27. The variation in $[Ne]_{trap}$ among the options for a sample is as small as 6% while those of $[Ne]_{SW}$ and $[Ne]_{cos}$ are 0–33% and 31–47%, respectively. Those variations are comparable to the uncertainties of $[Ne]_X$ (where X is SW, trap or cos) propagated from variables related to Ne analysis (typically 20–30%). Sample-to-sample variations, defined as $\sigma[Ne]_X/\overline{[Ne]_X}$, are much greater being 56–57% for $[Ne]_{trap}$, 330% for $[Ne]_{SW}$ and 190–200% for $[Ne]_{cos}$. The mean values of $[Ne]_{SW}$, $[Ne]_{trap}$, and $[Ne]_{cos}$ were used for comparison with other geochemical and spectral features.

The $P(^{21}Ne)$ in Ryugu particles are calculated for various shielding depths. At depths of 1.5–120 g cm^{-2}, $P(^{21}Ne)$ is fairly constant at $0.13–0.15 \times 10^{-8}$ (ccSTP g^{-1}) Myr^{-1} (Options 2–7). At the very surface (<1.5 g cm^{-2}; Option 1), $P(^{21}Ne)$ is as large as 0.20×10^{-8} (ccSTP g^{-1}) Myr^{-1} due to a greater SCR contribution. At greater depths (250–270 g·cm^{-2}; Option 8), $P(^{21}Ne)$ decreases to 0.0658×10^{-8} (ccSTP g^{-1}) Myr^{-1} due to the enhanced shielding effect. The cosmic-ray exposure ages (CRE ages or T_{CRE}) are calculated from $[^{21}Ne]_{cos}$ and $P(^{21}Ne)$ as

$$T_{CRE} = \frac{[^{21}Ne]_{cos}}{P(^{21}Ne)}. \tag{8}$$

The $[^{21}Ne]_{cos}$ is calculated from $[Ne]_{cos}$, $(^{20}Ne/^{22}Ne)_{cos}$, and $(^{21}Ne/^{22}Ne)_{cos}$. The T_{CRE} ranges from 0.5 to 8.3 Ma for Ryugu particles, except for that calculated for Option 8. The T_{CRE} for Option 8 are significantly older (1–16 Ma), merely due to low $P(^{21}Ne)$ at greater depth (250–270 g cm^{-2}).

ST1.4.12. Insoluble organic matter

Flaky aliquots of Ryugu particle A0035 and C0008, and Orgueil (CI1) were prepared by ultra-microtome and extracted in once distilled ultrapure water for 20 hours at 110°C to extract the soluble OM. Subsequently, the residual sample flacks were washed 3 times with water and dried. The dried residues were then demineralized by the addition of different acid mixtures. Firstly, 0.5 mL 1M HCl/10M HF was added and the mixture was agitated for 24 hours, followed by centrifugation at 3500 rpm for 30 minutes. The supernatant was then removed and 0.5 mL 6M HCl was added and agitated for 24 hours, before centrifugation and removal of the supernatant. The two steps were then repeated once more. In order to remove fluorides and any minerals coated in fluorides, a mixture of 0.5 ml 6M HCl/0.6M H_3BO_3 was added and the mixture agitated for 20 minutes, followed by heating at 70°C for 24 hours and centrifugation at 3500 rpm for 10 minutes. The supernatant was then removed and 0.5 ml 6M HCl/2M HF was added. The mixture was subsequently agitated for 20 minutes, before heating at 70°C for 24 hours and centrifugation at 3500 rpm for 10 minutes and removal of the supernatant. The two steps were repeated once more. Finally, to remove the HF acid and any remaining dissolved minerals, 0.5 mL 0.1M HCl was added, followed by centrifugation at 3500 rpm for 10 minutes and removal of the supernatant. This step was repeated a further 8 times, followed by drying.

The IOM residue was then suspended in water and transferred to a diamond compression cell and dried. The cell was then closed and pressed ready for transmittance FTIR spectroscopy. The FTIR spectrum was taken by using Thermo scientific Nicolet Continuum IR microscope equipped with the MCT/A detector and applying the transmission mode. To select the field of view, ~50 μm × 50 μm size of the square aperture was used. The background signal was collected at the sample-free part on the diamond window before each sample analysis. A number of scans were 150 or 300 for 650 to 4000 cm^{-1} spectrum range with 4 cm^{-1} of resolution. Data acquisition and processing, including background subtraction, were performed using OMNIC software.

ST1.4.13. Soluble organic matter

A 2.57 mg aliquot of Orgueil (CI1) and a 1.90 mg aliquot of Ryugu particle C0008 were placed within 300 μL insert vials along with 200 μL of once distilled ion-exchanged water (Puric-ω, Organo Co.) and heated for 20 hours at 110°C. After cooling the water supernatant and 3-times water washes were transferred to a 10 mL tube and sealed with a Teflon coated screw cap. The 10 mL tubes were then frozen overnight, before freeze-drying to remove the water. The freeze-dried residues were then heated at 110°C with 300 μL 2M HCl/isopropyl alcohol to convert the amino acids to isopropyl esters. The mixture was cooled and then reduced under a flow of N_2 until near dryness. Approximately 1 mL of water was added to each tube and the 10 mL tubes were again placed in a freezer overnight. The frozen isopropyl derivatives were then freeze-dried to ensure complete dryness and dissolved in 100 μL of ethyl acetate and transferred to 300 μL insert vials for analysis. A 300 μL insert vial was also run with water, but no sample and taken through the entire procedure to act as a procedural blank. Blanks were also included at every step to constrain the source of any contaminant contributions.

Ultra-High Performance Liquid Chromatography (UHPLC)-OT-MS analysis was performed in reversed phase using a Thermo Fisher Scientific Accucore^{TM} 150 Amide HILIC column on a Vanquish^{TM} UHPLC unit coupled to an Orbitrap Fusion Mass Spectrometer (Thermo Scientific). A binary pump system was installed in the UHPLC unit and allowed for a dynamically changing gradient between two phases, A (10 mM ammonium formate in water, adjusted to pH 3.5 using formic acid) and B (100% ACN). The gradient was adjusted from 100% B to 79% B over 15 minutes, to 0% B over a further 5 minutes, then held at 0% B for 5 minutes, before increasing to 100% B over 5 minutes and holding at 100% B for an additional 5 minutes. The following parameters were used for UHPLC-OT-MS: a flow rate of 0.15 mL/minute, column compartment temperature of 30°C, ion transfer tube and vaporizer temperature of 300°C, positive ion voltage of 3500 V, sheath gas of 50 and an auxiliary gas of 15. The OT-MS scan parameters were as follows: a RF lens of 55%, m/z range of 50–500, OT resolution of 240000 and an AGC target of 2×10^5.

The data obtained for UHPLC-OT-MS was compared to that obtained from two standards. The first standard was a custom in-house standard containing 27 amino acids and the second was a commercial standard (AN-2) that contained an additional 2 amino acids (proline and hydroxyproline) and urea. Assignments were initially made through a comparison of the retention times (RT) between the standards and the samples. Where a peak was found at a similar RT to that in the standard, it was assumed to be the same compound. Subsequently, for the amino acids that gave a high enough response, tandem mass spectrometry (MS/MS) was performed, and the MS/MS responses (fragmentation patterns) were compared between the samples and the standards. In all cases no amino acid identified by RT was found to have a different fragmentation pattern to the standard. However, there were some cases (especially for C0008) where the fragmentation pattern could not be extracted from the data of the sample, due to the response being too low.

References

246) Fredriksson, K. and Kerridge, J.F. (1988) Carbonates and sulfates in CI chondrites: formation by aqueous activity on the parent body. Meteoritics **23**, 35-44.

247) Tomeoka, K. and Buseck, P.R. (1988) Matrix mineralogy of the Orgueil CI carbonaceous chondrite. Geoch. Cosmoch. Acta **52**, 1627-1640.

248) Bullock, E.S., Gounelle, M., Lauretta, D.S., Grady, M.M. and Russell, S.S. (2005) Mineralogy and texture of Fe-Ni sulfides in CI1 chondrites: Clues to the extent of aqueous alteration on the CI1 parent body. Geoch. Cosmoch. Acta **69**, 2687-2700.

249) Berger, E.L., Lauretta, D.S., Zega, T.J. and Keller, L.P. (2016) Heterogeneous histories of Ni-bearing pyrrhotite and pentlandite grains in the CI chondrites Orgueil and Alais. Meteorit. Planet. Sci. **51**, 1813-1829.

250) Nakamura, E., Makishima, A., Moriguti, T., Kobayashi, K., Sakaguchi, C., Yokoyama, T. et al. (2003) Comprehensive geochemical analyses of small amounts (100mg) of extraterrestrial samples for the analytical competition related to the sample-return mission, MUSES-C. *In* The first Open Competition for the MUSES-C Asteroidal Sample Preliminary Examination Team, The Institute of Space and Astronautical Science. Report SP No. 16 (eds. Kushiro, I., Fujiwara, A. and Yano, H.). Inst. Space and Astron. Sci., Sagamihara, pp. 49-101.

251) Bagheri, G.H., Bonadonna, C., Manzella, I. and Vonlanthen, P. (2015) On the characterization of size and shape of irregular particles. Powder Technol. **270**, 141-153.

252) Kunihiro, T., Ota, T., Yamanaka, M., Potiszil, C. and Nakamura, E. (2021) The trace element composition of chondrule constituents: Implications for sample return methodologies and the chondrule silicate reservoir. Meteorit. Planet. Sci. **57**, 429-449.

253) Huberty, J.M., Kita, N.T., Kozdon, R., Heck, P.R., Fournelle, J.H., Spicuzza, M.J. et al. (2010) Crystal orientation effects in δ^{18}O for magnetite and hematite by SIMS. Chem. Geol. **276**, 269-283.

254) Śliwiński, M.G., Kitajima, K., Kozdon, R., Spicuzza, M.J., Fournelle, J.H., Denny, A. et al. (2016) Secondary ion mass spectrometry bias on isotope ratios in dolomite–ankerite, Part I: δ^{18}O matrix effects. Geostand. Geoanal. Res. **40**, 157-172.

255) Ogliore, R.C., Huss, G.R. and Nagashima, K. (2011) Ratio estimation in SIMS analysis. Nucl. Instrum. Meth. B **269**, 1910-1918.

256) Papanastassiou, D.A. (1978) Chromium isotopic anomalies in the Allende meteorite. Astrophys. J. **308**, 27-30.

257) Sugiura, N., Ichimura, K., Fujiya, W. and Takahata, N. (2010) Mn/Cr relative sensitivity factors for synthetic calcium carbonate measured with a NanoSIMS ion microprobe. Geochem. J. **44**, e11-e16.

258) Steele, R.C.J., Heber, V.S. and McKeegan, K.D. (2017) Matrix effects on the relative sensitivity factors for manganese and chromium during ion microprobe analysis of carbonate: Implications for early Solar System chronology. Geoch. Cosmoch. Acta **201**, 245-259.

259) Eklund, P.C. and Subbaswamy, K.R. (1979) Analysis of Breit-Wigner line shapes in the Raman spectra of graphite intercalation compounds. Phys. Rev. B **20**, 5157-5161.

260) Takano, Y., Yamada, K., Okamoto, C., Sawada, H., Okazaki, R., Sakamoto, K. et al. (2020) Chemical assessment of the explosive chamber in the projector system of Hayabusa2 for asteroid sampling. Earth Planets Space **72**, 97.

261) Ogawa, K., Shirai, K., Sawada, H., Arakawa, M., Honda, R., Wada, K. et al. (2017) System configuration and operation plan of Hayabusa2 DCAM3-D camera system for scientific observation during SCI impact experiment. Space Sci. Rev. **208**, 125-142.

262) Yokoyama, T., Makishima, A. and Nakamura, E. (1999) Evaluation of the coprecipitation of incompatible trace elements with fluoride during silicate rock dissolution by acid digestion. Chem. Geol. **157**, 175-187.

263) Makishima, A. and Nakamura, E. (2006) Determination of major, minor and trace elements in silicate samples by ICP-QMS and ICP-SFMS applying isotope dilution-internal standardization (ID-IS) and multi-stage internal standardization. Geostand. Geoanal. Res. **30**, 245-271.

264) Tanaka, R., Makishima, A., Kitagawa, H. and Nakamura, E. (2003) Suppression of Zr, Nb, Hf, and Ta coprecipitation in fluoride compounds for determination in Ca-rich materials. J. Anal. At. Spectrom. **18**, 1458-1463.

265) Lu, Y., Makishima, A. and Nakamura, E. (2007) Coprecipitation of Ti, Mo, Sn and Sb with fluorides and application to determination of B, Ti, Zr, Nb, Mo, Sn, Sb, Hf and Ta by ICP-MS. Chem. Geol. **236**, 13-26.

266) Makishima, A. and Nakamura, E. (2001) Determination of total sulfur at microgram per gram levels in geological materials by oxidation of sulfur into sulfate with in situ generation of bromine using isotope dilution high-resolution ICPMS. Anal. Chem. **73**, 2547-2553.

267) Makishima, A., Kobayashi, K. and Nakamura, E. (2002) Determination of chromium, nickel, copper and zinc in milligram samples of geological materials using isotope dilution high resolution inductively coupled plasma-mass spectrometry. Geostand. Newslett. **26**, 41-51.

268) Nakanishi, N., Yokoyama, T., Okabayashi, S., Iwamori, H. and Hirata, T. (2022) Geochemical constraints on the formation of chondrules: Implication from Os and Fe isotopes and HSE abundances in metals from CR chondrites. Geoch. Cosmoch. Acta **319**, 254-270.

269) Birck, J.L., Barman, M.R. and Capmas, F. (1997) Re-Os isotopic measurements at the femtomole level in natural samples. Geostand. Newslett. **21**, 19-27.

270) Creaser, R.A., Papanastassiou, D.A. and Wasserburg, G.J. (1991) Negative thermal ion mass spectrometry of osmium, rhenium and iridium. Geoch. Cosmoch. Acta **55**, 397-401.

271) Völkening, J., Walczyk, T. and G. Heumann, K. (1991) Osmium isotope ratio determinations by negative thermal ionization mass spectrometry. Int. J. Mass Spectrom. **105**, 147-159.

272) van Kooten, E.M.M.E., Wielandt, D., Schiller, M., Nagashima, K., Thomen, A., Larsen, K.K. et al. (2016) Isotopic evidence for primordial molecular cloud material in metal-rich carbonaceous chondrites. Proc. Natl. Acad. Sci. USA **113**, 2011-2016.

273) Li, C. F., Feng, L. J., Wang, X. C., Chu, Z. Y., J.-H. Guo, J. H., and Wilde, S. A. (2016) Precise measurement of Cr isotope ratios using a highly sensitive Nb_2O_5 emitter by thermal ionization mass spectrometry and an improved procedure for separating Cr from geological materials, J Anal. Atom. Spectrom. **31**, 2375-2383.

274) Shields, W.R., Murphy, T.J., Catanzaro, E.J. and Garner, E.L. (1966) Absolute isotopic abundance ratios and the atomic weight of a reference sample of chromium. J. Res. NBS A Phys. Chem. **70A**, 193-197.

275) Kubota, R. (2009) Simultaneous determination of total carbon, nitrogen, hydrogen and sulfur in twenty-seven geological reference materials by elemental analyser. Geostand. Geoanal. Res. **33**, 271-283.

276) Stüeken, E.E., de Castro, M., Krotz, L., Brodie, C., Iammarino, M. and Giazzi, G. (2020) Optimized switch-over between CHNS abundance and CNS isotope ratio analyses by elemental analyzer-isotope ratio mass spectrometry: Application to six geological reference materials. Rapid Commun. Mass Spectrom. **34**, e8821.

277) Ogawa, N.O., Nagata, T., Kitazato, H. and Ohkouchi, N. (2010) Ultra sensitive elemental analyzer/isotope ratio mass spectrometer for stable nitrogen and carbon isotope analyses. *In* Earth, Life and Isotopes (eds. Ohkouchi, N., Tayasu, I. and Koba, K.). Kyoto University Press, pp. 339-353.

278) Schultz, L.G., Tourtelot, H.A. and Flangan, F.J. (1976) Cody Shale, SCo-1, from Natrona County, Wyoming. USGS Professional Paper **840**, 21-23.

279) Pack, A., Tanaka, R., Hering, M., Sengupta, S., Peters, S. and Nakamura, E. (2016) The oxygen isotope composition of San Carlos olivine on the VSMOW2-SLAP2 scale. Rapid Commun. Mass Spectrom. **30**, 1495-1504.

280) Tanaka, R. and Nakamura, E. (2017) Silicate–SiO reaction in a protoplanetary disk recorded by oxygen isotopes in chondrules. Nat. Astron. **1**, 0137.

281) Valley, J.W., Kitchen, N., Kohn, M.J., Niendorf, C.R. and Spicuzza, M.J. (1995) UWG-2, a garnet standard for oxygen isotope ratios: Strategies for high precision and accuracy with laser heating. Geoch. Cosmoch. Acta **59**, 5223-5231.

282) Osawa, T. (2004) A new correction technique for mass interferences by $^{40}Ar^{++}$ and CO_2^{++} during isotope analysis of a small amount of Ne. J. Mass. Spectrom. Soc. Japan **52**, 230-232.

283) Busemann, H., Baur, H. and Wieler, R. (2000) Primordial noble gases in “phase Q” in carbonaceous and ordinary chondrites studied by closed-system stepped etching. Meteorit. Planet. Sci. **35**, 949-973.

284) Huss, G.R. and Lewis, R.S. (1994) Noble gases in presolar diamonds I: Three distinct components and their implications for diamond origins. Meteoritics **29**, 791-810.

285) Hohenberg, C., Marti, K., Podosek, F., Reedy, R. and Shirck, J. (1978) Comparisons between observed and predicted cosmogenic noble gases in lunar samples. 9th Lunar and Planetary Science Conference **9**, 2311-2344.

286) Zheng, Y.-F. (1991) Calculation of oxygen isotope fractionation in metal oxides. Geoch. Cosmoch. Acta **55**, 2299-2307.

287) Zheng, Y.-F. (1999) Oxygen isotope fractionation in carbonate and sulfate minerals. Geochem. J. **33**, 109-126.

Supplementary Figures A

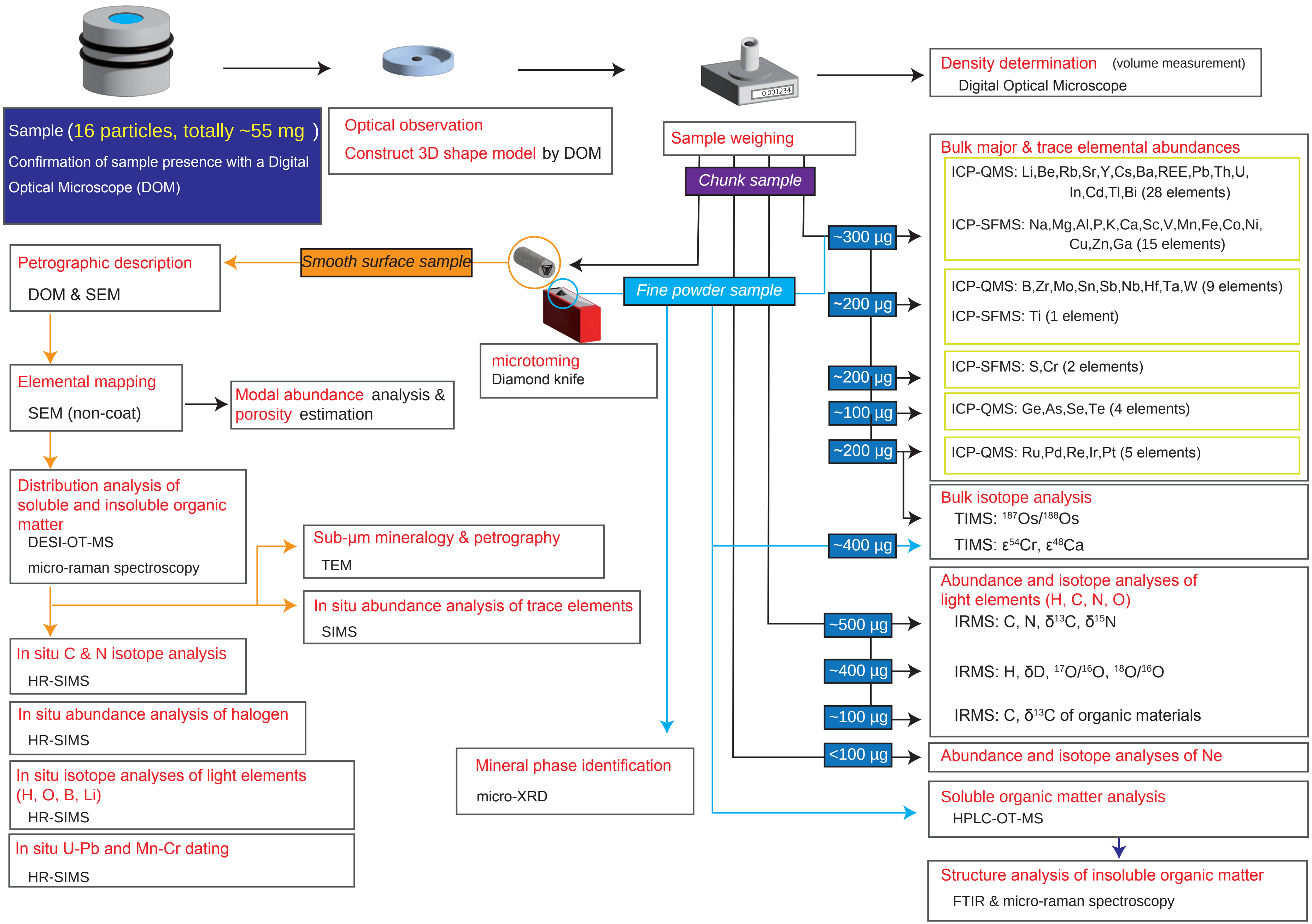

Fig. SA1: The analytical protocol applied to the Ryugu particles in this study.

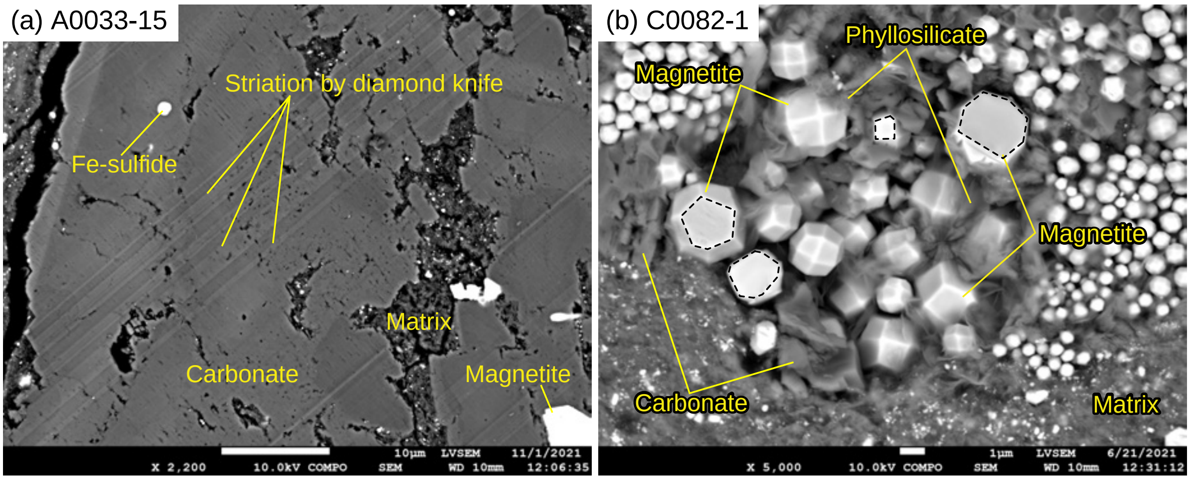

Fig. SA2: BSE images showing artificial surfaces of particles prepared by ultra-microtome. (a) The surface of the carbonate nodule in A0033-15, which is smooth enough for microscopic observation. Artifacts, such as striations, caused by the diamond knife are occasionally observed. (b) The surface of the magnetite nodule in C0082-1, where both the cross-sections (surrounded by dashed lines) and three-dimensional forms of minerals in the pore space can be observed.

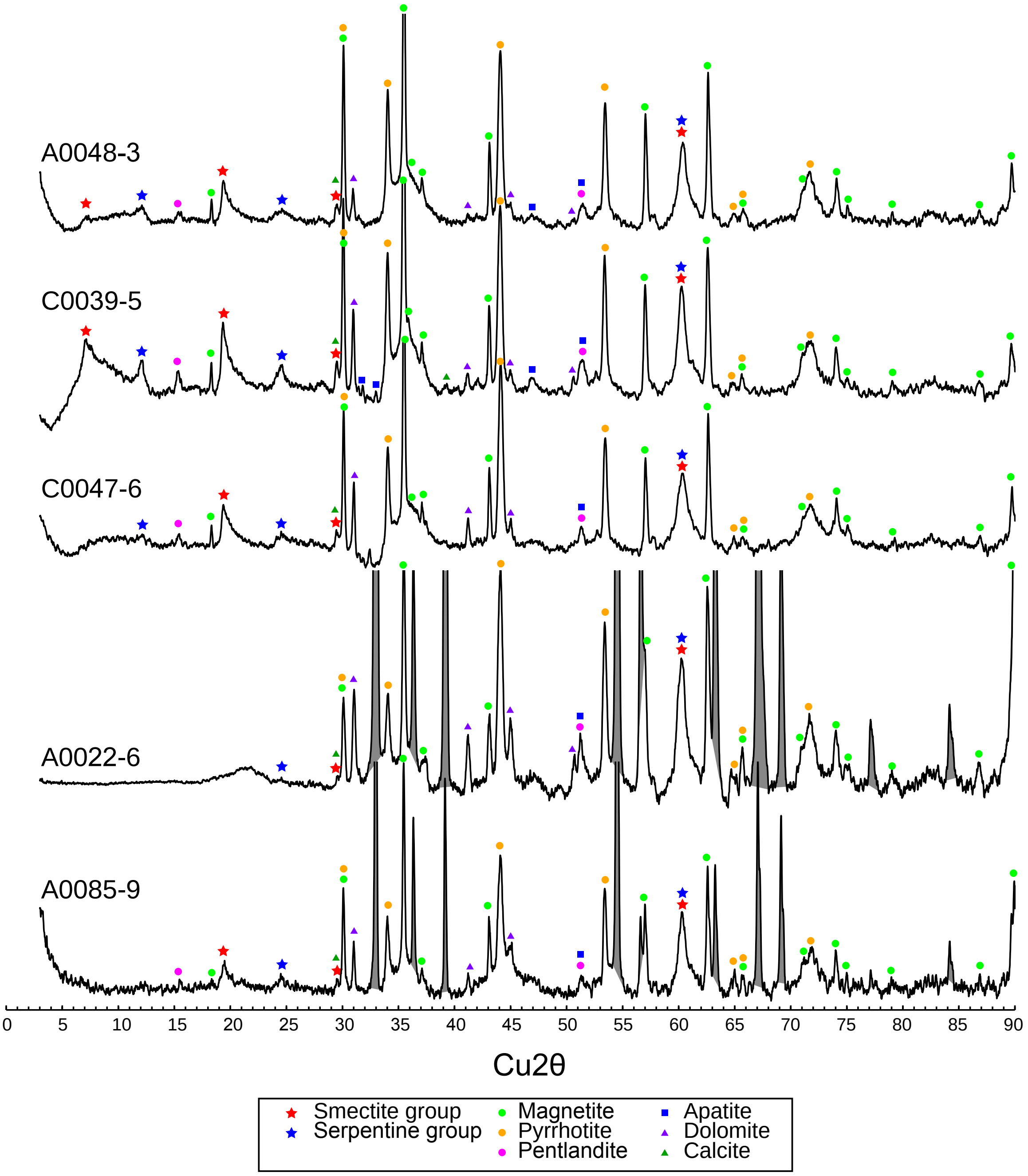

Fig. SA3: The X-ray diffraction patterns obtained from the ultra-microtomed surface of five particles. The peaks shaded in grey in A0022-6 and A0085-9 are those corresponding to the indium used for mounting the particle. Phases of smectite and serpentine group phyllosilicates, saponite, magnetite, pyrrhotite, pentlandite, apatite, dolomite, and calcite were identified in the particles.

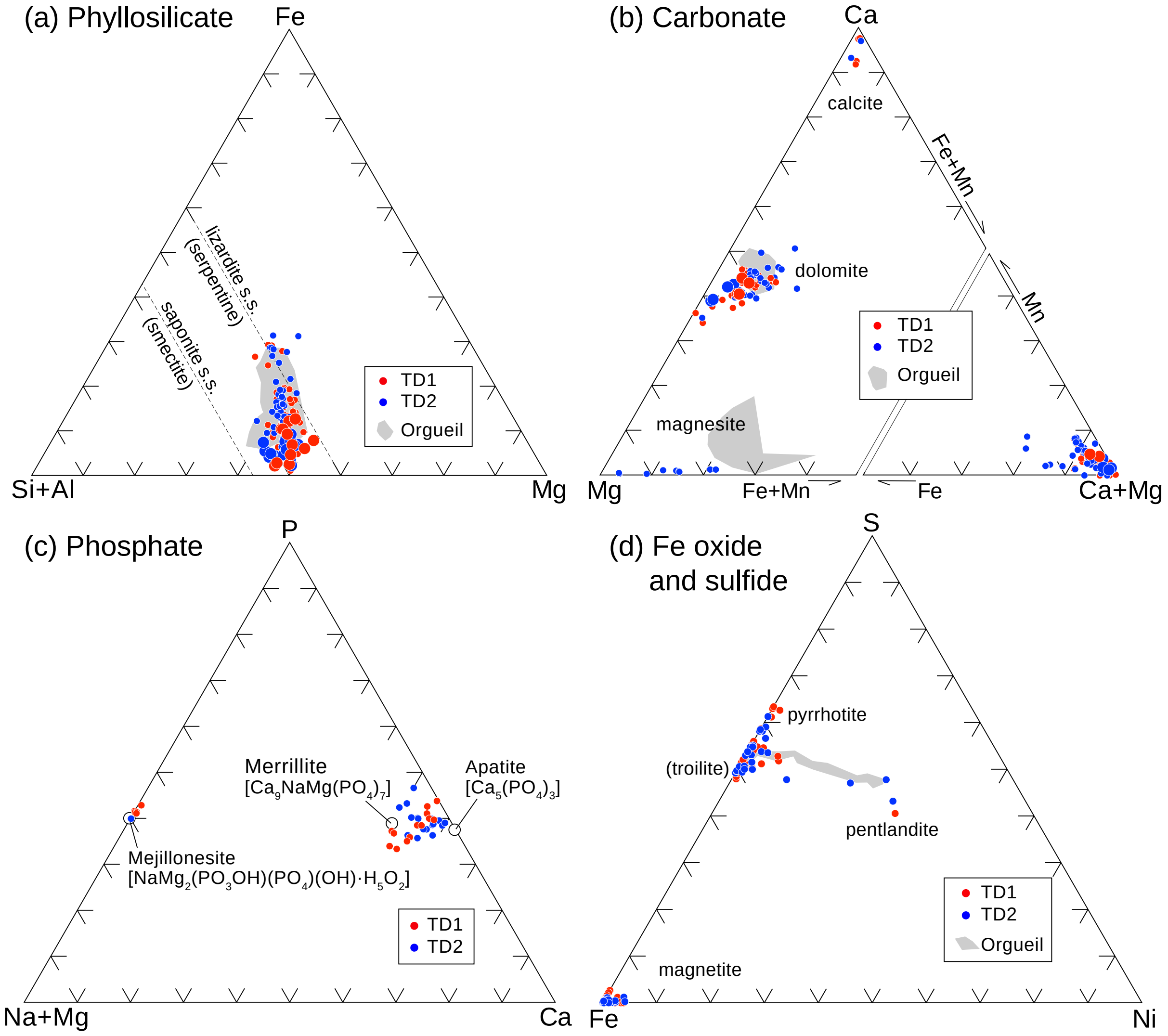

Fig. SA4: Ternary diagrams showing the chemical compositions of (a) phyllosilicate, (b) carbonate, (c) phosphate, and (d) iron oxide and sulfide. The small and large symbols in diagram (a) indicate phyllosilicates in the matrix and those in phyllosilicate nodules, respectively. The small and large symbols in diagram (b) indicate carbonates that are depleted and enriched in rare-earth elements, respectively; see the main text for details. The data for the Orgueil (CI1) are from refs. [246–249].

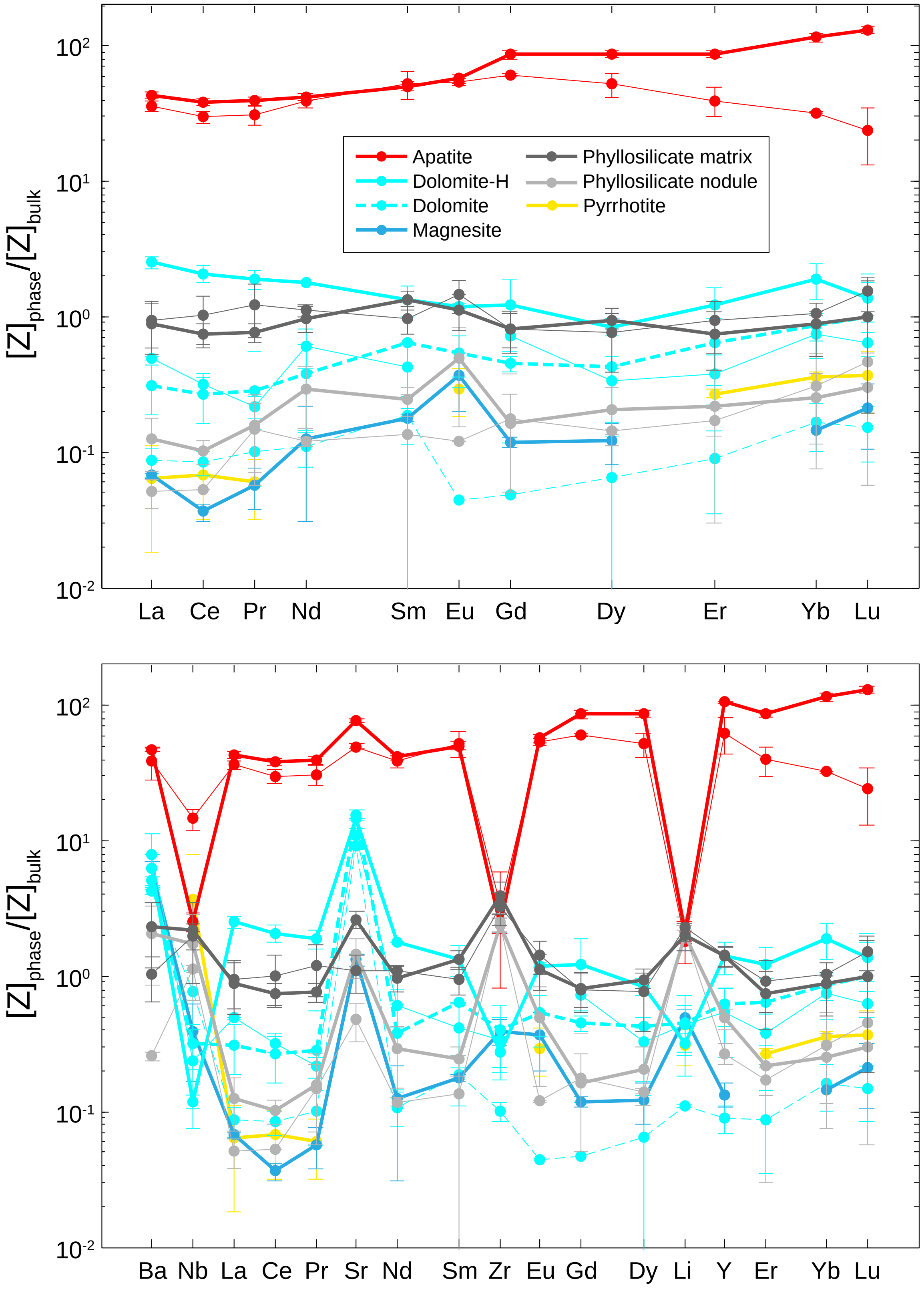

Fig. SA5: Trace element abundances of the major phases and components determined by SIMS. The apatite, dolomite, magnesite and Fe-sulfide phases and the phyllosilicate-dominated matrix and phyllosilicate nodule components were analyzed. The elemental abundance of each phase and component was normalized to the bulk A0033-15 (thin line) and C0053-1 (thick line) values determined by this study. Dolomite that is enriched in LREE is referred to as ‘dolomite-H’.

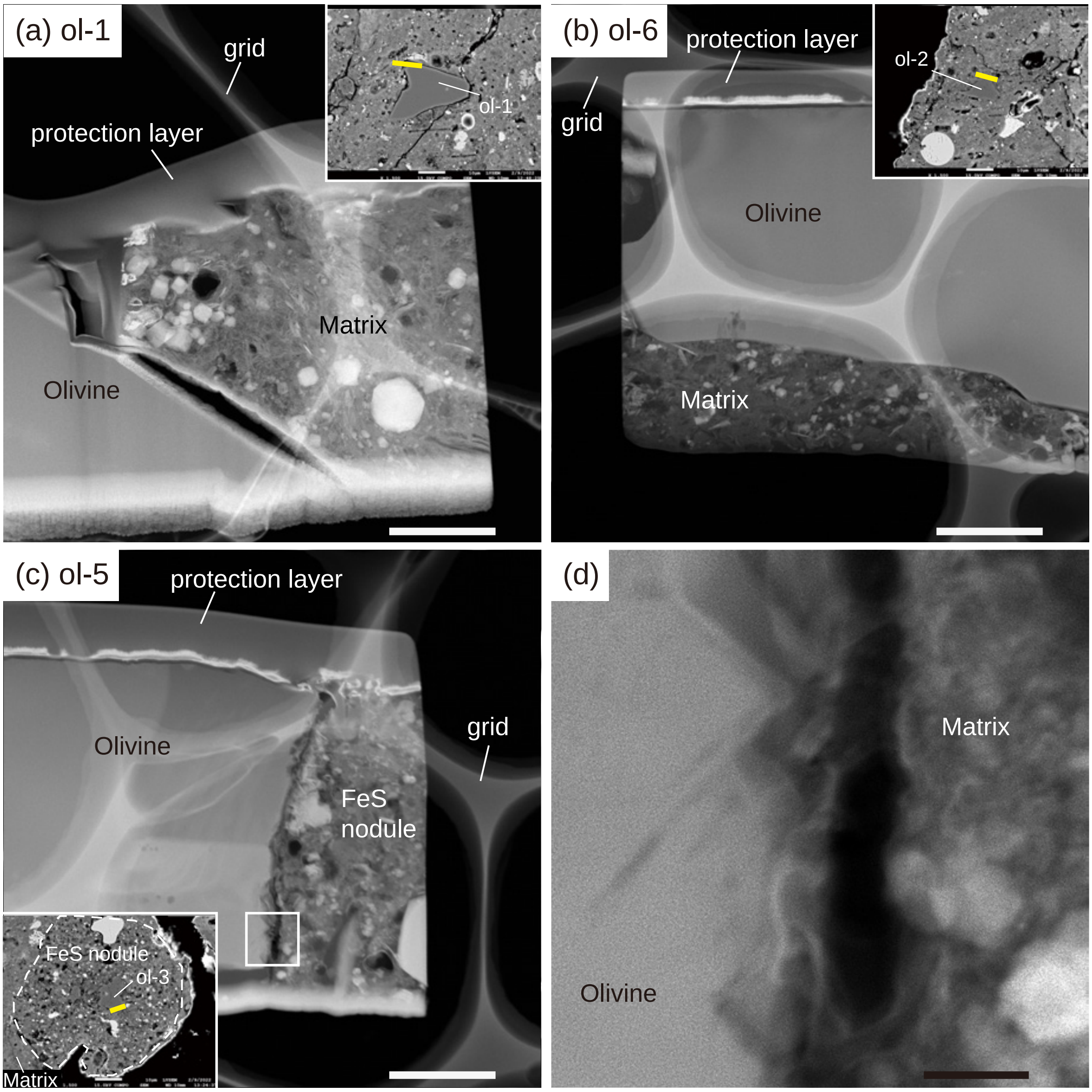

Fig. SA6: Scanning TEM images of angular-shaped (a) olivine-1 (ol-a73-5s2@7055) and (b) olivine-6 (ol-a73-5s2@7079) with matrix, and irregular-shaped (c) olivine-5 (ol-a73-5s2@7068) in an Fe-sulfide nodule from A0073-5, where spot numbers of SIMS analyses were shown in parentheses (see Table S6 for details). (d) An enlarged view of the white rectangle in (c). The scale bars correspond to 1 μm in (a)–(c) and 100 nm in (d). The locations where TEM films were fabricated are shown as yellow bars on the BSE images shown in the subpanels (the subpanels scale bars correspond to 10 μm). The white area located on the top of each film is a protection layer accumulated during sample preparation. The magnified image of the interface shown in (d) demonstrates that the olivine fragment has an angular surface that has been formed by mechanical fracturing. No significant reaction layer is observed.

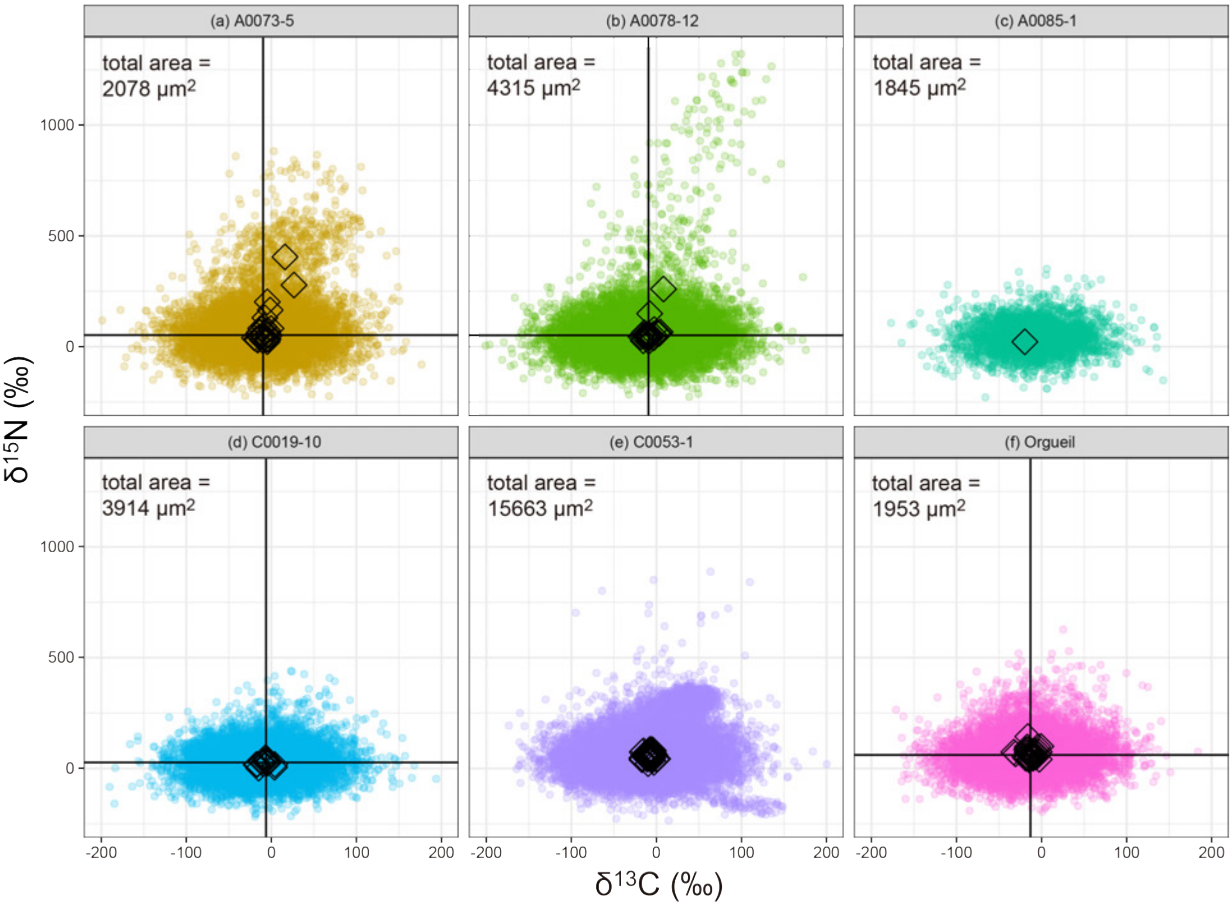

Fig. SA7: δ^{13}C and δ^{15}N obtained from pixel-by-pixel, area, and whole-rock analyses. The colored circle, empty diamond, and crossed line corresponds to pixel-by-pixel (pixels extracted from maps), area (whole 15 μm × 15 μm and 50 μm × 50 μm maps), and whole-rock analyses, respectively. Pixels with integration of $^{12}C^{14}N^{-}$ ions < 1000 and $^{12}C^{12}C^{-}$ ions < 100 are not shown. (a) A0073-5, (b) A0078-12, (c) A0085-1, (d) C0019-10, (e) C0053-1, and (f) Orgueil (CI1).

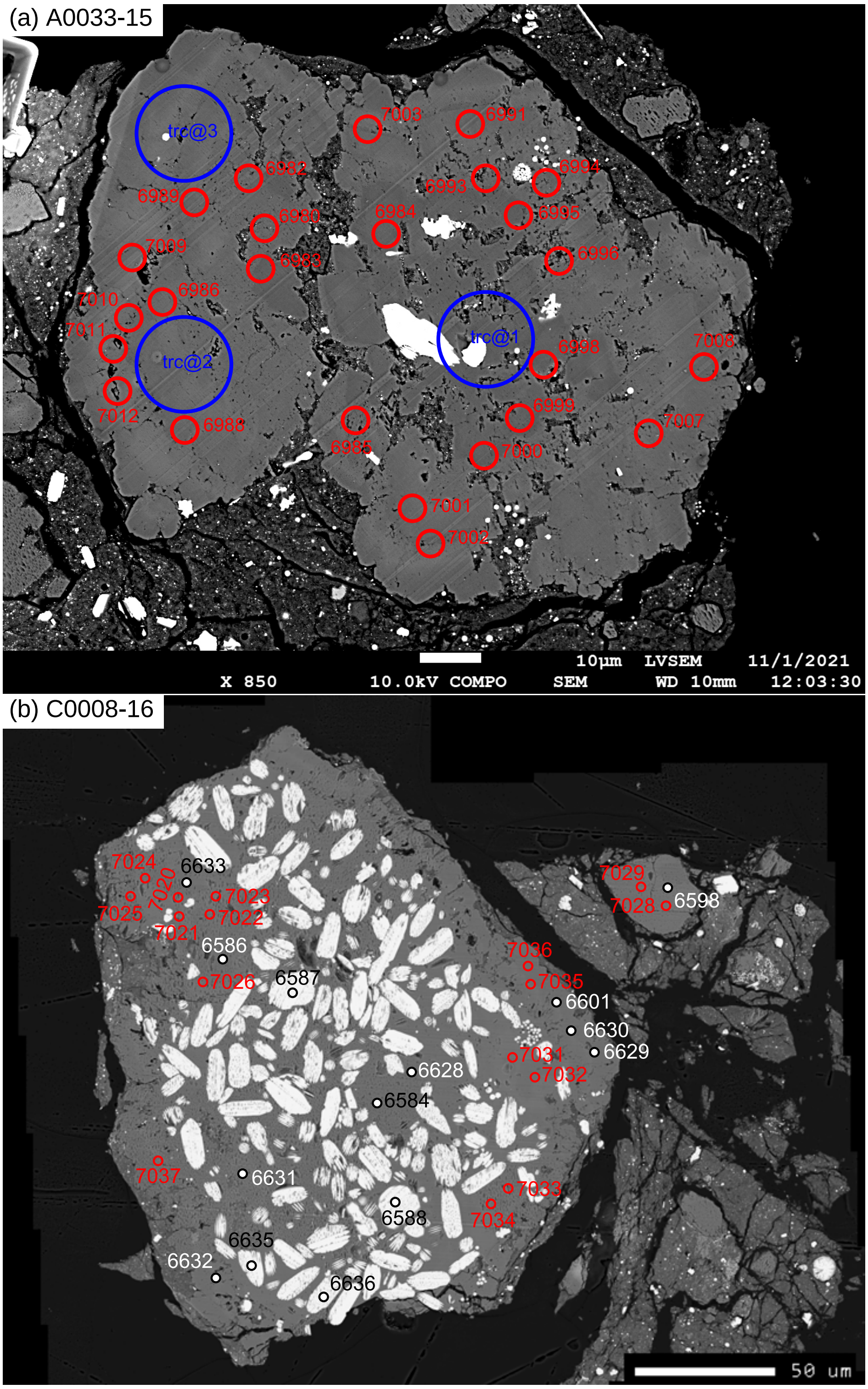

Fig. SA8: BSE images showing SIMS spots for (a) trace element and Mn-Cr isotopic analyses on the carbonate nodule in A0033-15 and (b) O and Mn-Cr isotopic analyses on the magnetite-carbonate nodule in C0008-16. Spots for trace element, Mn-Cr isotopic, and O isotopic analyses are shown by blue, red, and black circles, respectively.

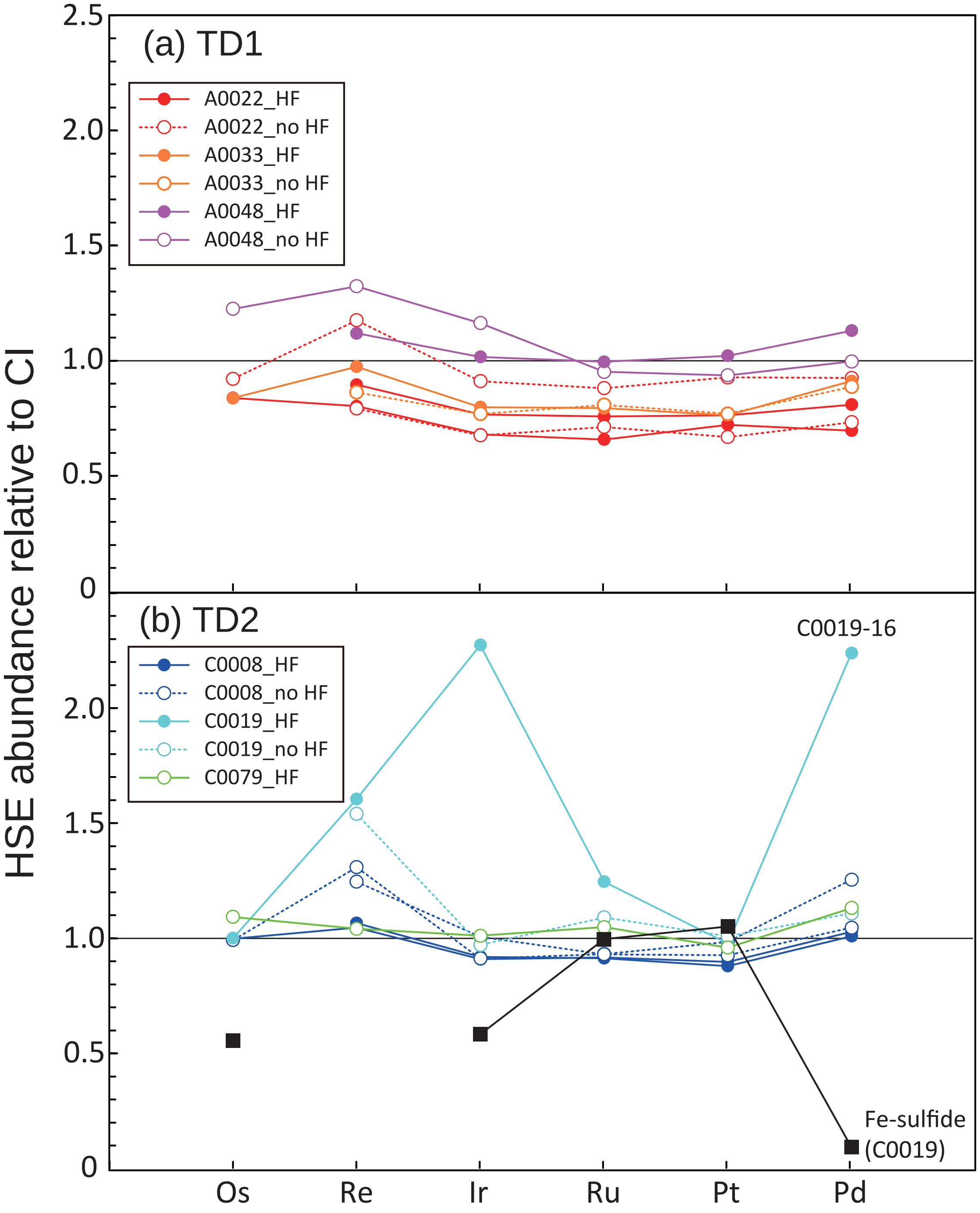

Fig. SA9: Individual data of highly siderophile elements of (a) TD1 particles and (b) TD2 particles plotted relative to CI chondrites [43)]. Particles digested with and without HF are shown with a filled circle with solid line and open circles with broken line, respectively. The filled squares are Fe-sulfide separates from C0019. Because the absolute abundances of HSE in the Fe-sulfides were not accurately determined, the values were normalized as $[Ru]/[Ru]_{CI} = 1$, where $[Ru]_{CI}$ is Ru abundance of CI chondrites.

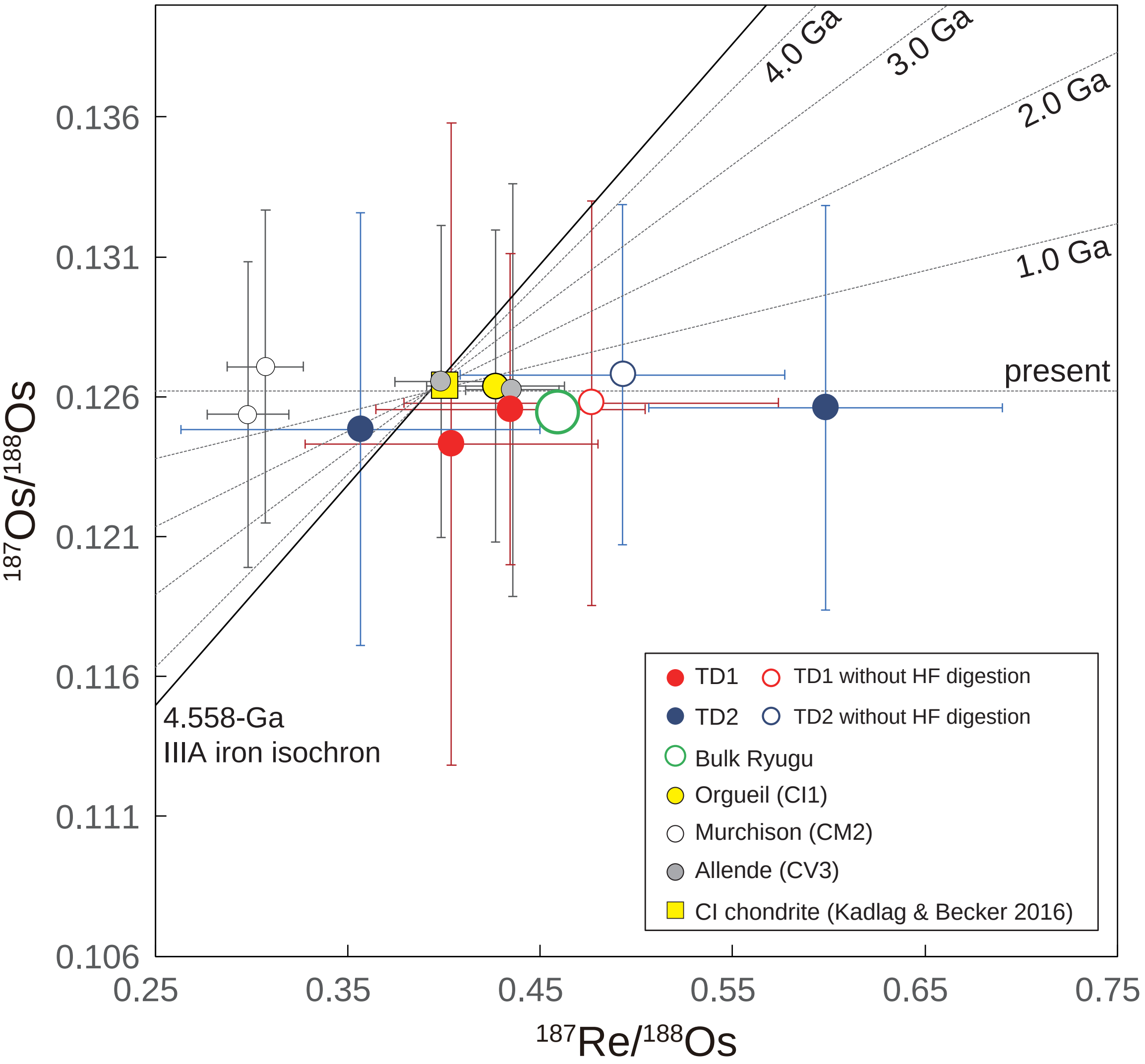

Fig. SA10: ^{187}Re/^{188}Os vs. ^{187}Os/^{188}Os for Ryugu particles. The data for Orgueil (CI1), Murchison (CM2), and Allende (CV3) measured in this study are also plotted. Bulk Ryugu is the weighted mean value of all Ryugu data. The error bars are 2SE after blank correction. All data are presented in Table S13. The data for CI chondrites is a compiled value [249)]. The solid line is the 4.558-Ga isochron obtained by IIIA iron meteorites [48)]. The broken lines are calculated isochron calculated for each age. Details are described in Supplementary Text ST1.4.5.

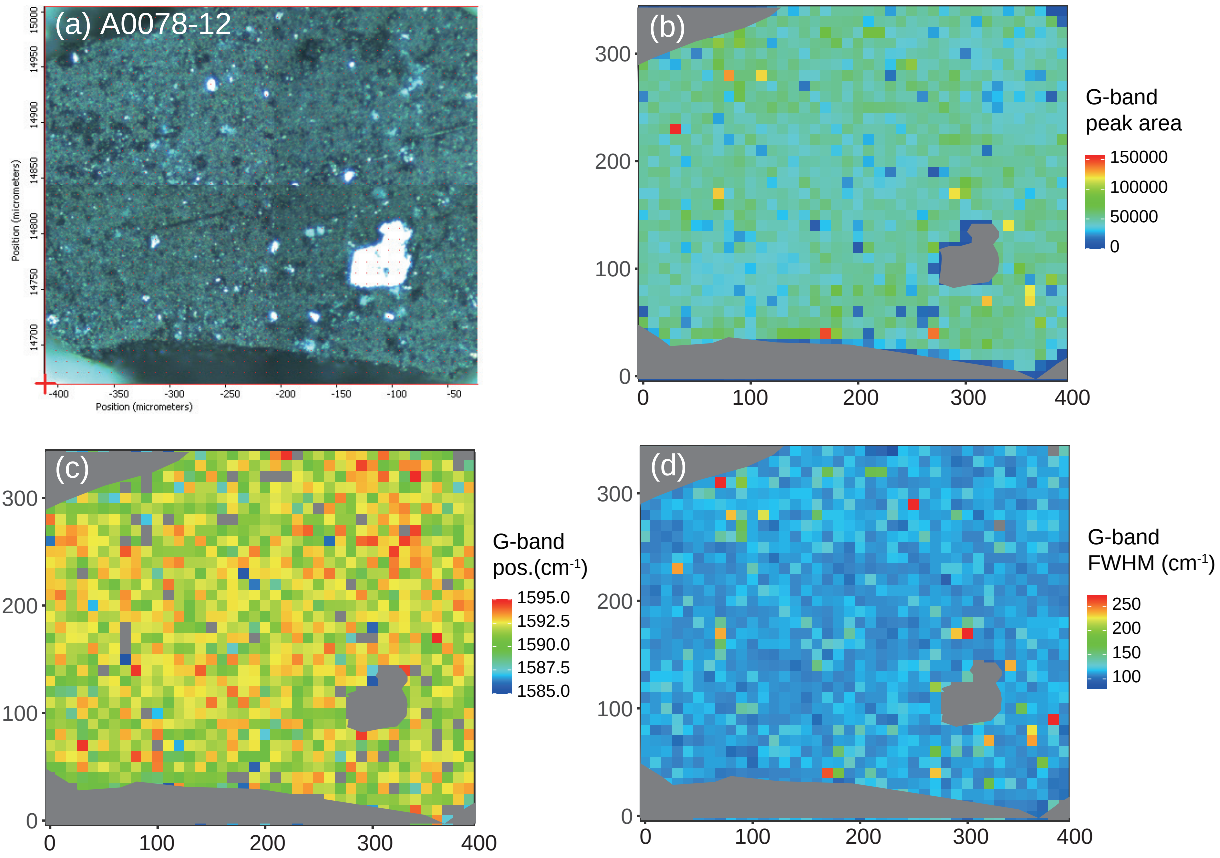

Fig. SA11: Representative Raman maps from A0078-12. (a) Optical image of the A0078-12 surface, (b) G-band peak area, (c) G-band peak position (cm^{-1}), and (d) the FWHM (full width at half maximum) of the G-band peak. FOV is 400 μm × 330 μm.

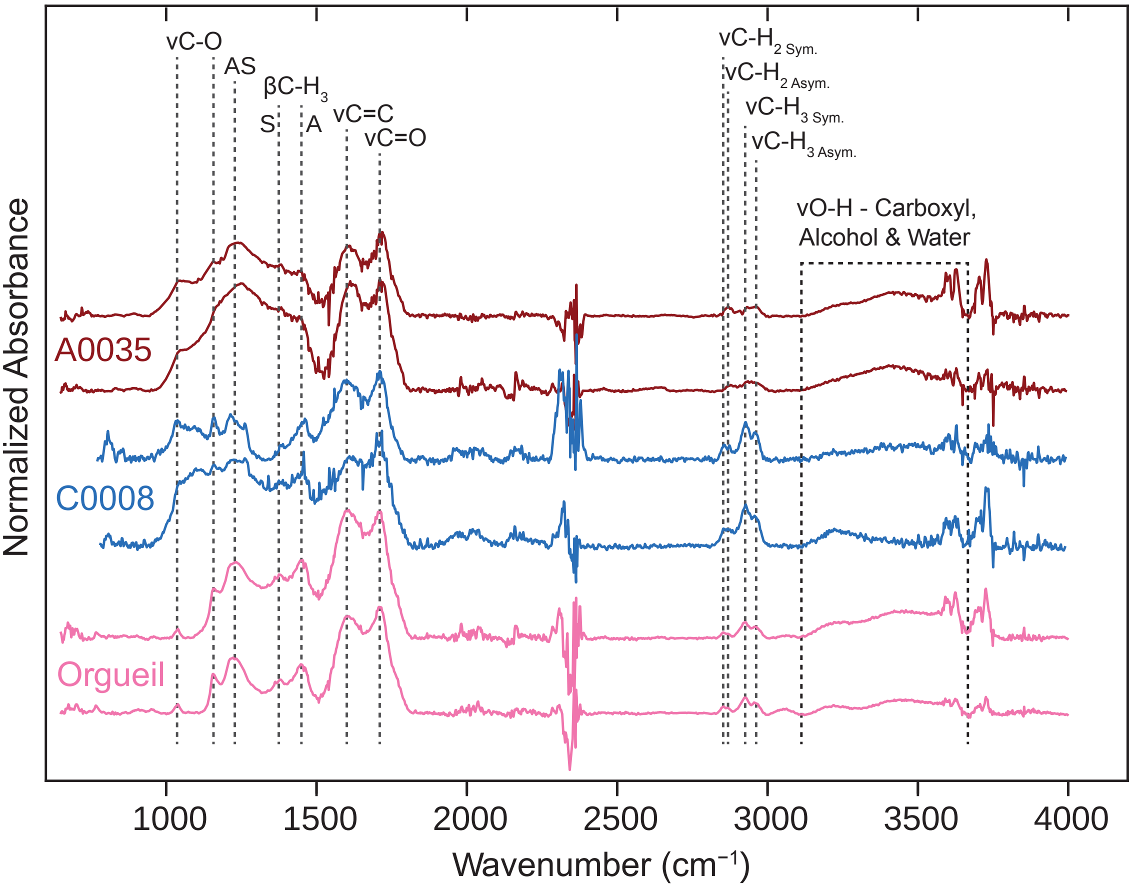

Fig. SA12: The FTIR response for Ryugu and Orgueil(CI1). The measurements were undertaken on IOM extracted from demineralized samples. The major vibrational modes of interest have been annotated on the figure. AS. = aromatic, Skel. = skeletal, ν = stretching vibration, β = bending vibration, Sym. = symmetric, Asym. = asymmetric and Ali = aliphatic. Note that A and S for βC-H refer to the symmetric and asymmetric modes, respectively.

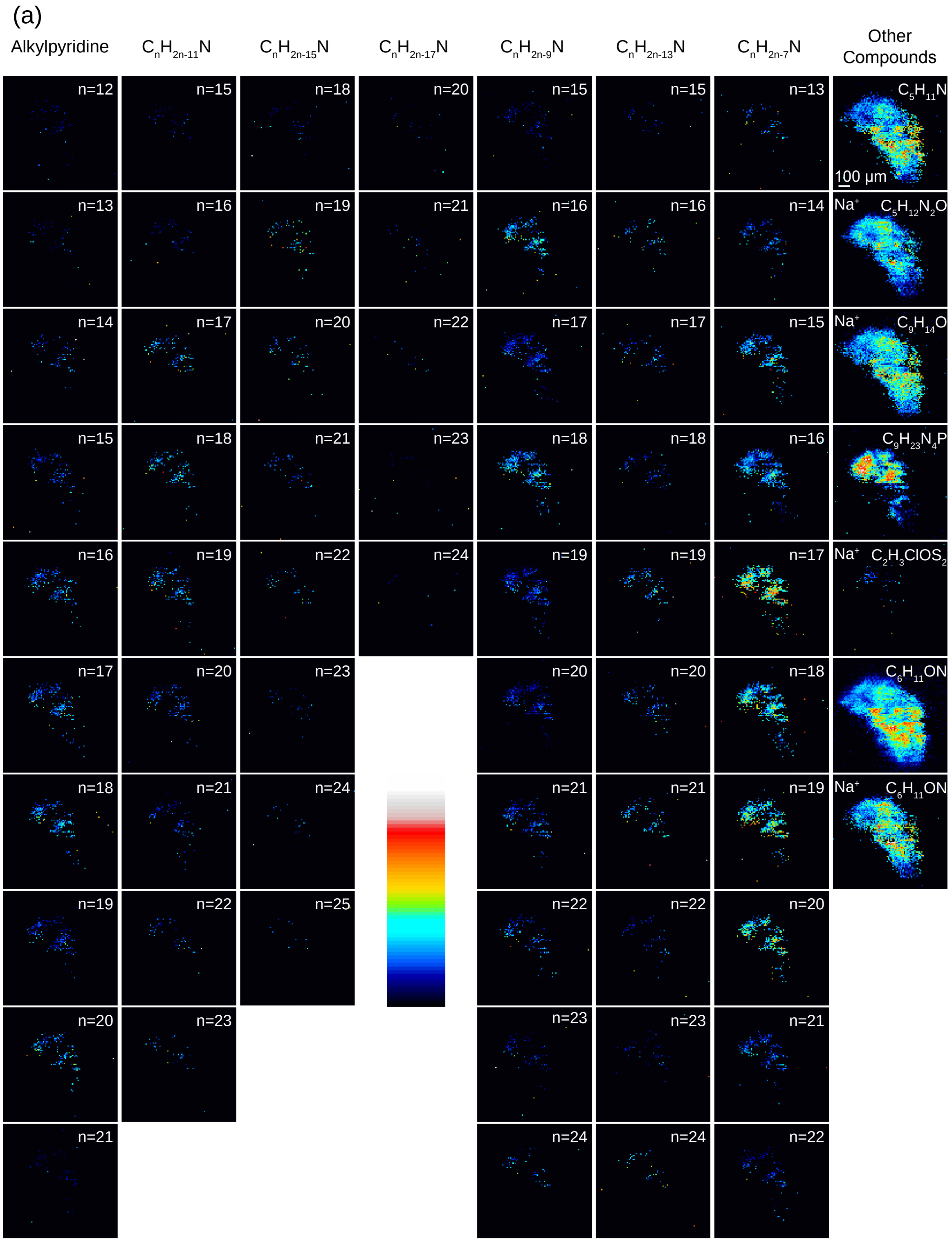

Fig. SA13: Ion intensity maps from (a) C0008-15 and (b) A0048-10 for the different homologue series and compounds identified, which were normalized to the total ion chromatogram (TIC). Note that the homologue general formula is indicated at the top of each column and the number of C present in each homologue member is represented in the top right corner of each image. For the non-homologue compounds, the chemical formula is indicated in the top right corner of each image and a Na^+ is used to indicate those compounds that were detected as a sodium adduct. The color scale has been placed in the middle of the figure and it is a rainbow style scale ranging from black (lowest values) to white (highest values).

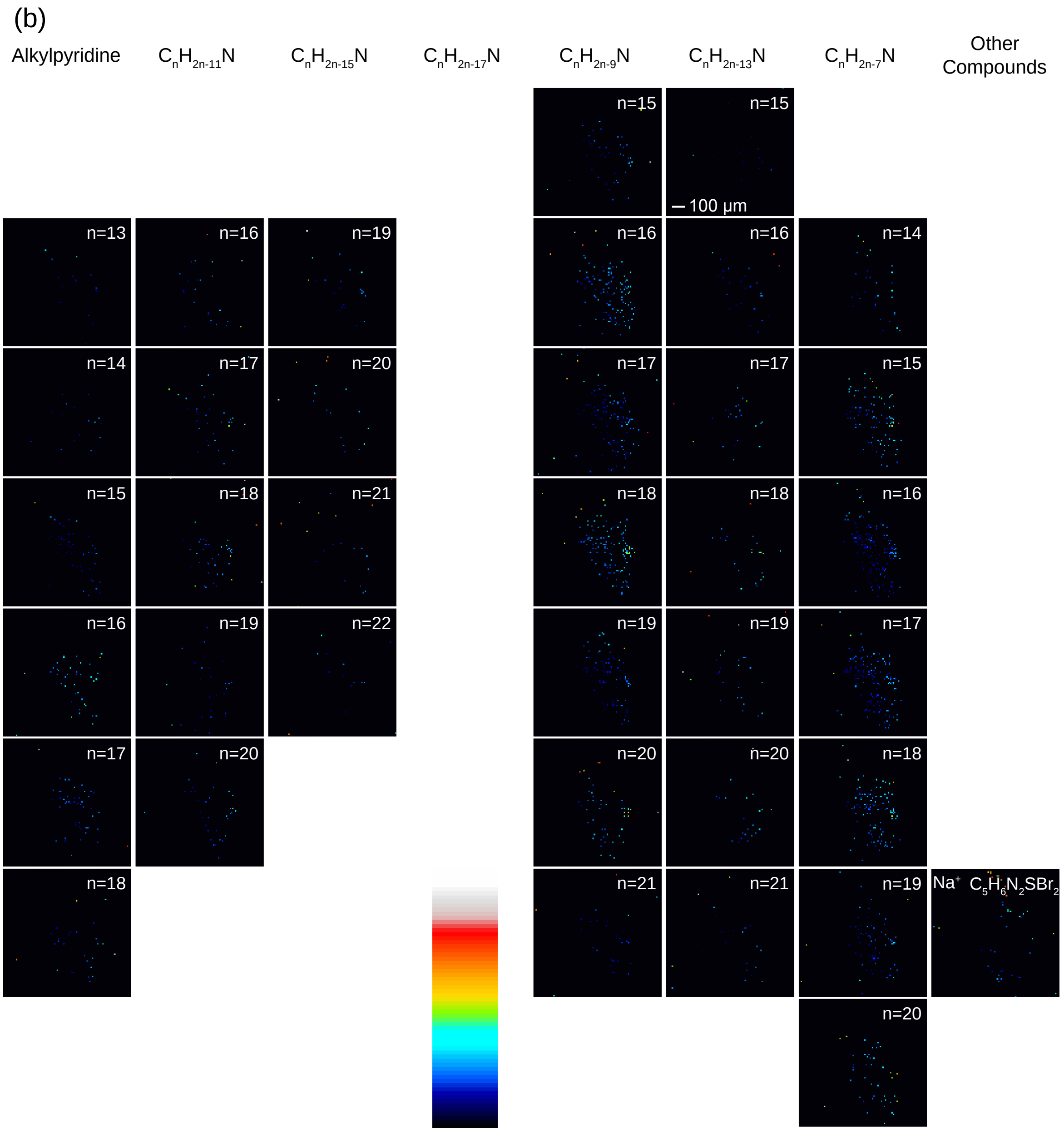

Fig. SA13: Continued

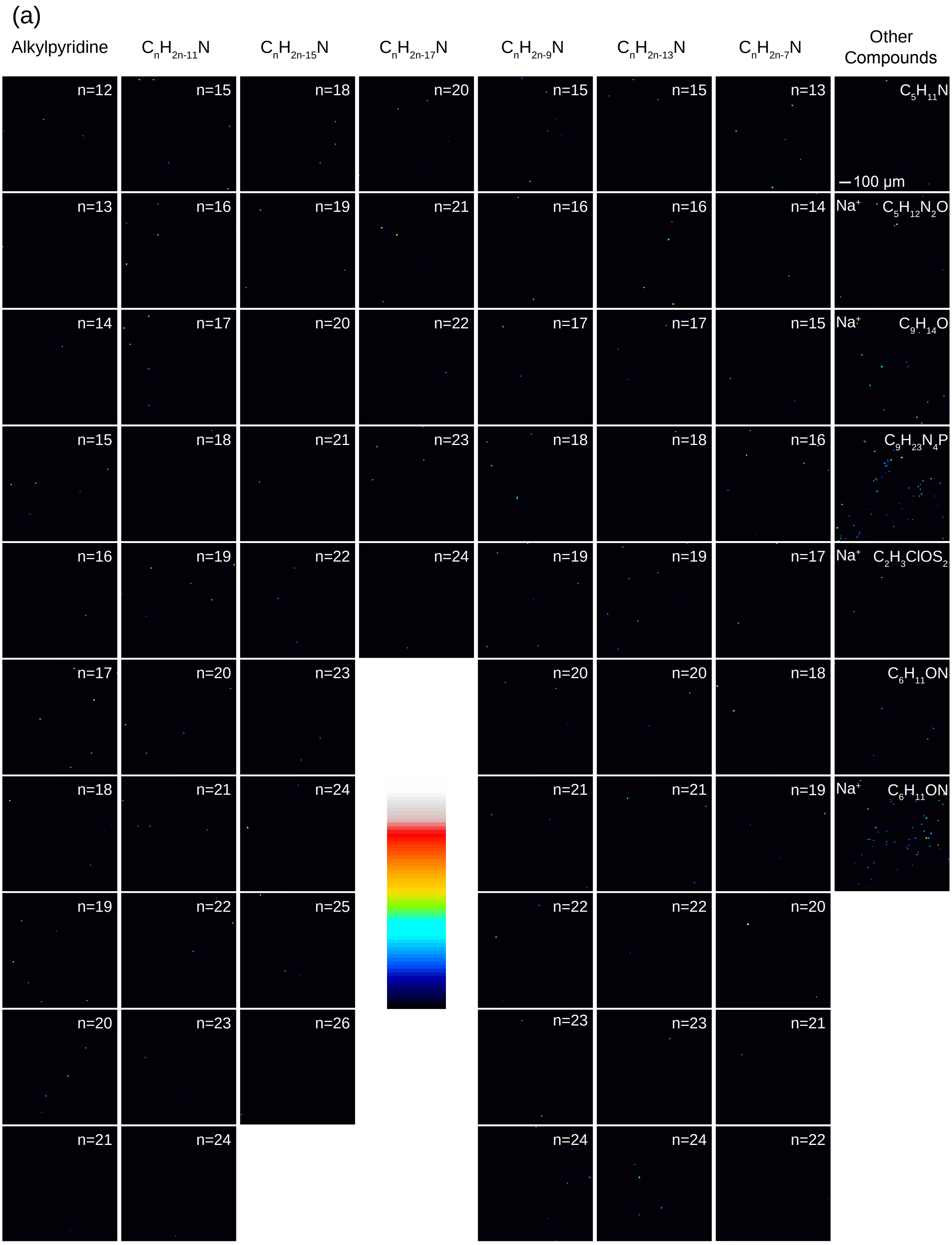

Fig. SA14: Ion intensity maps from the blank for (a) C0008-15 and (b) A0048-10 for the different homologue series and compounds identified, which were normalized to the total ion chromatogram (TIC). Note that the homologue general formula is indicated at the top of each column and the number of C present in each homologue member is represented in the top right corner of each image. For the non-homologue compounds, the chemical formula is indicated in the top right corner of each image and a Na^+ is used to indicate those compounds that were detected as a sodium adduct. The color scale has been placed in the middle of the figure and it is a rainbow style scale ranging from black (lowest values) to white (highest values).

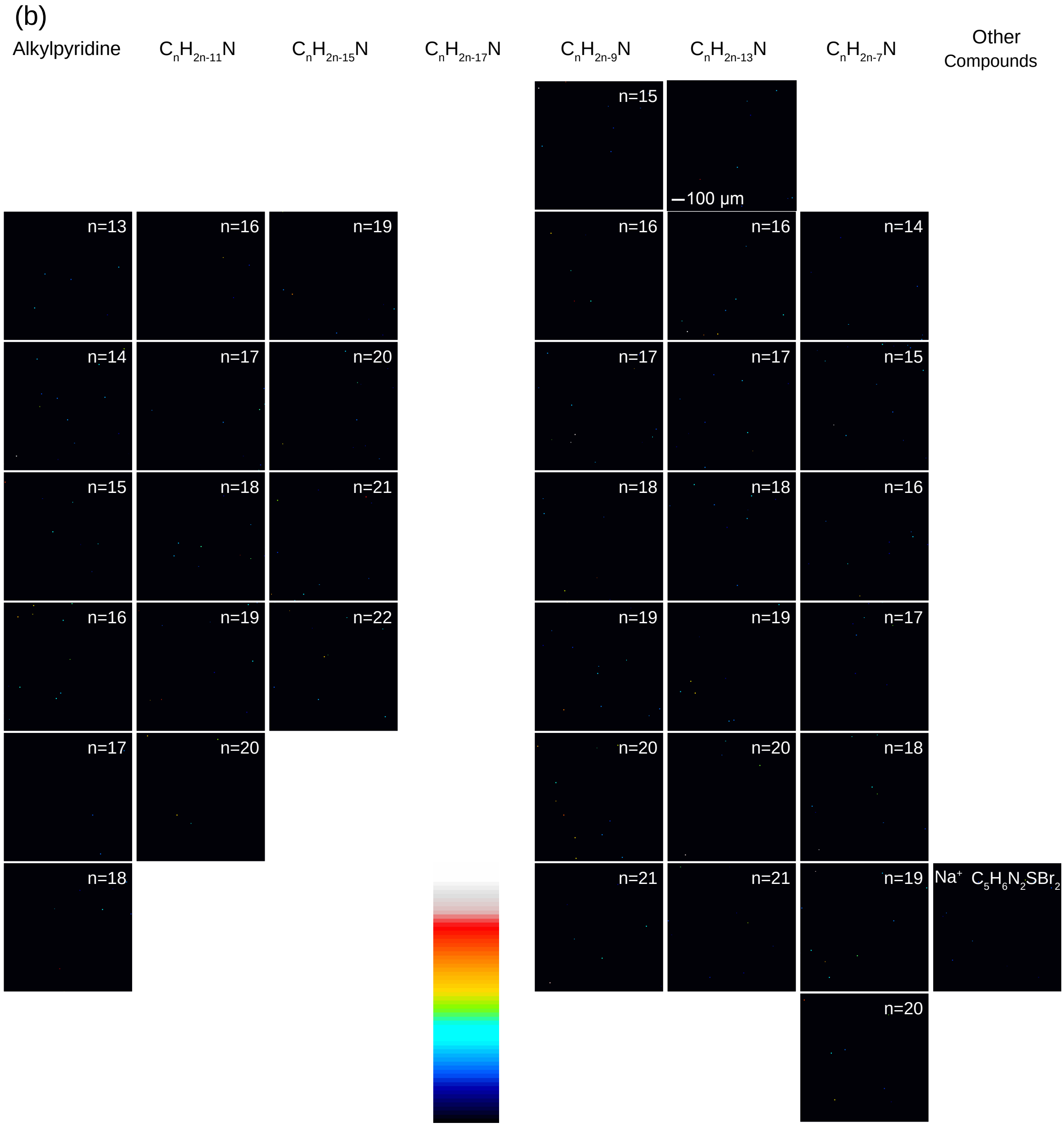

Fig. SA14: Continued

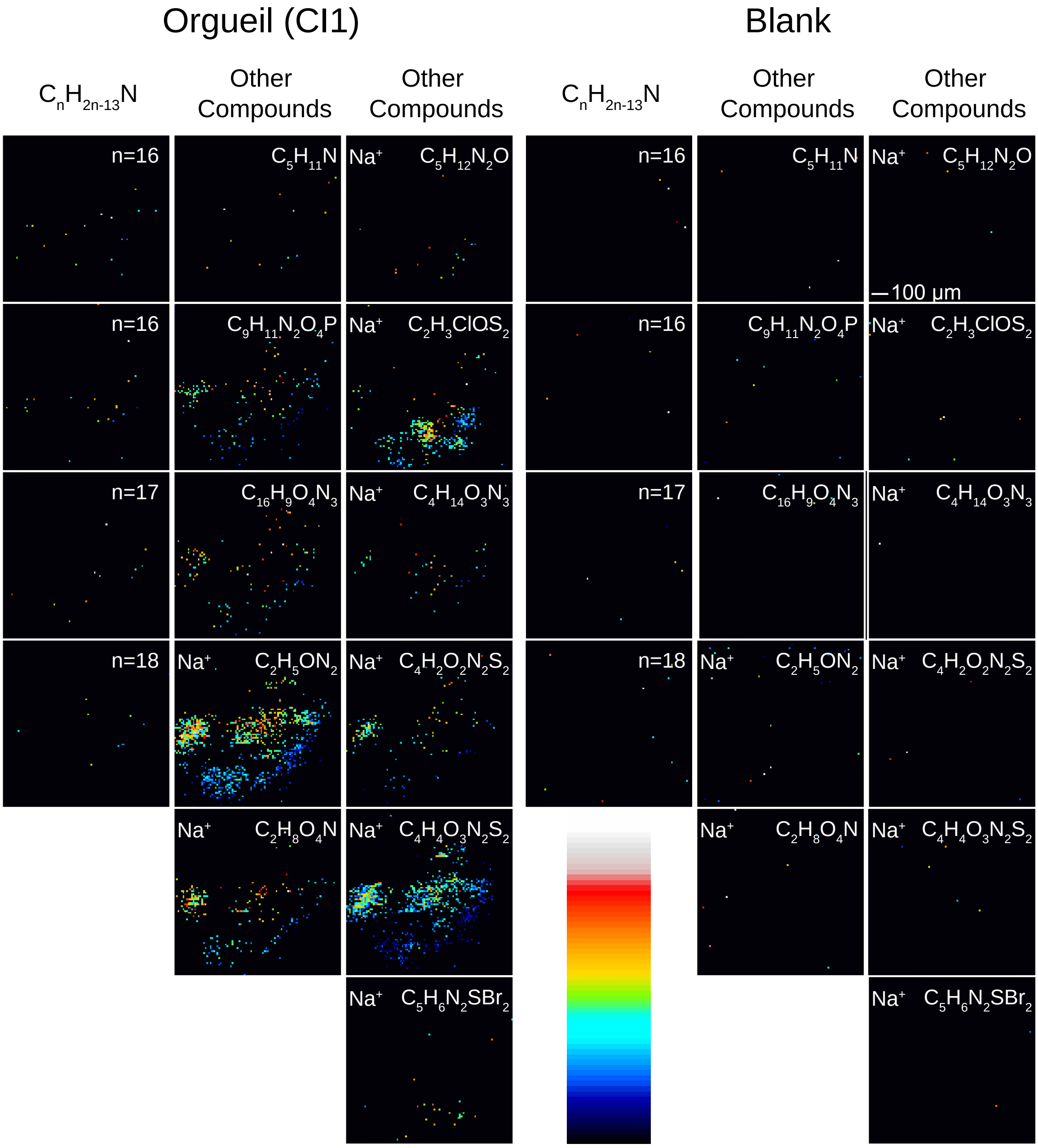

Fig. SA15: Ion intensity maps from Orgueil (CI1) and the corresponding serpentinite blank for the different homologue series and compounds identified, which were normalized to the total ion chromatogram (TIC). Note that the homologue general formula is indicated at the top of each column and the number of carbons present in each homologue member is represented in the top right corner of each image. For the non-homologue compounds, the chemical formula is indicated in the top right corner of each image. The color scale has been placed in the middle of the figure and it is a rainbow style scale ranging from black (lowest values) to white (highest values).

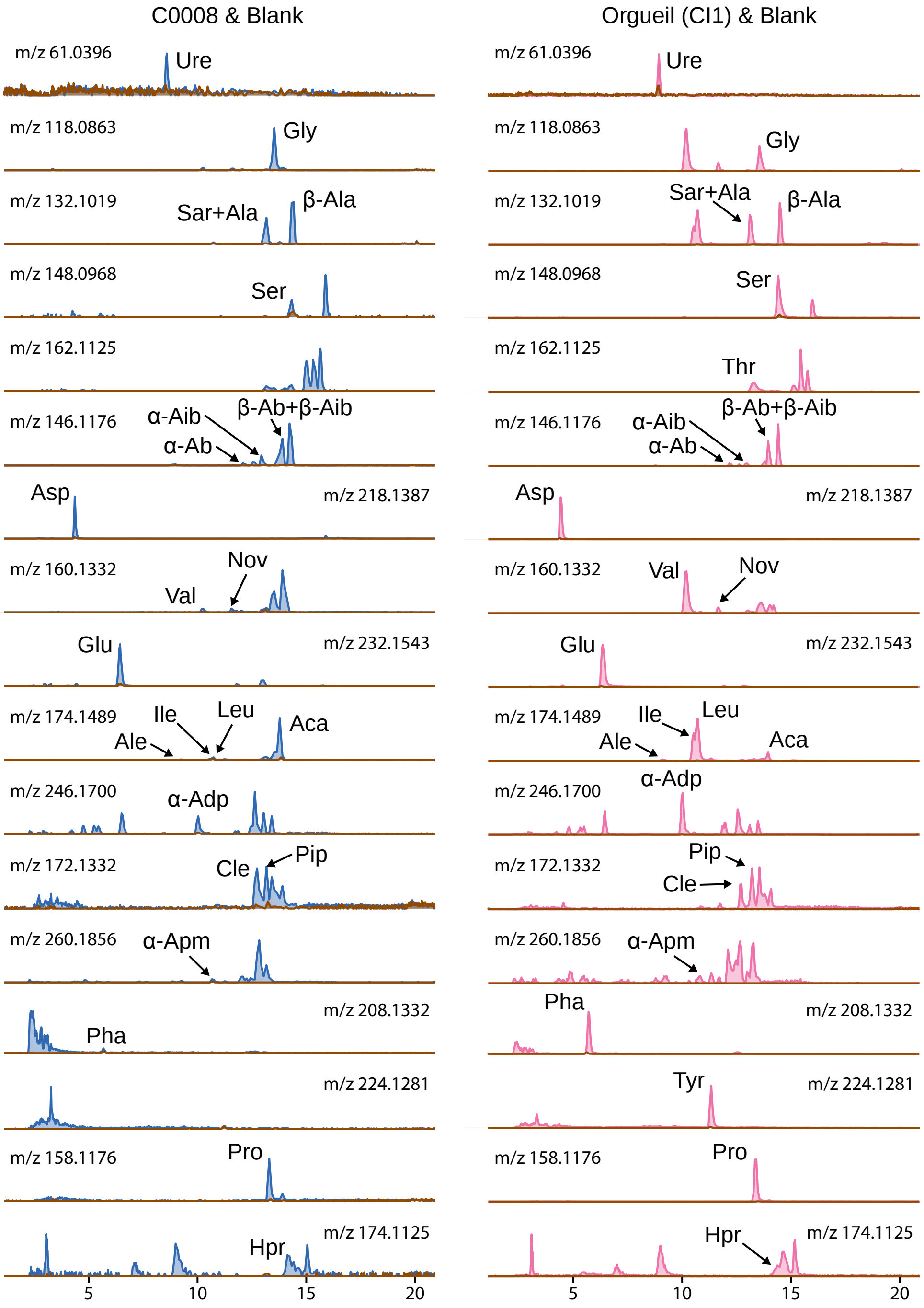

Fig. SA16: Extracted chromatograms for the organic compounds detected within C0008 and Orgueil (CI1). With the exception of Urea, all the compounds shown are amino acids, which were derivatized to isopropyl esters. The red trace indicates the blank, whilst the green trace indicates the sample. It is clear that in all cases the response from the sample is higher than that of the blank. Shorthand codes have been used to label the peaks, which are explained in Table S20. Almost all of the amino acids identified here can be found in both C0008 and Orgueil, the exception being Tyrosine, which is not present in C0008. Although there are major similarities in the amino acids identified between C0008 and Orgueil, there are clear differences in the ratios between them for each sample. For example, valine and norvaline are almost 1:1 in C0008, but in Orgueil the valine peak is much larger than the norvaline peak. Furthermore, there are many unidentified compounds observed in C0008 and Ryugu and these also record different responses.

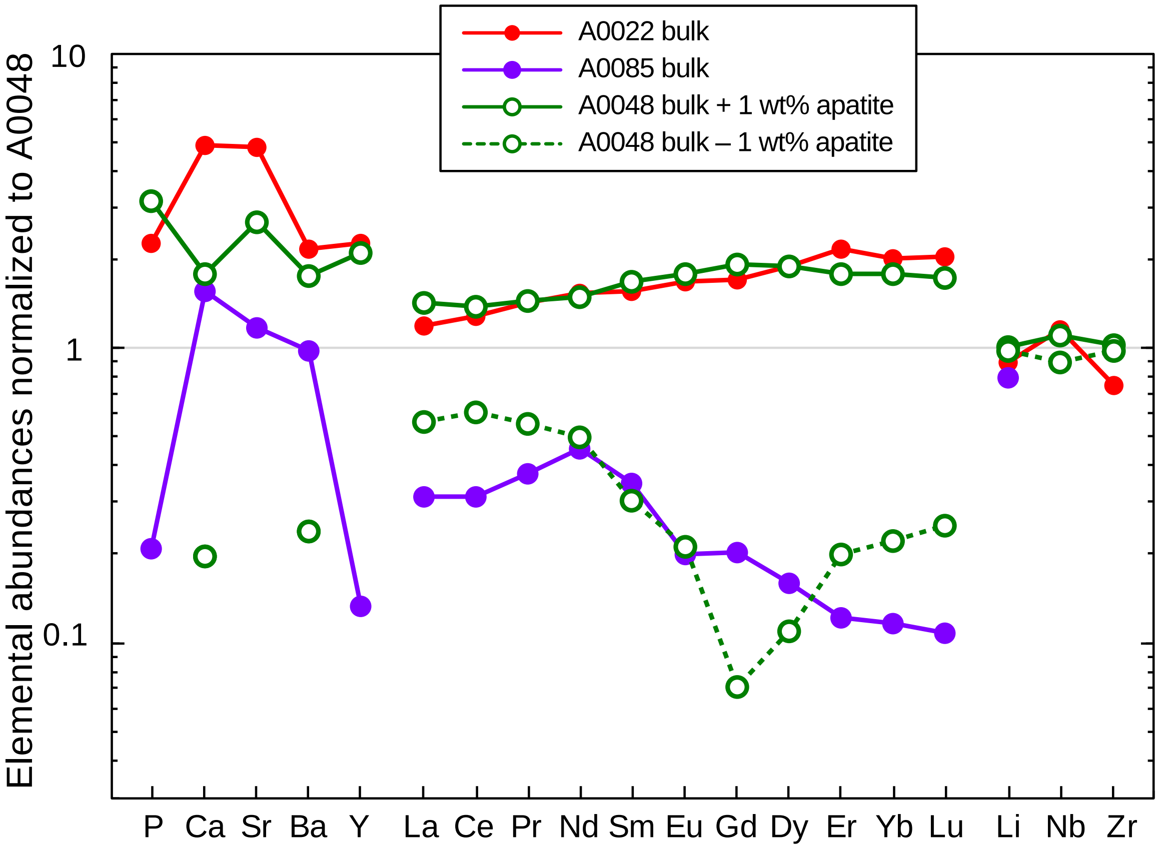

Fig. SA17: A multi-element diagram showing the measured and modeled bulk elemental abundances of the TD1 particles, normalized to the measured bulk elemental abundances of A0048. The modeled abundances were calculated using the bulk abundances of A0048 and the average (n=3) of the apatite abundances determined by SIMS. Elemental abundances of the A0048 bulk plus 1 wt% of the apatite reproduce those of the A0022 bulk, considering the contributions of Ca and Sr in carbonate. The low abundances of Li, Nb, and Zr of the apatite do not contribute to the variation of the elemental abundances of the TD1 particles. The elemental abundances of A0048 minus 1 wt% of the apatite yield, relative to the A0085 bulk, excess in light and heavy rare earth elements, and deficit in P, Ca, Sr, Ba, Y and middle rare earth elements.

Supplementary Figures B

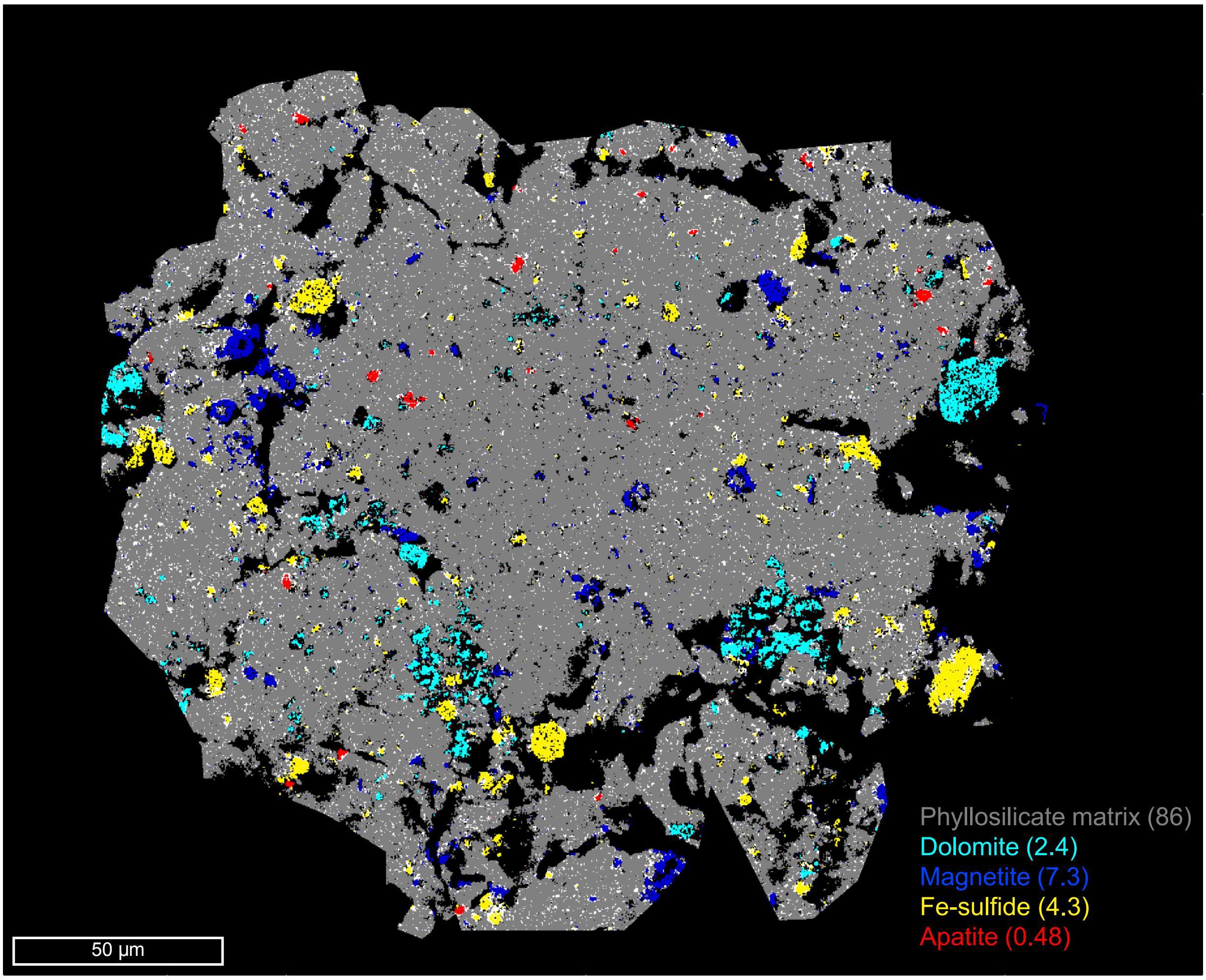

Fig. SB1: Phasemap of A0022-6. In parenthesis is modal abundance (%) of phase or component.

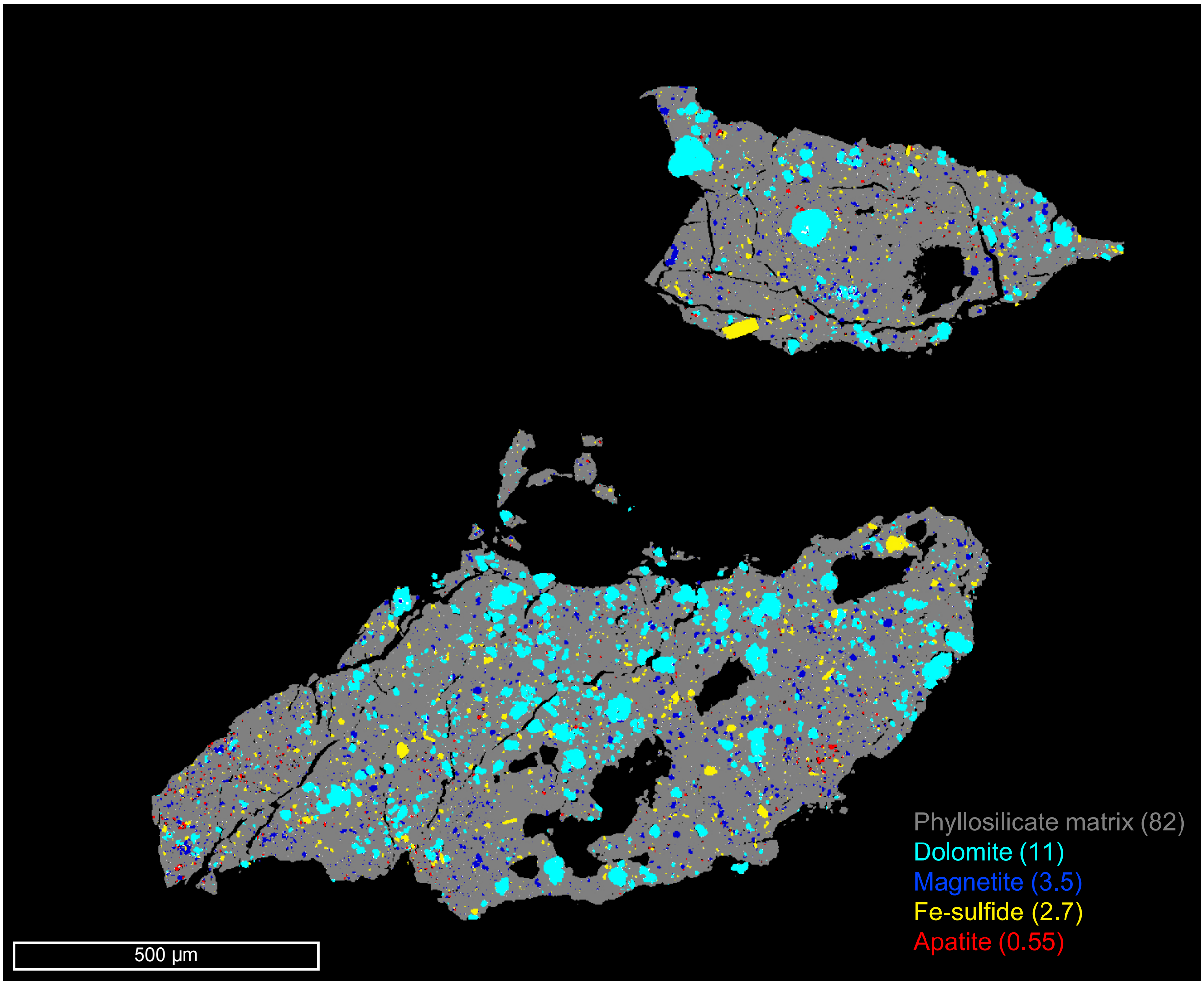

Fig. SB2: Phasemap of A0022-15. In parenthesis is modal abundance (%) of phase or component.

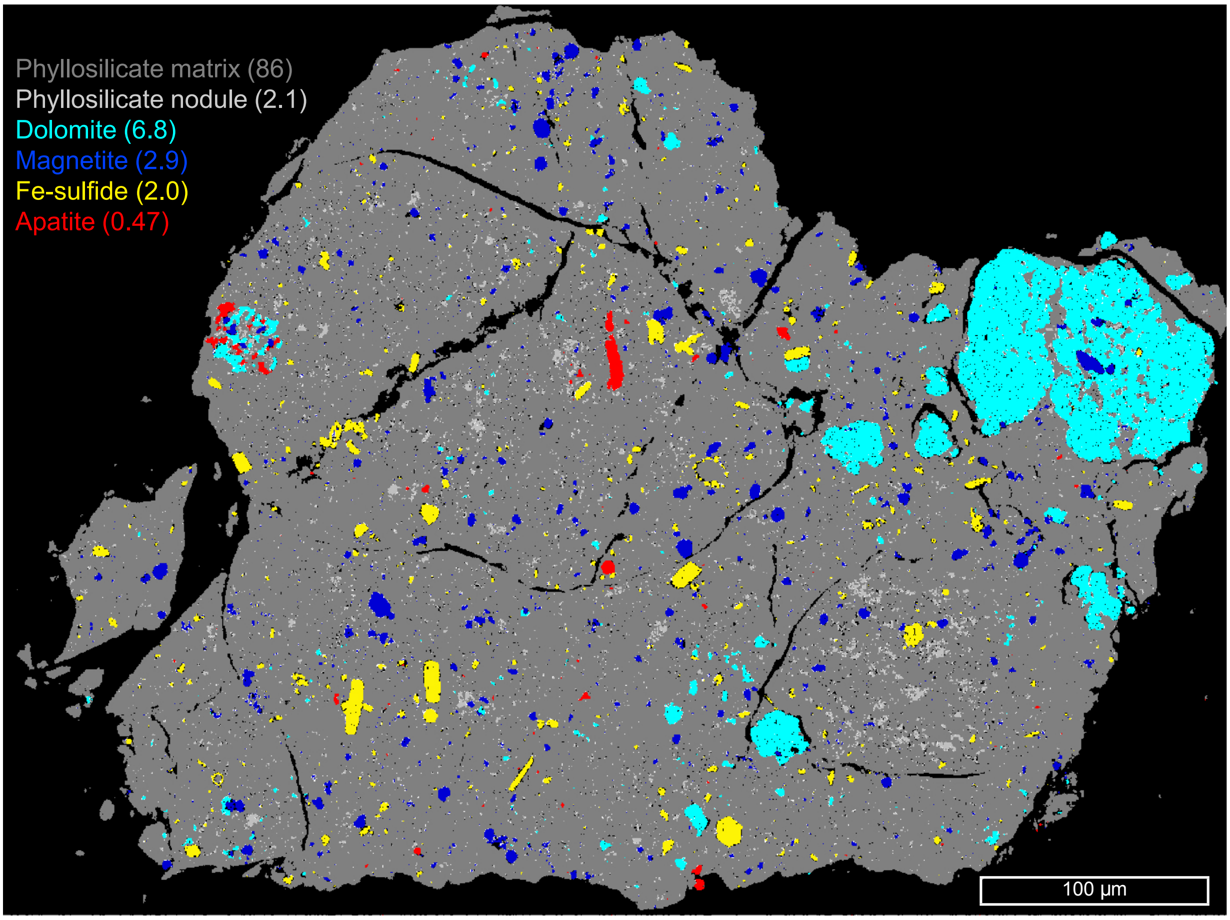

Fig. SB3: Phasemap of A0033-15. In parenthesis is modal abundance (%) of phase or component.

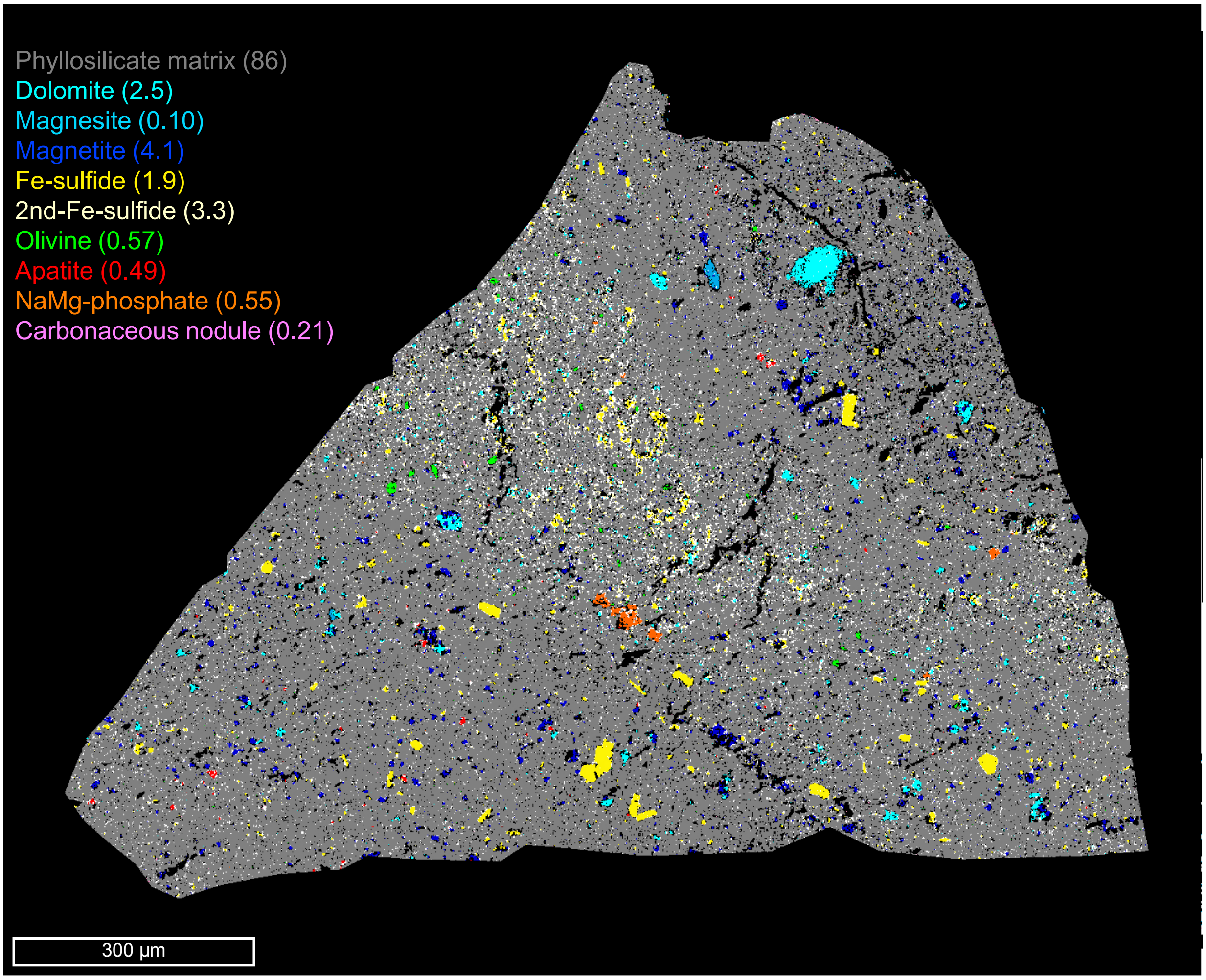

Fig. SB4: Phasemap of A0035-1. In parenthesis is modal abundance (%) of phase or component.

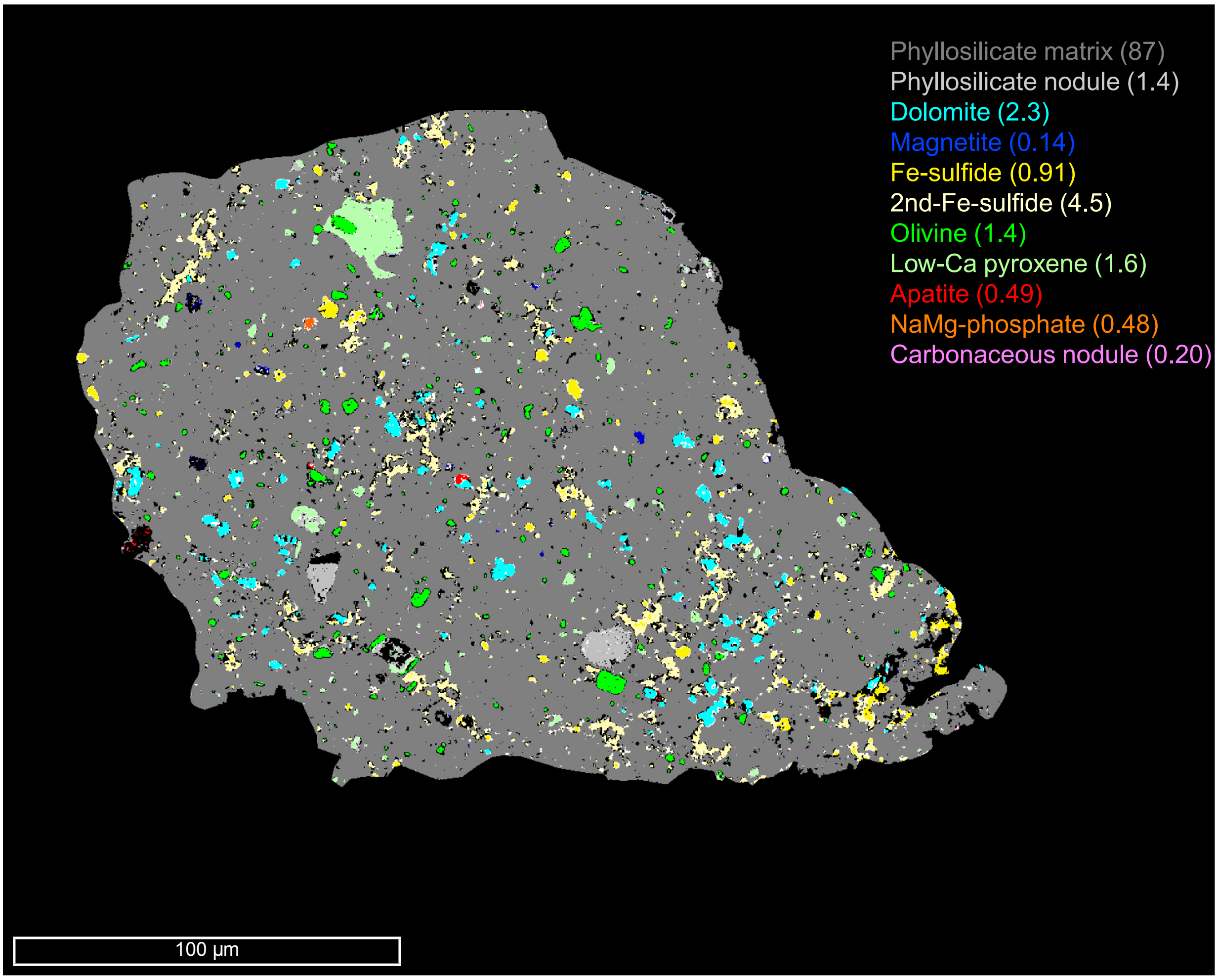

Fig. SB5: Phasemap of A0035-12, which a massive domain in A0035-1 and not accounted for modal abundance estimation of the sample. In parenthesis is modal abundance (%) of phase or component.

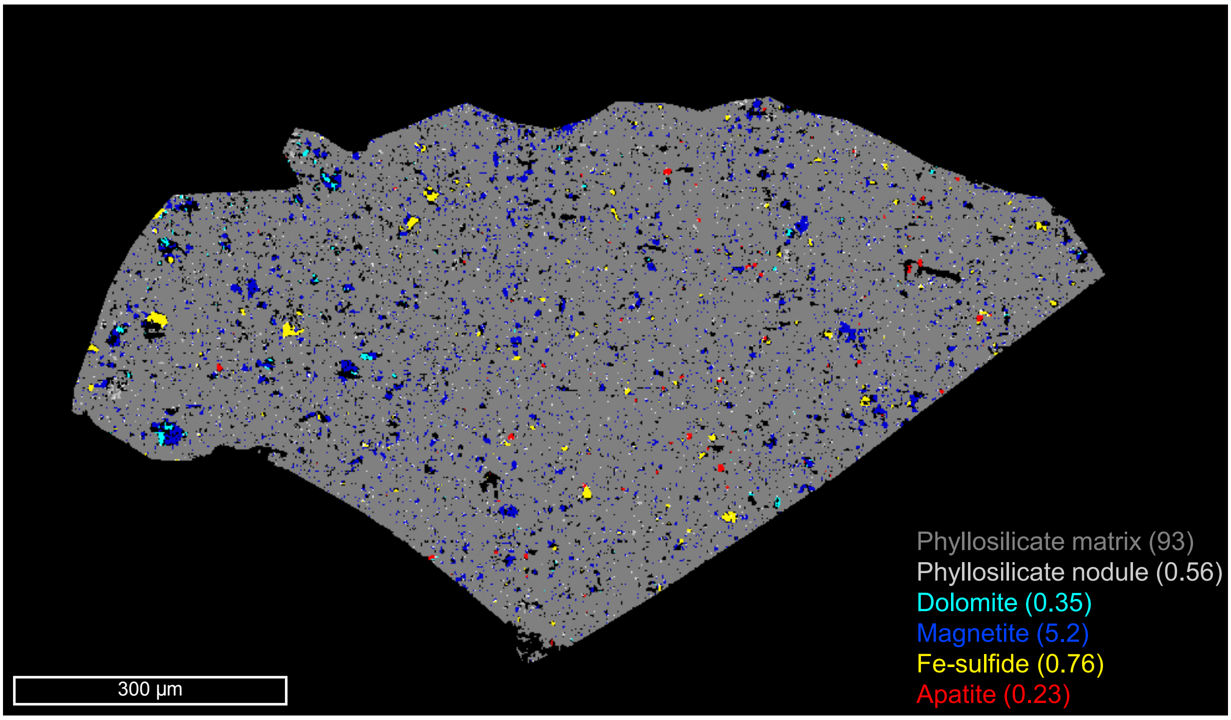

Fig. SB6: Phasemap of A0048-3. In parenthesis is modal abundance (%) of phase or component.

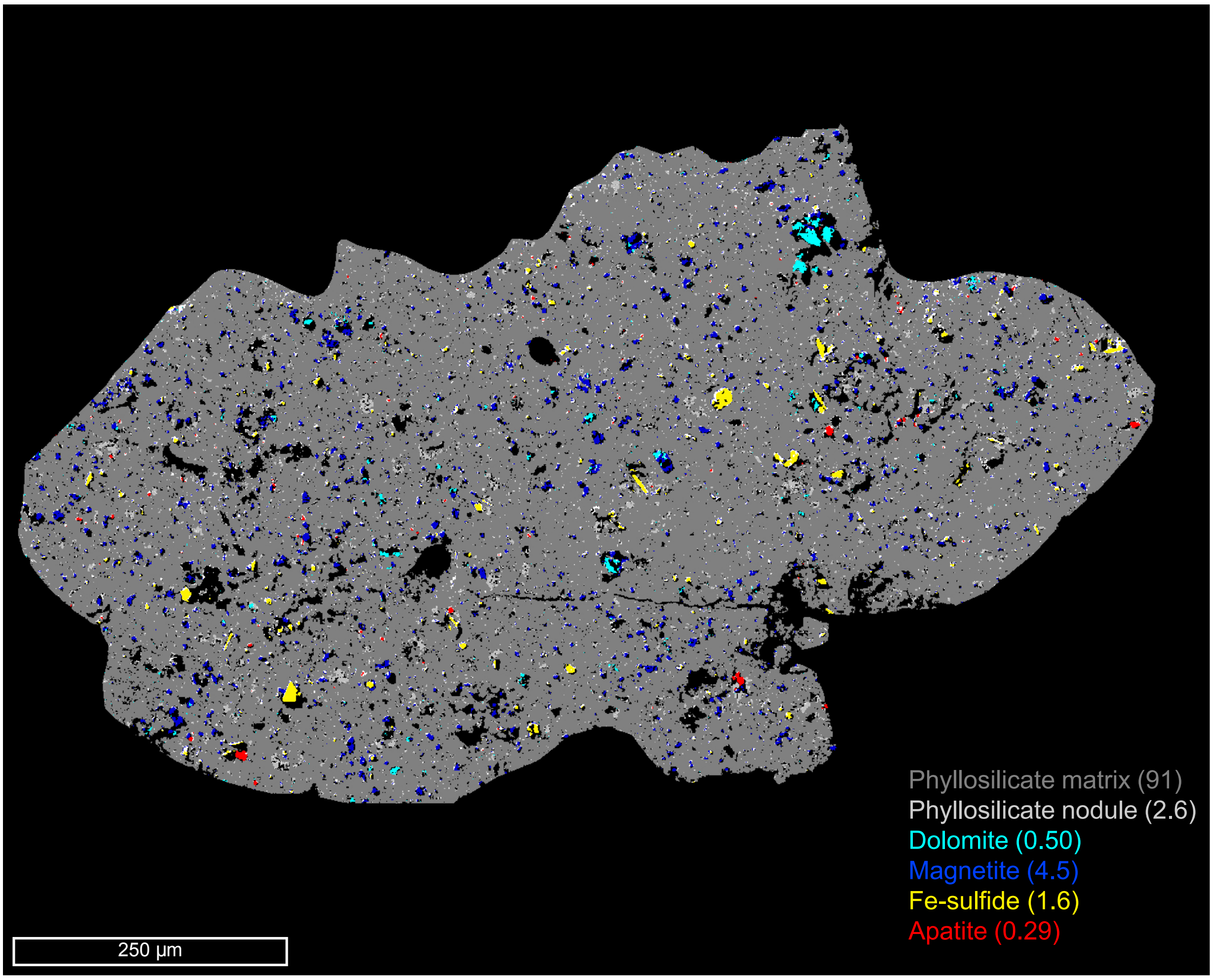

Fig. SB7: Phasemap of A0048-10. In parenthesis is modal abundance (%) of phase or component.

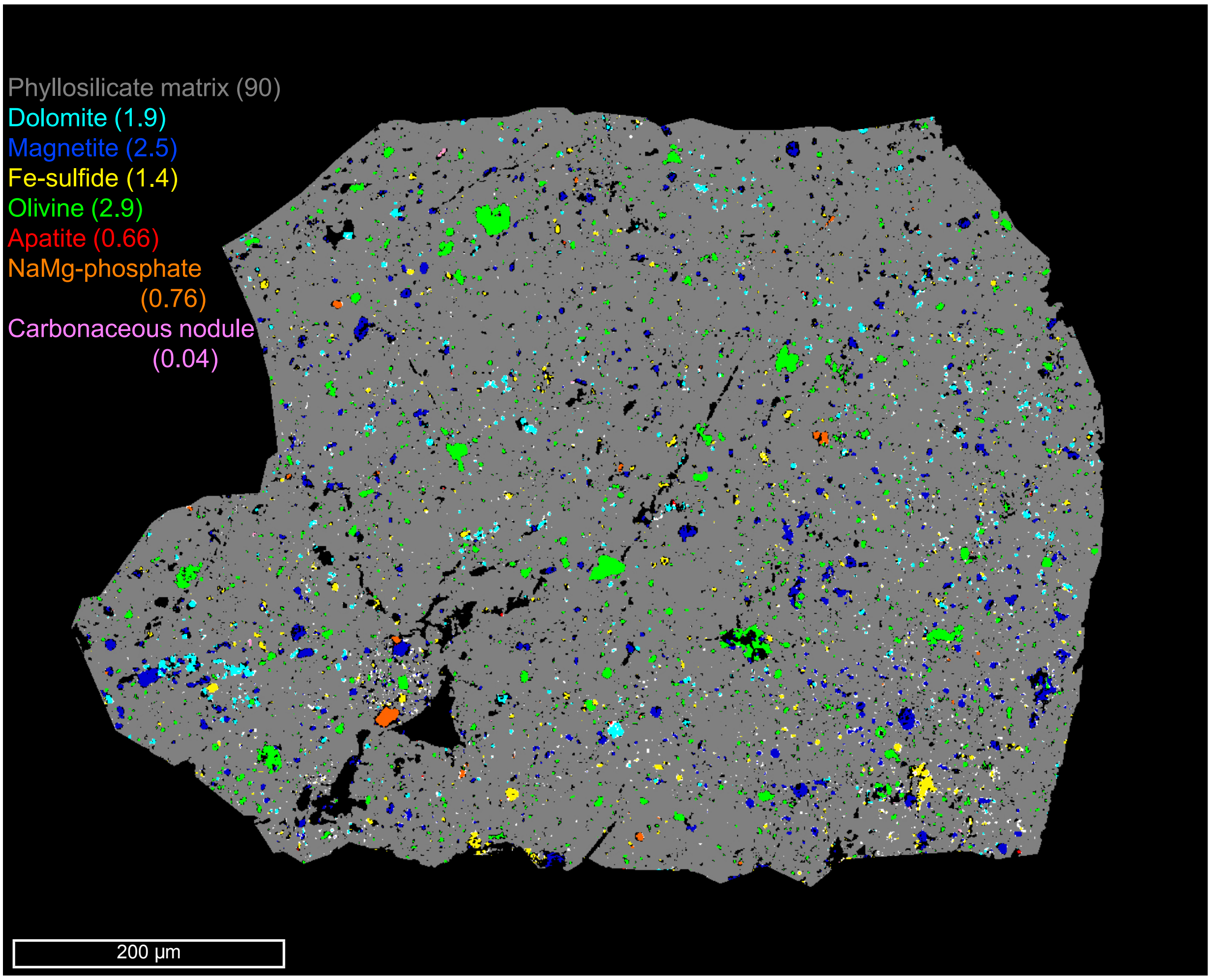

Fig. SB8: Phasemap of A0073-5. In parenthesis is modal abundance (%) of phase or component.

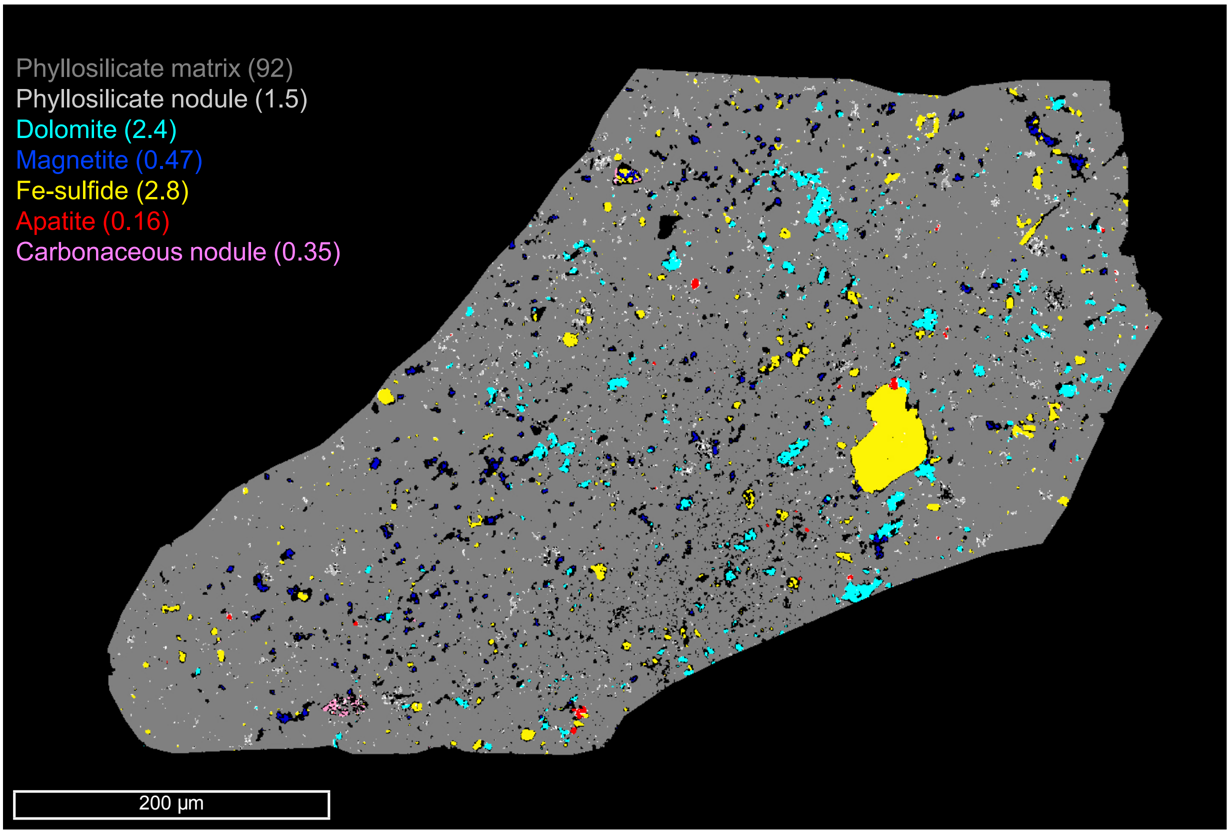

Fig. SB9: Phasemap of A0078-12. In parenthesis is modal abundance (%) of phase or component.

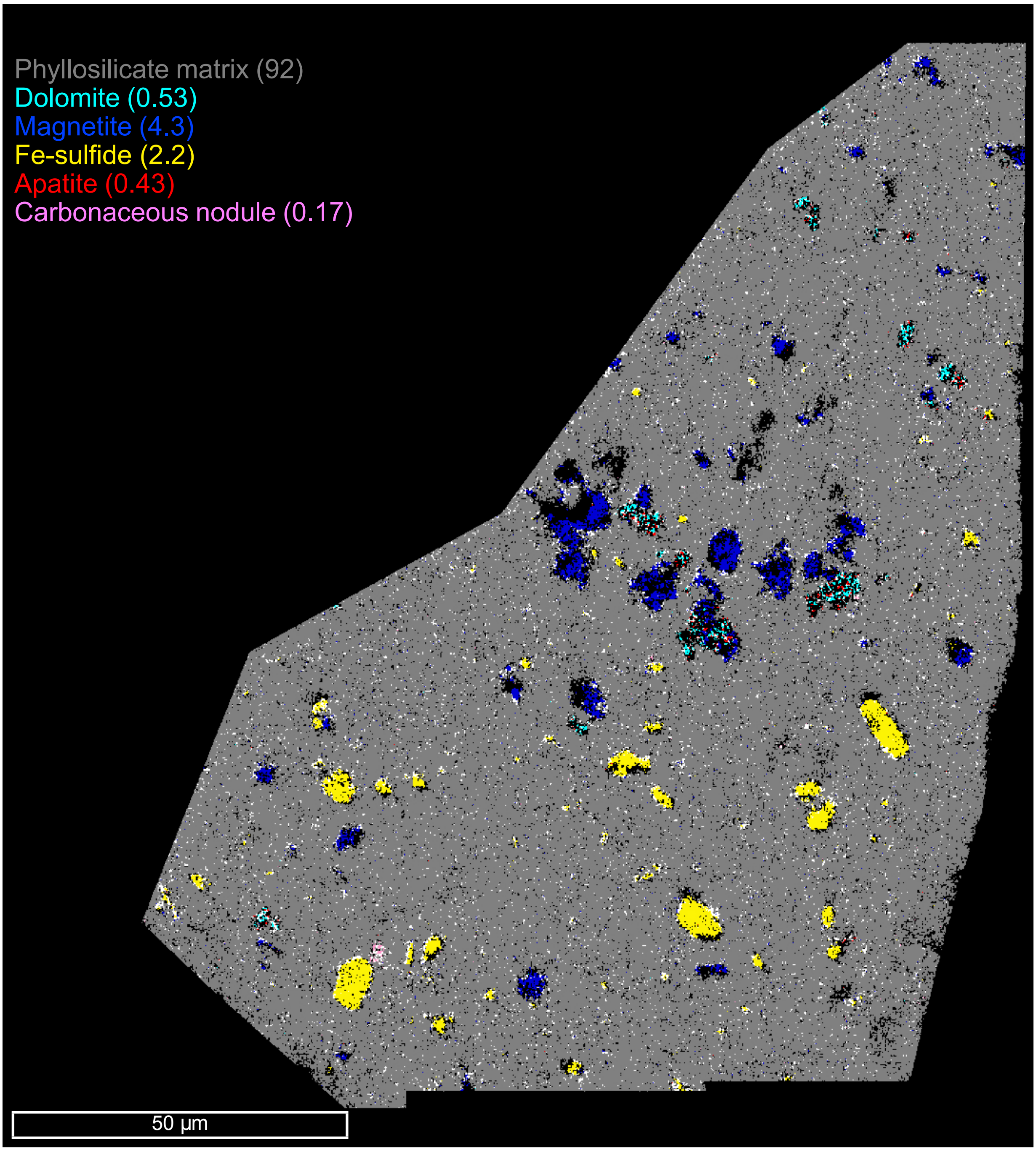

Fig. SB10: Phasemap of A0085-1. In parenthesis is modal abundance (%) of phase or component.

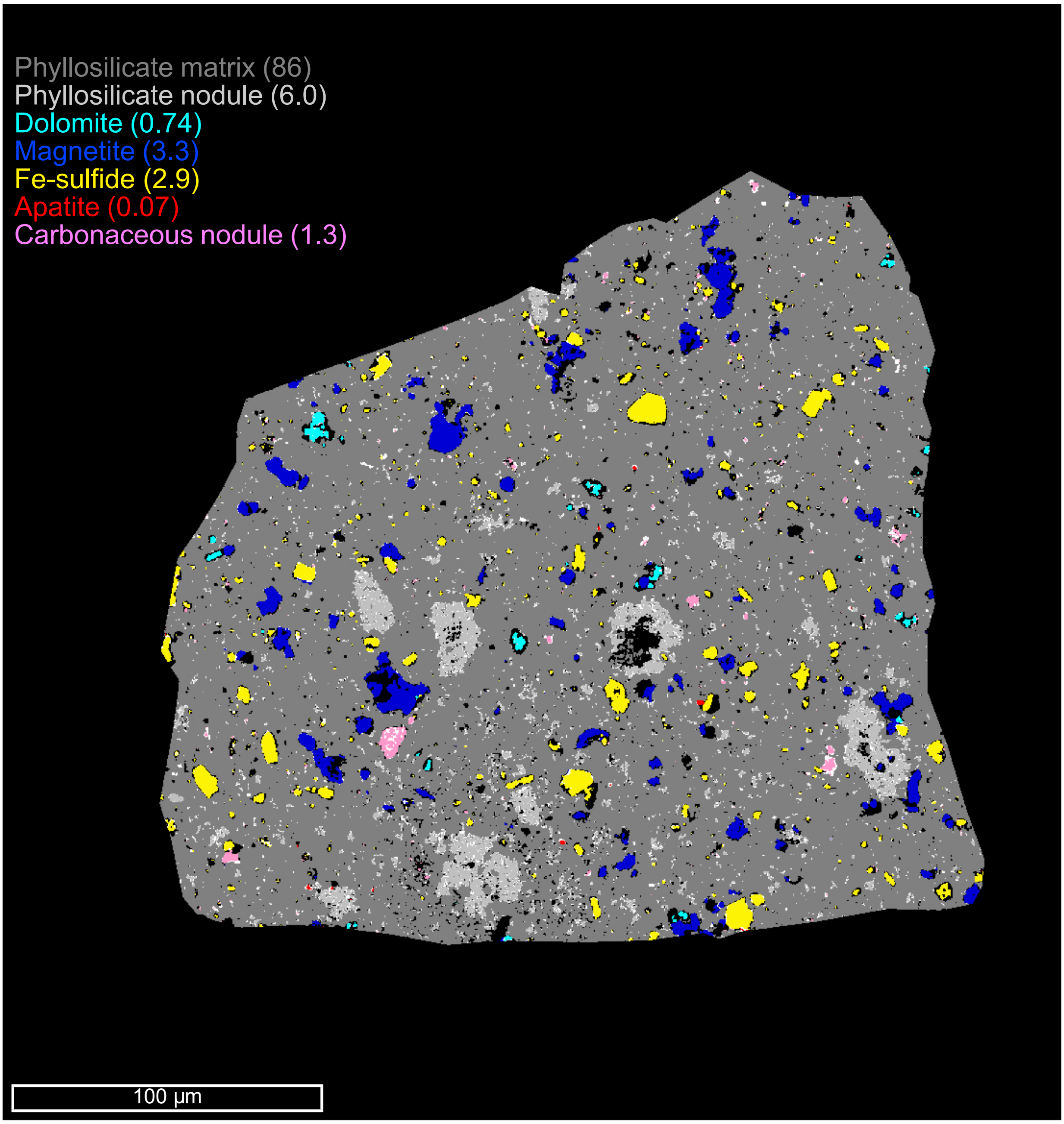

Fig. SB11: Phasemap of A0085-9. In parenthesis is modal abundance (%) of phase or component.

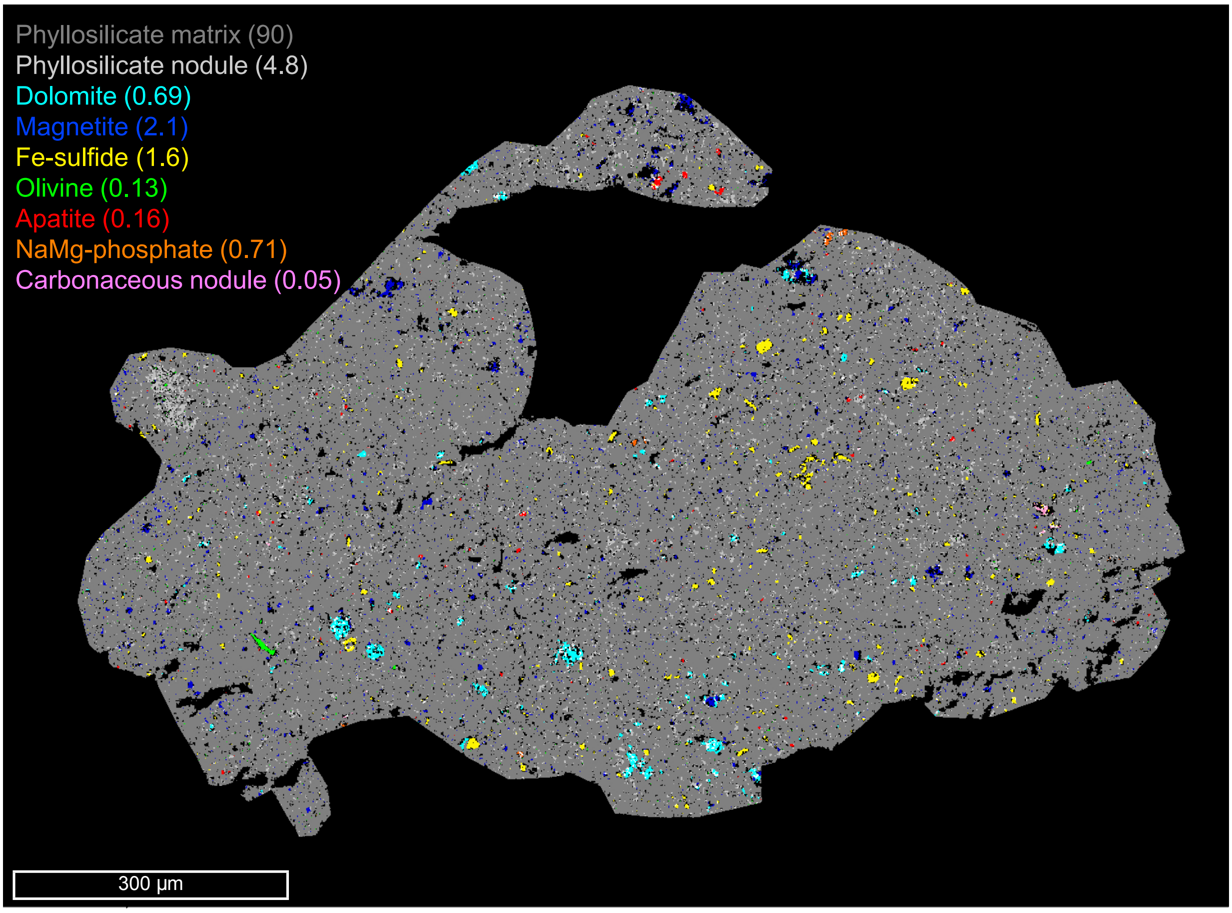

Fig. SB12: Phasemap of C0008-4. In parenthesis is modal abundance (%) of phase or component.

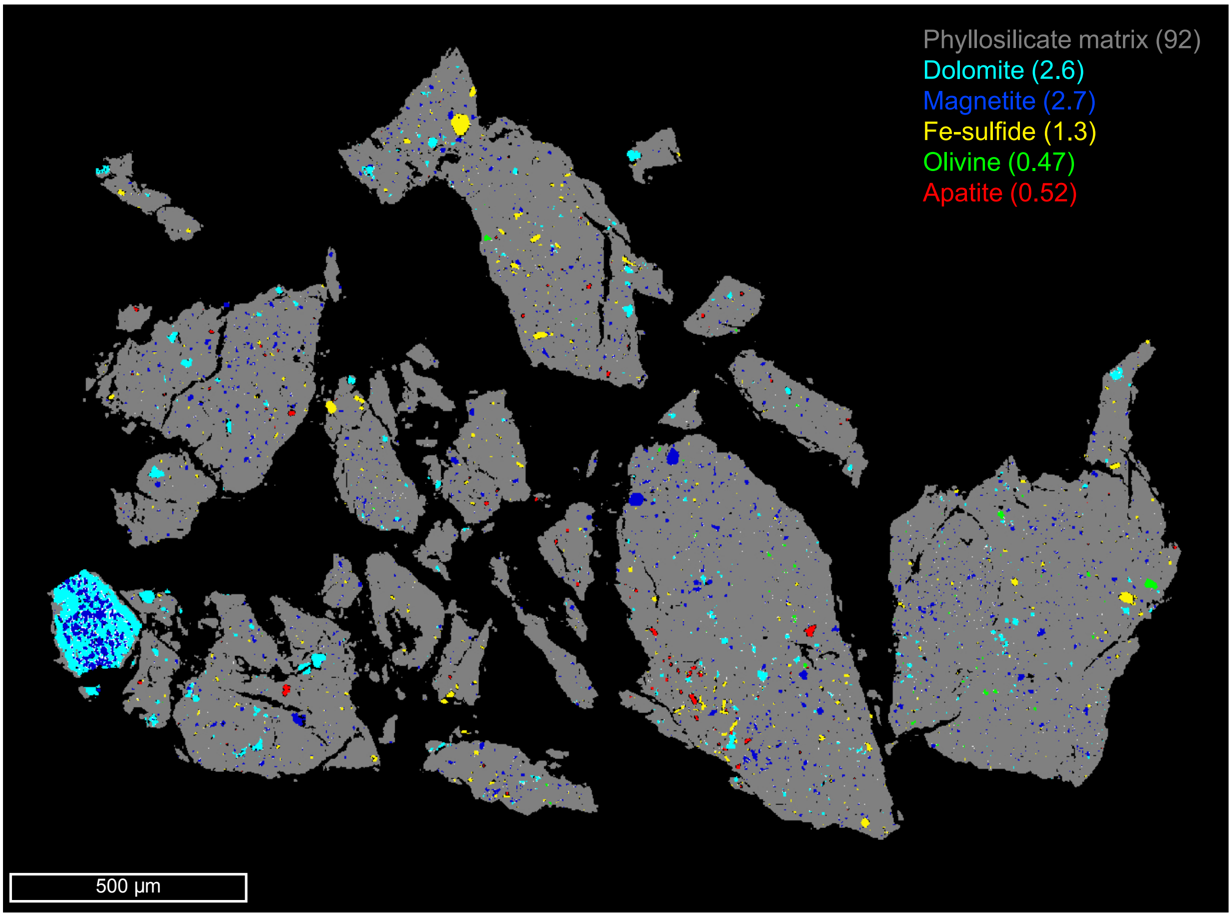

Fig. SB13: Phasemap of C0008-16. In parenthesis is modal abundance (%) of phase or component.

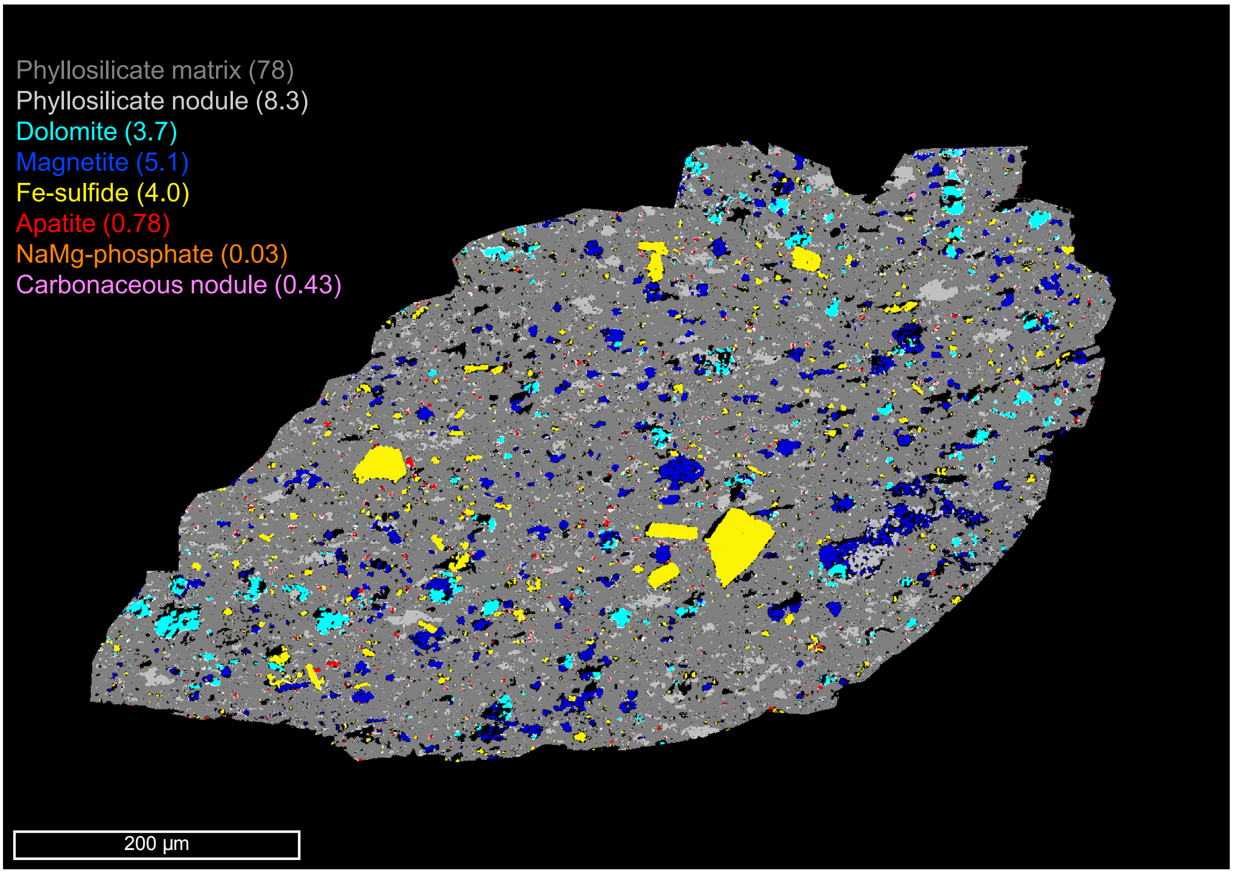

Fig. SB14: Phasemap of C0019-10. In parenthesis is modal abundance (%) of phase or component.

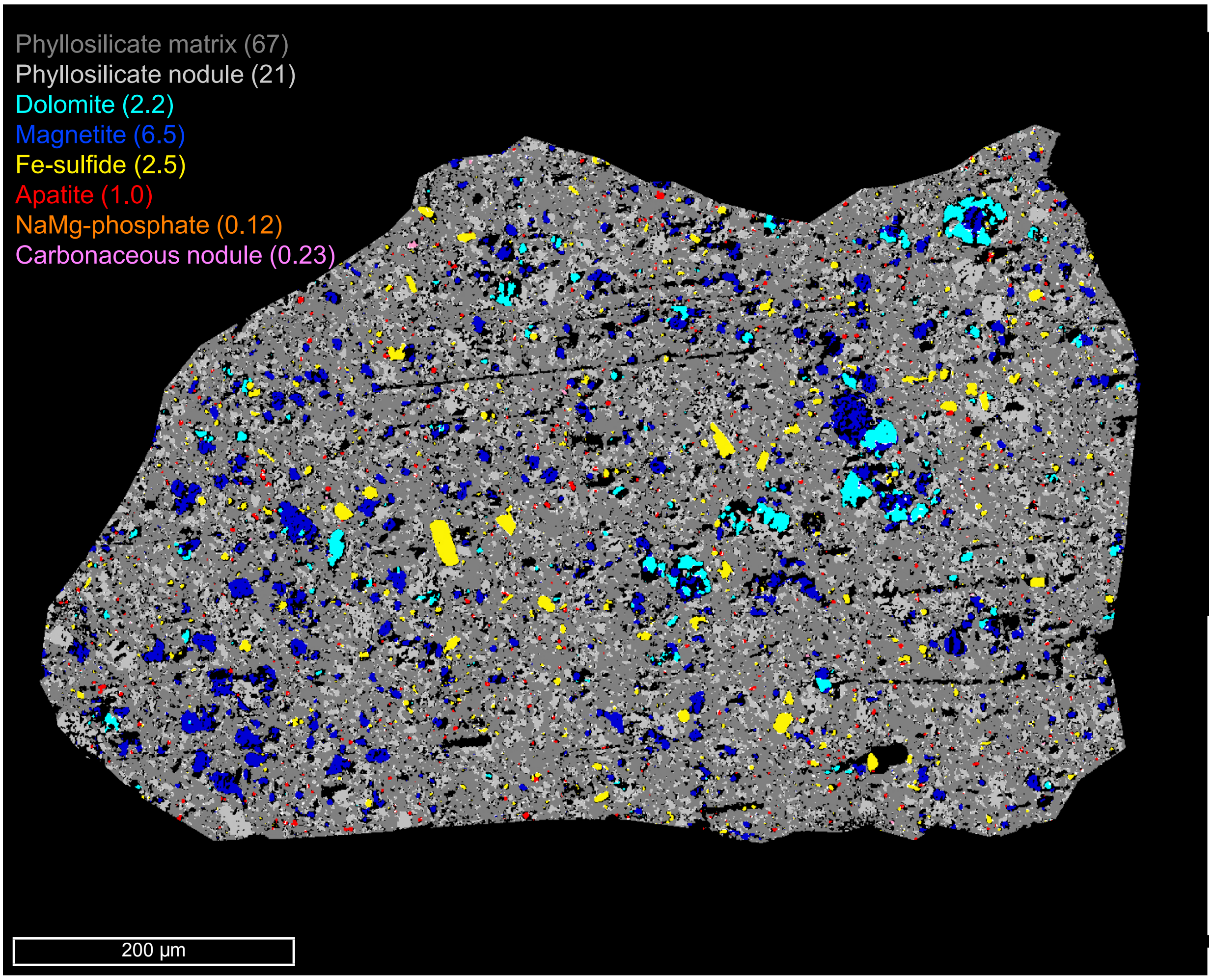

Fig. SB15: Phasemap of C0027-10. In parenthesis is modal abundance (%) of phase or component.

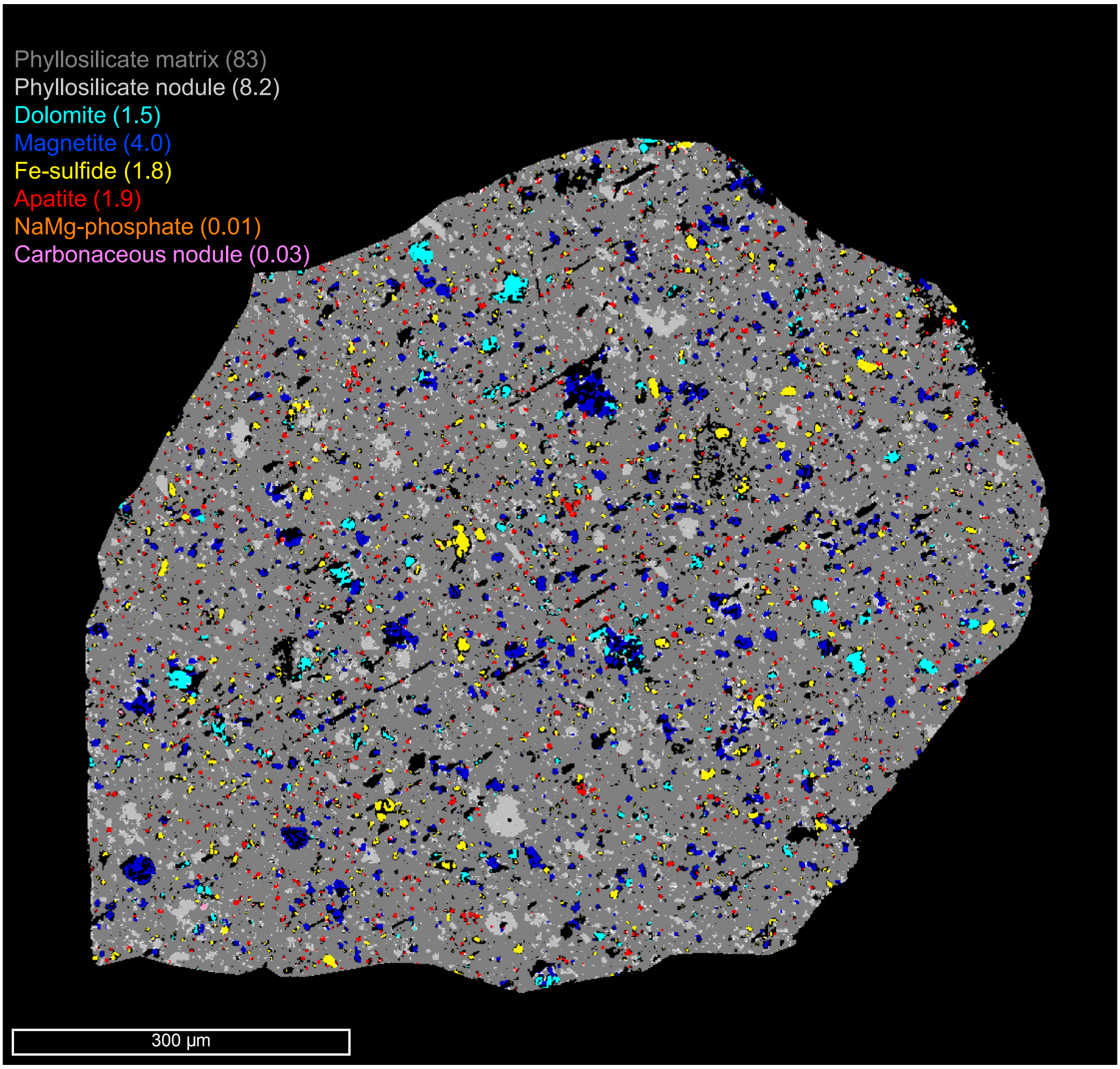

Fig. SB16: Phasemap of C0039-5. In parenthesis is modal abundance (%) of phase or component.

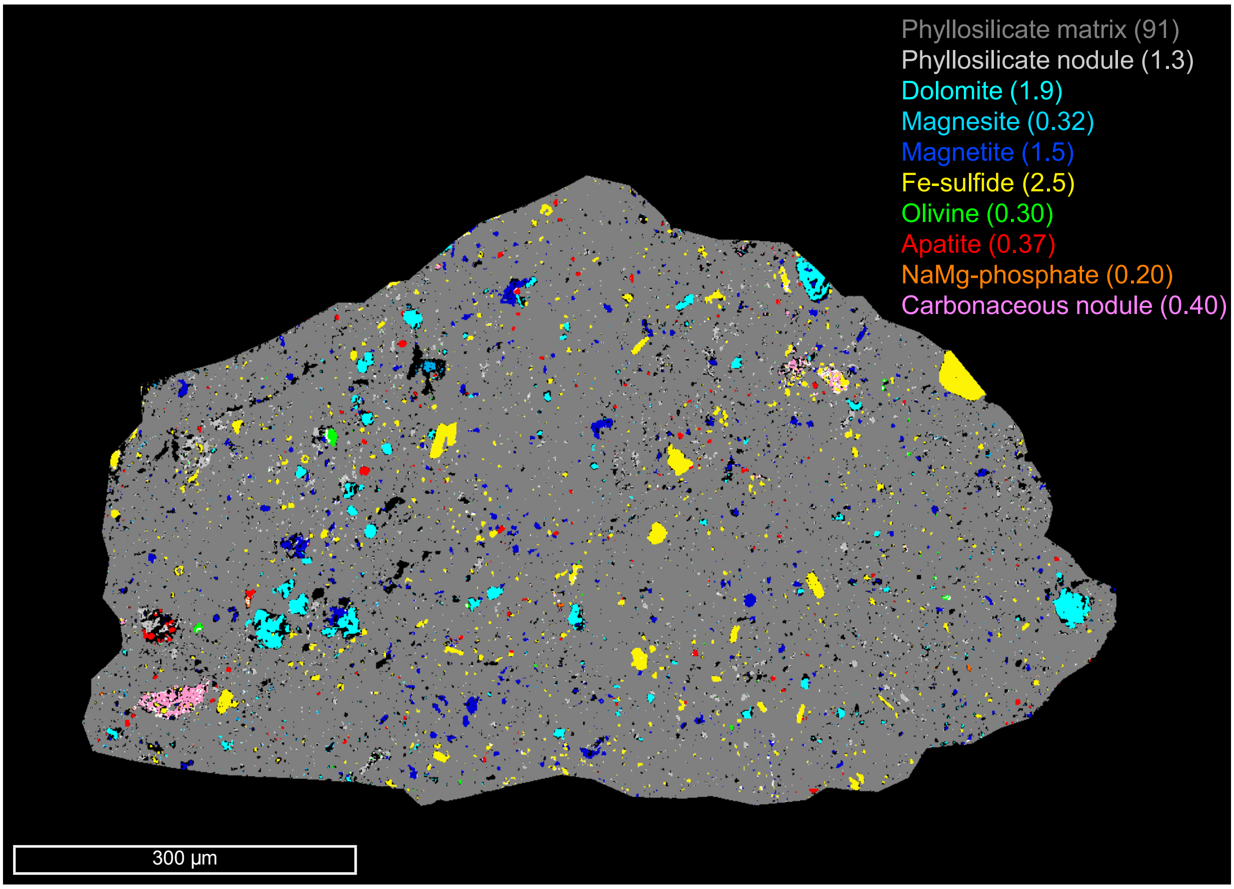

Fig. SB17: Phasemap of C0047-6. In parenthesis is modal abundance (%) of phase or component.

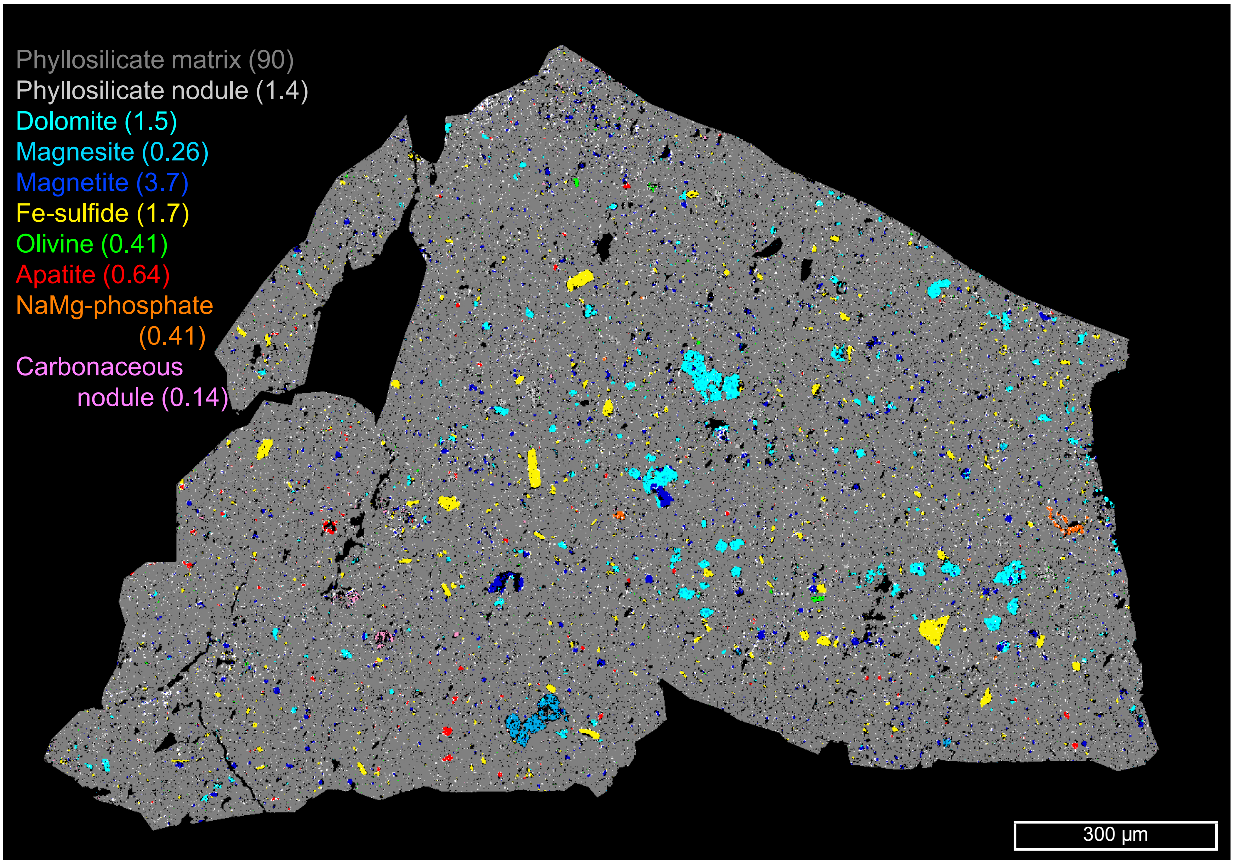

Fig. SB18: Phasemap of C0053-1. In parenthesis is modal abundance (%) of phase or component.

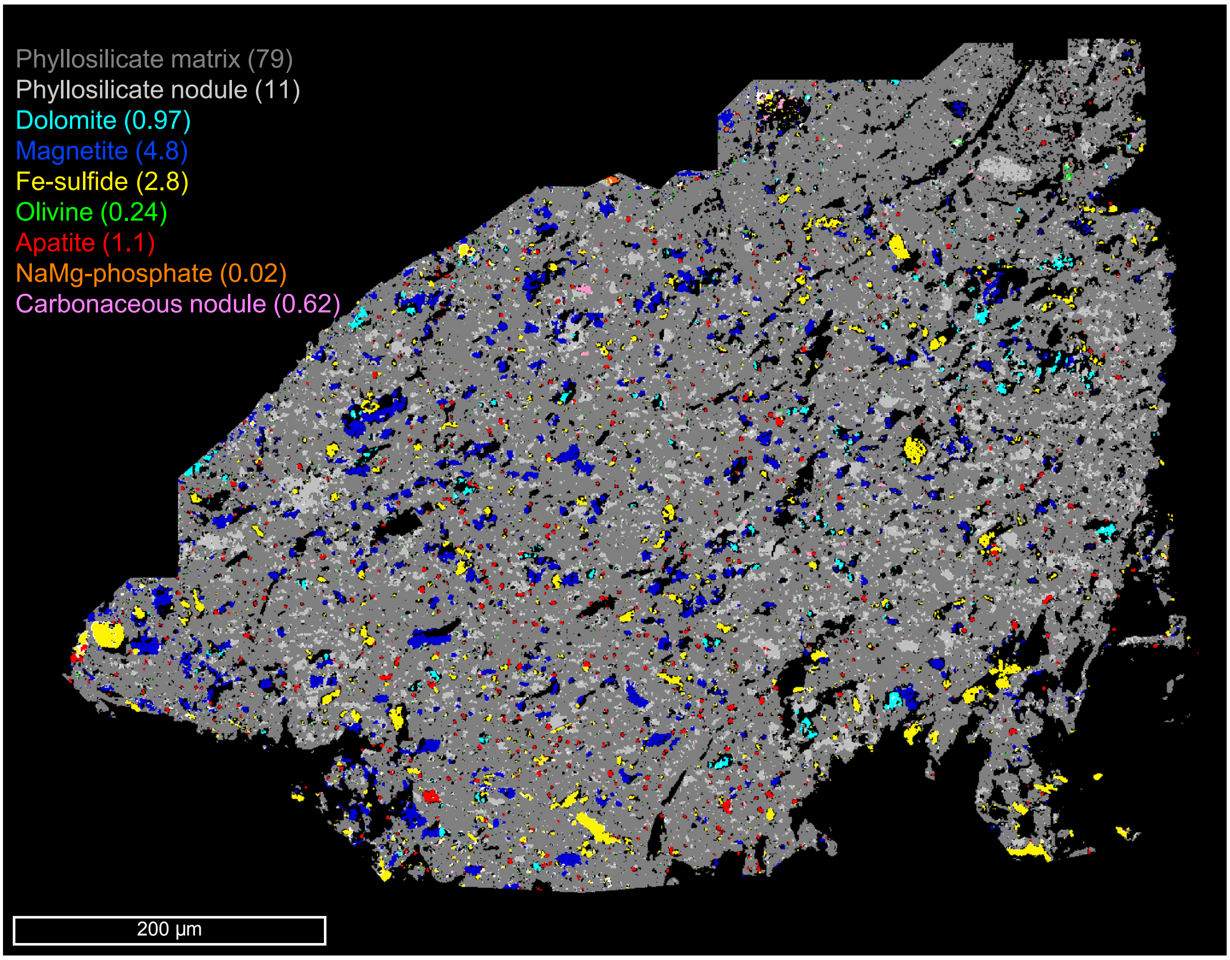

Fig. SB19: Phasemap of C0079-6. In parenthesis is modal abundance (%) of phase or component.

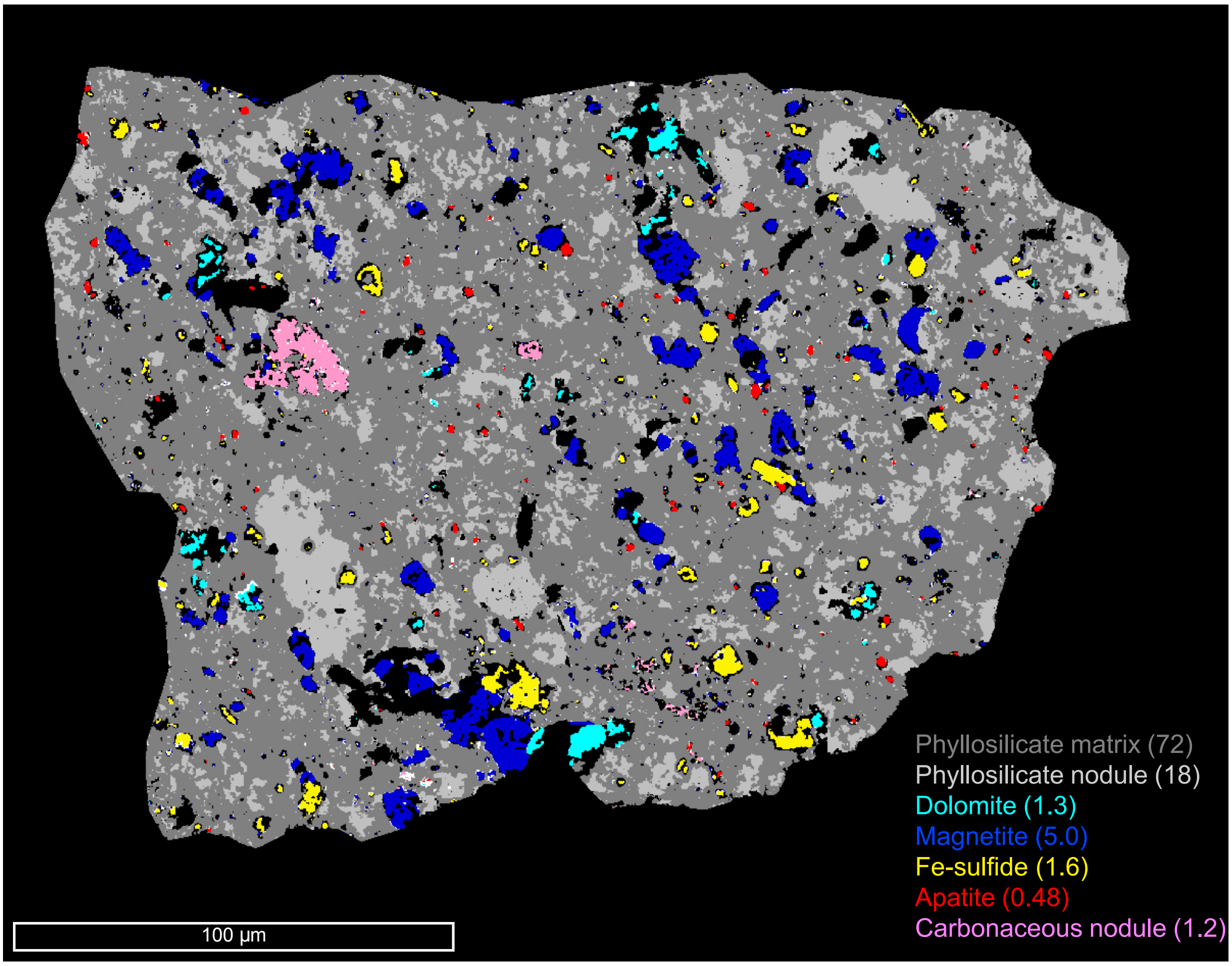

Fig. SB20: Phasemap of C0079-11. In parenthesis is modal abundance (%) of phase or component.

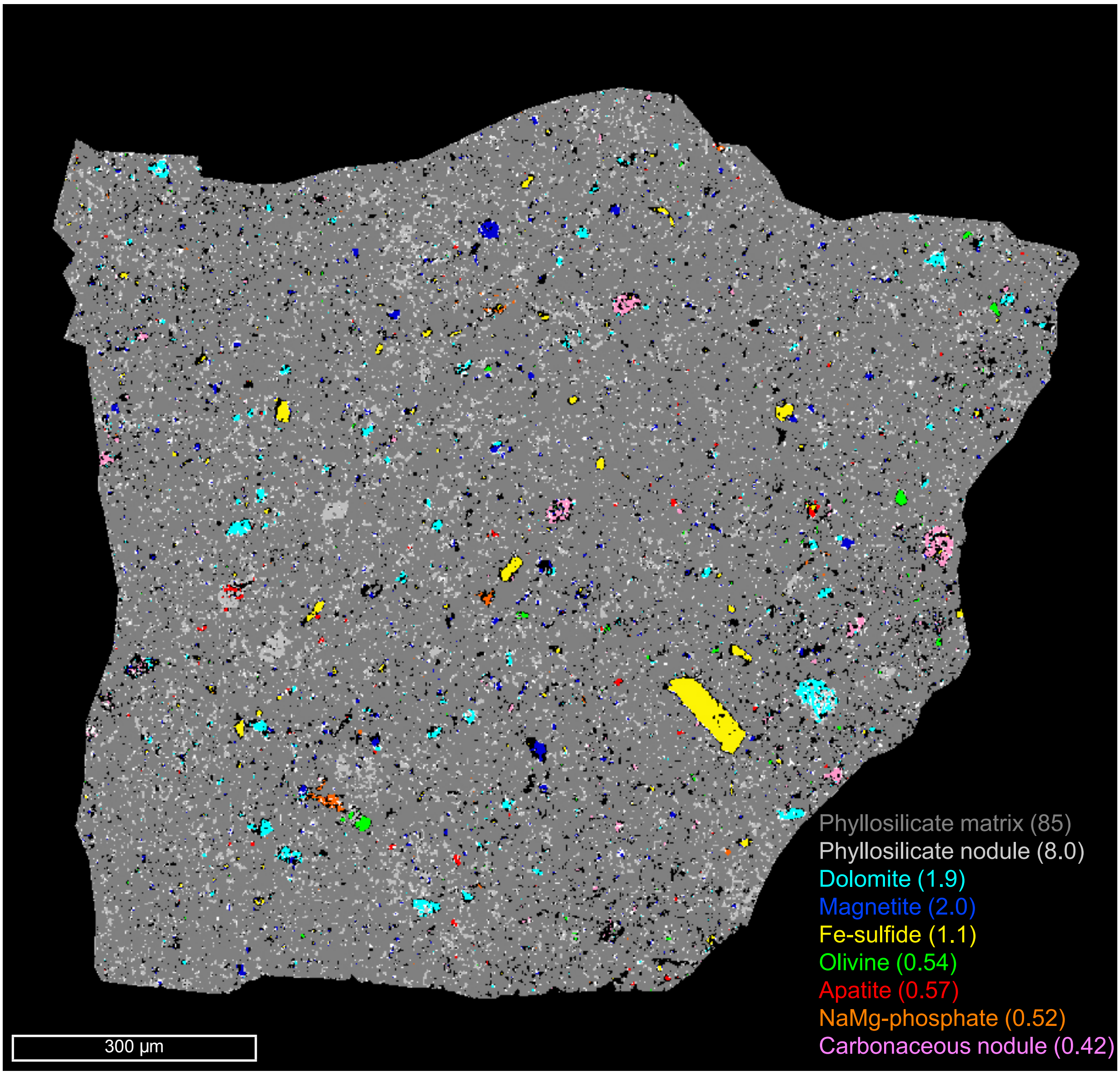

Fig. SB21: Phasemap of C0081-1-s1. In parenthesis is modal abundance (%) of phase or component.

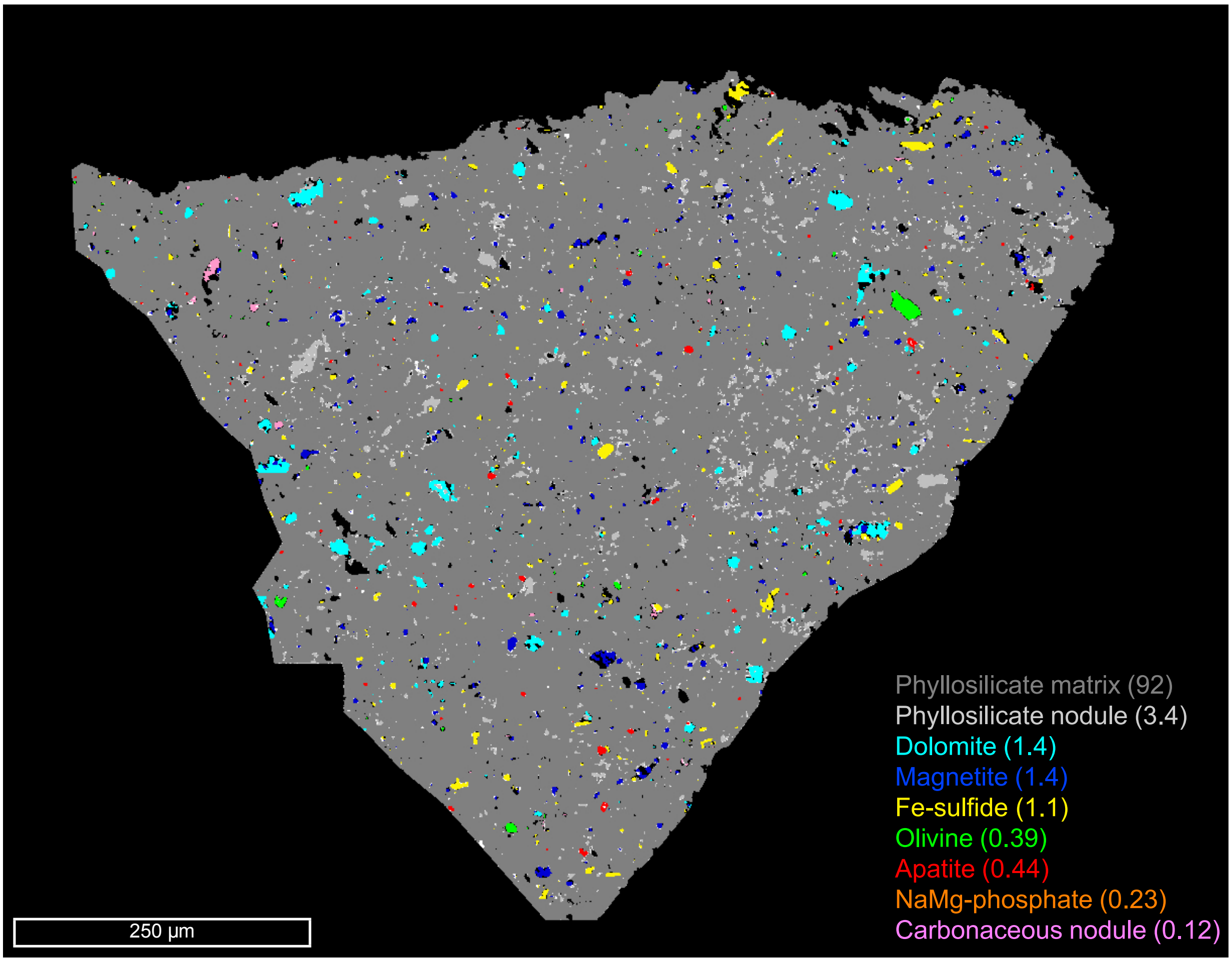

Fig. SB22: Phasemap of C0081-1-s2. In parenthesis is modal abundance (%) of phase or component.

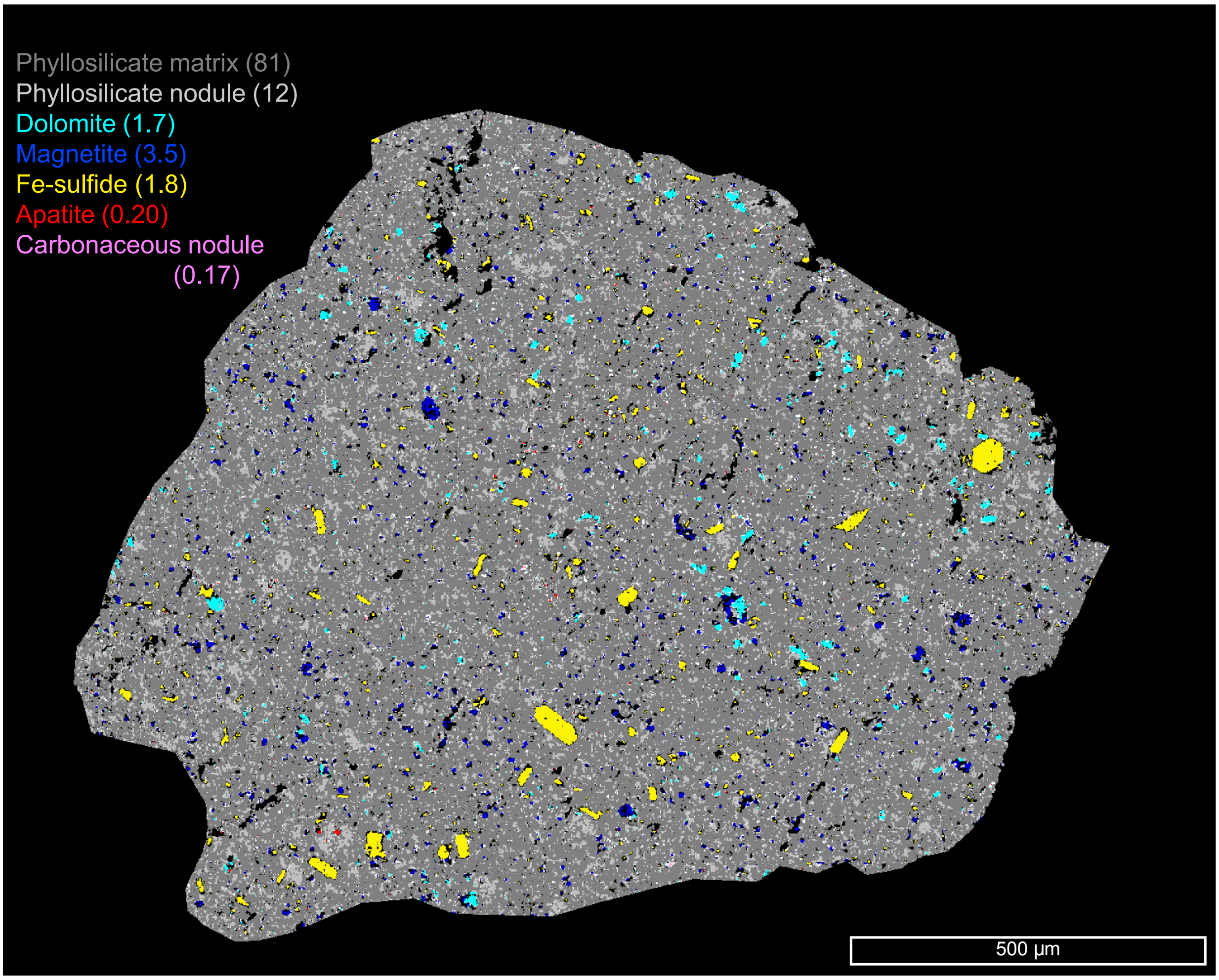

Fig. SB23: Phasemap of C0082-1-s1. In parenthesis is modal abundance (%) of phase or component.

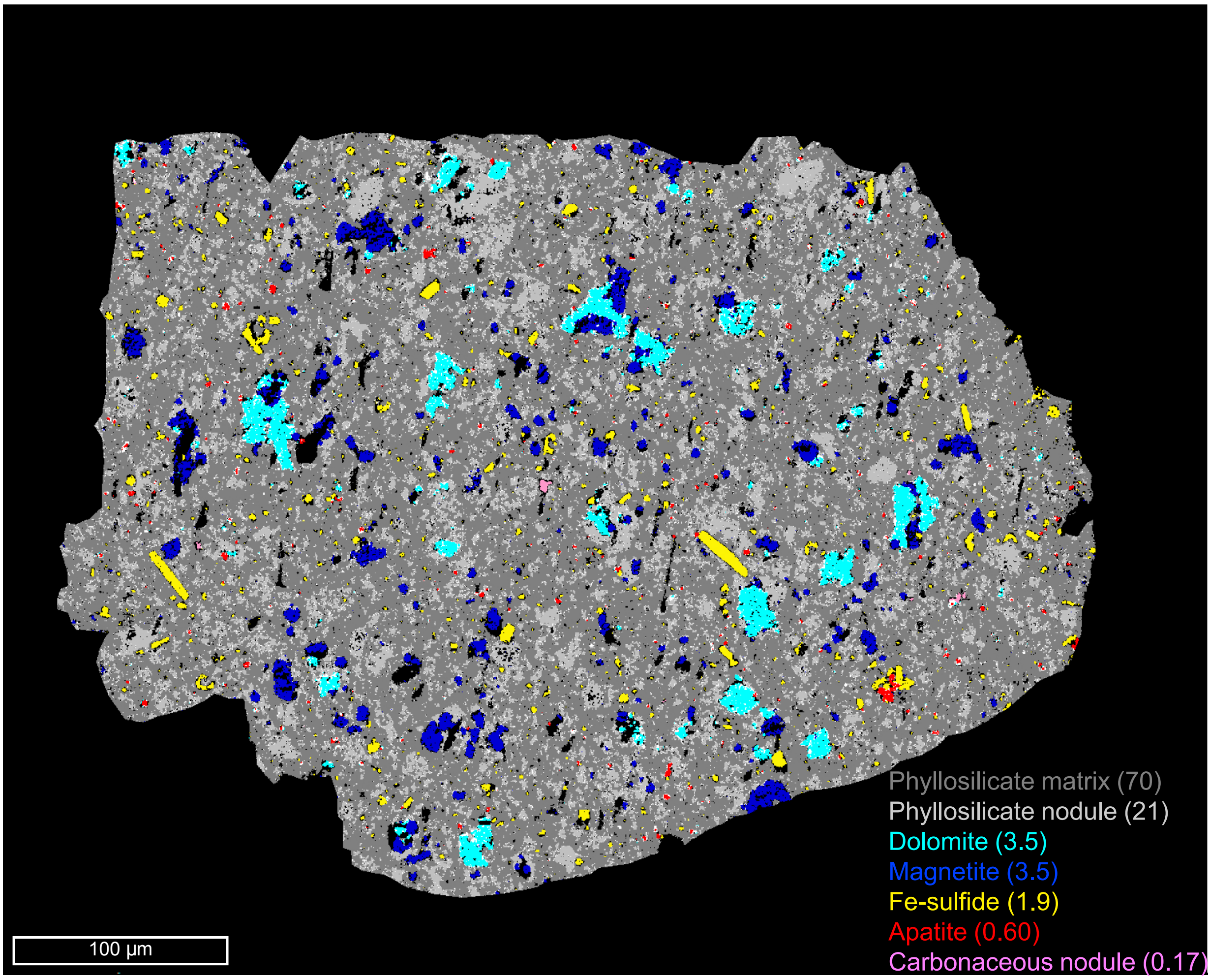

Fig. SB24: Phasemap of C0082-1-s2. In parenthesis is modal abundance (%) of phase or component.

Supplementary Tables

Table S1: Properties of the Ryugu particles examined and the methods applied in this study.

Name	A0022	A0033	A0035	A0048	A0073	A0078	A0085	C0008	C0019	C0027	C0039	C0047	C0053	C0079	C0081	C0082
Size (μm)	2812	2406	2102	3734	1480	2623	1225	3710	2647	2220	1778	1864	2376	3028	3235	2750
Weight (mg)	6.3	4.0	2.7	3.0	0.8	1.8	0.7	10.0	6.8	2.2	1.0	1.3	3.2	2.5	4.4	3.8
Sample preparation																
– Ultra-microtome	○	○	○	○	○	○	○	○	○	○	○	○	○	○	○	○
– Indium mount	○	○	○	○	○	○	○	○	○	○	○	○	○	○	○	○
– Resin mount	○	○	○		○		○	○								
Observation																
– Digital microscope	○	○	○	○	○	○	○	○	○	○	○	○	○	○	○	○
– SEM	○	○	○	○	○	○	○	○	○	○	○	○	○	○	○	○
– TEM		○			○		○									
– XRD	○			○			○				○	○				
Inorganic in situ analysis																
– SEM-EDX (Major element)	○	○	○	○	○	○	○	○	○	○	○	○	○	○	○	○
– EPMA (Major element)		○														
– SIMS (Trace element)		○											○			
– HR-SIMS (O isotope)	○		○		○			○								
– HR-SIMS (C-N isotope)					○	○	○		○				○			
– HR-SIMS (H-Li-B isotope)					○								○			
– HR-SIMS (Mn-Cr isotope)	○	○						○								
Inorganic bulk analysis																
– Session I	○	○	○	○	○	○	○	○	○	○	○	○	○	○	○	○
– Session II	○	○		○		○		○	○	○			○	○	○	○
– Session III	○	○		○		○		○	○	○			○	○	○	○
– Session IV	○	○		○				○	○					○		
– Session V	○	○		○				○	○					○		
– Session VI	○														○	
– Session VII	○	○	○	○		○	○	○	○	○			○	○	○	○
– Session VIII	○	○	○	○	○	○		○	○	○	○	○		○	○	○
– Session IX	○	○	○	○		○		○	○	○				○	○	○
– Session X	○	○				○		○	○					○		
– Session XI	○	○	○	○	○	○	○	○	○	○	○	○	○	○	○	○
Organic in situ analysis																
– Raman	○	○	○	○	○	○	○	○	○	○	○	○	○	○	○	○
– DESI				○				○								
Organic bulk analysis																
– FTIR			○					○								
– UHPLC								○								

Details of each analytical method are described in the Supplementary text.

Table S2: Modal abundances of components and grain density.

	Modal abundance (volume %)								Grain density (kg·m^{-3})
	Phyllosilicate						Olivine (+ LPx)	Carbonaceous nodule	
Sample	matrix	nodule	Carbonate	Magnetite	Fe-sulfide	Phosphate			
A0022 (n=2)	83.7		6.93	5.39	3.50	0.52			2.68k
A0033 (n=1)	85.7	2.10	6.83	2.87	2.02	0.47			2.58k
A0035 (n=1)	86.2		2.60	4.14	5.24	1.05	0.57	0.21	2.67k
A0048 (n=2)	91.8	1.57	0.43	4.81	1.18	0.26			2.58k
A0073 (n=1)	89.8		1.86	2.50	1.44	1.42	2.94	0.04	2.56k
A0078 (n=1)	92.2	1.52	2.44	0.47	2.83	0.16		0.35	2.50k
A0085 (n=2)	89.1	2.97	0.63	3.81	2.53	0.25	0.00	0.72	2.58k
C0008 (n=2)	91.1	2.38	1.65	2.37	1.44	0.70	0.30	0.03	2.53k
C0019 (n=1)	77.7	8.30	3.72	5.07	3.96	0.81	0.00	0.43	2.66k
C0027 (n=1)	66.6	20.9	2.19	6.47	2.50	1.13		0.23	2.67k
C0039 (n=1)	82.5	8.24	1.50	3.96	1.83	1.88		0.03	2.59k
C0047 (n=1)	91.2	1.31	2.20	1.53	2.46	0.57	0.30	0.40	2.53k
C0053 (n=1)	89.8	1.38	1.78	3.74	1.70	1.05	0.41	0.14	2.58k
C0079 (n=2)	75.5	14.5	1.13	4.91	2.20	0.80	0.12	0.92	2.60k
C0081 (n=2)	88.3	5.68	1.62	1.67	1.11	0.88	0.46	0.27	2.51k
C0082 (n=2)	75.1	16.4	2.63	3.50	1.84	0.40		0.17	2.57k
Average	84.8	6.7	2.5	3.6	2.4	0.8	0.6	0.3	2.59k
1σ	7.5	6.6	1.9	1.6	1.1	0.5	0.9	0.3	0.06k

"n" in parentheses indicates the number of the mounts examined, and "k" attached to values denotes $\times 10^3$.

"Carbonate" includes dolomite, calcite and magnesites, and "Phosphate" does apatite and Na-Mg-phosphate.

Grain density is estimated assuming densities of the phase as follows; phyllosilicate (2.42k), carbonate (2.84k), magnetite (5.15k), Fe-sulfide (pyrrhotite) (4.61k), phosphate (3.08k), olivine (3.27k), and carbonaceous nodule (1.10k).

Table S3: Densities and modal abundances of the components.

	Density ($kg\cdot m^{-3}$)		Modal abundance (volume %)		
Sample	Grain density	Bulk density	*Void	Coarse component	Matrix
A0022 (n=2)	2.68k	1.31k	51.0	8.0	40.9
A0033 (n=1)	2.58k	2.08k	19.2	11.5	69.2
A0035 (n=2)	2.67k	1.65k	38.1	8.5	53.3
A0048 (n=1)	2.58k	1.31k	49.4	4.2	46.4
A0073 (n=1)	2.56k	1.51k	41.2	6.0	52.7
A0078 (n=2)	2.50k	1.59k	36.6	4.9	58.4
A0085 (n=1)	2.58k	1.47k	42.9	6.2	50.8
C0008 (n=2)	2.53k	1.42k	44.0	5.0	51.0
C0019 (n=1)	2.66k	1.93k	27.4	16.2	56.4
C0027 (n=1)	2.67k	1.40k	47.5	17.5	34.9
C0039 (n=1)	2.59k	1.44k	44.6	9.7	45.7
C0047 (n=1)	2.53k	1.44k	43.0	5.0	52.0
C0053 (n=1)	2.58k	1.86k	28.0	7.4	64.6
C0079 (n=1)	2.60k	1.20k	53.8	11.3	34.9
C0081 (n=1)	2.51k	1.40k	44.2	6.5	49.2
C0082 (n=1)	2.57k	1.44k	44.1	13.9	41.9
Average	2.59k	1.53k	40.9	8.9	50.2
1σ	0.06k	0.24k	9.3	4.2	9.5

"n" in parentheses indicates the number of the mounts examined, and "k" attached to values denotes $\times 10^3$. *Void is estimated as porosity based on the grain density and the bulk density.

Table S4: Elemental abundances of components in C0053-1.

	Apatite (n=1)	Dolomite-H (n=2)	Dolomite (n=3)	Magnesite (n=2)	Phyllosilicate matrix (n=3)	Phyllosilicate nodule (n=5)	Pyrrhotite (n=2)
[Li]	3.2 (0.6)u	470 (90)n	700 (400)n	700 (100)n	3.0 (0.7)u	3.0 (0.2)u	500 (100)n
[Sr]	770 (20)u	144 (2)u	150 (10)u	13 (1)u	26 (4)u	14 (5)u	—
[Y]	161 (4)u	2.2 (0.6)u	1000 (300)n	210 (40)n	2.2 (0.3)u	700 (100)n	—
[Zr]	8 (1)u	900 (300)n	1.4 (0.7)u	1.3 (0.3)u	13 (4)u	8.1 (1)u	—
[Nb]	700 (100)n	31 (3)n	80 (30)n	100 (60)n	600 (300)n	500 (300)n	1 (1)u
[Ba]	151 (5)u	20 (5)u	16 (1)u	20 (3)u	7 (4)u	7 (4)u	—
[La]	12.1 (0.7)u	710 (70)n	90 (30)n	18.8 (0.6)n	200 (100)n	40 (20)n	20 (10)n
[Ce]	28 (2)u	1.5 (0.2)u	190 (80)n	26 (4)n	500 (100)n	70 (10)n	50 (30)n
[Pr]	4.4 (0.3)u	210 (30)n	30 (30)n	6 (2)n	80 (10)n	20 (10)n	7 (3)n
[Nd]	24 (1)u	996.6 (0.4)n	200 (100)n	70 (50)n	500 (100)n	160 (80)n	—
[Sm]	9.5 (0.7)u	250 (70)n	119 (3)n	33 (2)n	250 (40)n	50 (10)n	—
[Eu]	3.9 (0.3)u	81 (3)n	40 (10)n	20 (10)n	80 (20)n	30 (20)n	20 (8)n
[Gd]	20 (2)u	300 (200)n	110 (10)n	28 (2)n	190 (50)n	40 (30)n	—
[Dy]	27 (2)u	270 (40)n	135 (4)n	40 (10)n	290 (40)n	60 (30)n	—
[Er]	18 (1)u	240 (90)n	130 (70)n	—	150 (70)n	40 (40)n	55 (4)n
[Yb]	24 (1)u	400 (100)n	180 (40)n	29.9n	180 (80)n	50 (30)n	74 (6)n
[Lu]	3.9 (0.2)u	40 (10)n	30 (30)n	7 (3)n	30 (20)n	9 (7)n	11 (5)n
[SiO$_2$]	—	—	—	—	40.5c	40.5c	—
[CaO]	55.1c	30.4c	30.4c	—	—	—	—
[Fe]	—	—	—	—	—	—	62.3c
[MgO]	—	—	—	29.3c	—	—	—

“n” in parentheses indicates the number of the spots analyzed. Units are in g/g, and “c”, “u”, and “n” attached to values denote $\times 10^{-2}$, $\times 10^{-6}$, and $\times 10^{-9}$, respectively. “Dolomite-H” denotes the dolomite that is distinctively higher in elemental abundance compared to the others.

Table S5: Elemental abundances of components in A0033-15.

	Apatite (n=2)	Dolomite-H (n=1)	Dolomite (n=2)	Phyllosilicate matrix (n=2)	Phyllosilicate nodule (n=2)
[Li]	2.2 (0.7)u	500 (200)n	137 (6)n	2.8 (0.6)u	2.5 (0.3)u
[Sr]	760 (40)u	170 (20)u	143 (9)u	17 (5)u	7 (2)u
[Y]	180 (50)u	1.5 (0.8)u	260 (60)n	4.1 (0.7)u	800 (100)n
[Zr]	10 (8)u	1 (0.5)u	310 (50)n	10 (3)u	8 (1)u
[Nb]	3.7 (0.6)u	60 (40)n	200 (90)n	500 (100)n	290 (20)n
[Ba]	160 (40)u	30 (10)u	17.7 (0.9)u	4 (2)u	1.08 (0.08)u
[La]	13 (1)u	181 (4)n	32 (8)n	300 (100)n	19 (5)n
[Ce]	30 (3)u	320 (40)n	80 (20)n	1 (0.4)u	50 (0)n
[Pr]	5 (0.9)u	36 (6)n	17 (7)n	200 (80)n	20 (10)n
[Nd]	33 (3)u	500 (200)n	90 (30)n	960 (90)n	103 (7)n
[Sm]	15 (3)u	120 (60)n	50 (20)n	270 (60)n	40 (40)n
[Eu]	6.6 (0.4)u	—	5 (30)n	180 (50)n	14.9 (0.1)n
[Gd]	26.9 (0.6)u	326n	20 (30)n	400 (100)n	80 (90)n
[Dy]	29 (6)u	190 (90)n	40 (40)n	400 (200)n	80 (3)n
[Er]	14 (3)u	130 (50)n	30 (20)n	300 (100)n	60 (10)n
[Yb]	11.2 (0.3)u	260 (90)n	60 (20)n	370 (10)n	110 (80)n
[Lu]	1.2 (0.6)u	33 (7)n	8 (3)n	80 (20)n	20 (30)n
[SiO$_2$]	—	—	—	40.5c	40.5c
[CaO]	55.1c	30.4c	30.4c	—	—

“n” in parentheses indicates the number of the spots analyzed. Units are in g/g, and “c”, “u”, and “n” attached to values denote $\times 10^{-2}$, $\times 10^{-6}$, and $\times 10^{-9}$, respectively. “Dolomite-H” denotes the dolomite that is distinctively higher in elemental abundance compared to the others.

Table S6: O isotopic compositions of magnetite, dolomite, olivine, and low-Ca pyroxene grains.

Sample	Phase	Spot	δ^{18}O	(1SE)	δ^{17}O	(1SE)	Δ^{17}O	(1SE)
A0022-15	magnetite	oxy-mag-a22-15s1@6699	3.6	0.6	4.7	0.5	2.8	0.4
A0022-15	magnetite	oxy-mag-a22-15s1@6702	4.9	0.6	4.9	0.5	2.4	0.4
A0022-15	magnetite	oxy-mag-a22-15s1@6703	7.4	0.6	6.7	0.5	2.9	0.4
A0022-15	magnetite	oxy-mag-a22-15s1@6707	5.6	0.6	6.1	0.4	3.2	0.4
A0022-15	magnetite	oxy-mag-a22-15s1@6715	4.5	0.7	4.5	0.5	2.2	0.4
A0022-15	magnetite	oxy-mag-a22-15s1@6725	6.1	0.6	5.8	0.5	2.6	0.4
A0022-15	magnetite	oxy-mag-a22-15s1@6728	4.2	0.6	3.6	0.5	1.4	0.5
A0022-15	magnetite	oxy-mag-a22-15s1@6741	3.0	0.5	3.5	0.5	2.0	0.4
A0022-15	dolomite	oxy-dol-a22-15s1@6697	37.1	0.5	20.9	0.4	1.6	0.4
A0022-15	dolomite	oxy-dol-a22-15s1@6698	39.7	0.4	21.8	0.4	1.2	0.4
A0022-15	dolomite	oxy-dol-a22-15s1@6700	33.1	0.4	18.6	0.4	1.4	0.3
A0022-15	dolomite	oxy-dol-a22-15s1@6701	39.0	0.4	22.0	0.4	1.8	0.4
A0022-15	dolomite	oxy-dol-a22-15s1@6706	34.9	0.7	19.1	0.5	1.0	0.6
A0022-15	dolomite	oxy-dol-a22-15s1@6708	40.5	0.4	22.4	0.4	1.3	0.4
A0022-15	dolomite	oxy-dol-a22-15s1@6712	41.4	0.4	23.0	0.4	1.5	0.4
A0022-15	dolomite	oxy-dol-a22-15s1@6714	38.5	0.4	21.2	0.4	1.1	0.4
A0022-15	dolomite	oxy-dol-a22-15s1@6724	31.5	0.5	17.1	0.5	0.7	0.5
A0022-15	dolomite	oxy-dol-a22-15s1@6726	41.6	0.3	22.6	0.4	1.0	0.4
A0022-15	dolomite	oxy-dol-a22-15s1@6727	40.3	0.3	22.2	0.4	1.3	0.4
A0022-15	dolomite	oxy-dol-a22-15s1@6729	38.9	0.3	21.8	0.4	1.6	0.4
A0022-15	dolomite	oxy-dol-a22-15s1@6730	40.3	0.3	22.1	0.5	1.1	0.4
A0022-15	dolomite	oxy-dol-a22-15s1@6732	37.0	0.7	20.7	0.6	1.5	0.6
A0022-15	dolomite	oxy-dol-a22-15s1@6733	40.7	0.3	22.2	0.5	1.1	0.4
A0022-15	dolomite	oxy-dol-a22-15s1@6734	39.7	0.3	22.1	0.4	1.5	0.4
A0035-12	low-Ca pyroxene	oxy-opx-a35-12s2@7105	-4.5	0.4	-7.8	0.4	-5.5	0.3
A0035-12	low-Ca pyroxene	oxy-opx-a35-12s2@7106	-4.3	0.4	-7.8	0.3	-5.5	0.4
A0035-12	olivine	oxy-ol-a35-12s2@7107	-4.4	0.3	-7.9	0.4	-5.6	0.3
A0073-5	olivine	oxy-ol-a73-5s2@7055	-4.7	0.3	-6.0	0.5	-3.5	0.5
A0073-5	olivine	oxy-ol-a73-5s2@7056	-6.6	0.3	-7.6	0.5	-4.2	0.5
A0073-5	olivine	oxy-ol-a73-5s2@7068	-51.1	0.4	-49.3	0.4	-22.7	0.4
A0073-5	olivine	oxy-ol-a73-5s2@7070	-48.0	0.4	-48.1	0.3	-23.2	0.4
A0073-5	olivine	oxy-ol-a73-5s2@7079	-50.9	0.5	-49.3	0.4	-22.8	0.5
A0073-5	olivine	oxy-ol-a73-5s2@7080	-6.3	0.4	-9.4	0.4	-6.2	0.3
C0008-16	magnetite	oxy-mag-c8-16s1@6587	-5.3	0.6	-1.8	0.4	0.9	0.3
C0008-16	magnetite	oxy-mag-c8-16s1@6588	-5.3	0.6	-1.5	0.4	1.2	0.3
C0008-16	magnetite	oxy-mag-c8-16s1@6602	1.9	0.6	2.2	0.5	1.2	0.3
C0008-16	magnetite	oxy-mag-c8-16s1@6603	-0.6	0.7	0.6	0.5	0.9	0.3
C0008-16	magnetite	oxy-mag-c8-16s1@6606	-1.7	0.7	-0.5	0.5	0.4	0.4
C0008-16	magnetite	oxy-mag-c8-16s1@6616	0.0	0.7	1.7	0.5	1.7	0.3
C0008-16	magnetite	oxy-mag-c8-16s1@6617	-1.7	0.7	2.0	0.5	2.9	0.3
C0008-16	magnetite	oxy-mag-c8-16s1@6635	-4.0	0.7	-1.3	0.5	0.8	0.3
C0008-16	magnetite	oxy-mag-c8-16s1@6636	-1.6	0.6	0.0	0.5	0.8	0.3
C0008-16	dolomite	oxy-dol-c8-16s1@6584	30.7	0.4	17.9	0.3	2.0	0.4
C0008-16	dolomite	oxy-dol-c8-16s1@6586	29.2	0.5	17.7	0.3	2.5	0.4
C0008-16	dolomite	oxy-dol-c8-16s1@6598	35.4	0.4	20.1	0.3	1.7	0.3
C0008-16	dolomite	oxy-dol-c8-16s1@6599	30.7	0.4	16.1	0.4	0.1	0.4
C0008-16	dolomite	oxy-dol-c8-16s1@6601	34.7	0.4	19.9	0.4	1.8	0.3
C0008-16	dolomite	oxy-dol-c8-16s1@6605	33.2	0.4	18.3	0.4	1.0	0.4
C0008-16	dolomite	oxy-dol-c8-16s1@6618	33.0	0.4	18.9	0.3	1.7	0.3
C0008-16	dolomite	oxy-dol-c8-16s1@6628	34.1	0.4	19.0	0.4	1.2	0.3
C0008-16	dolomite	oxy-dol-c8-16s1@6629	34.0	0.4	19.1	0.4	1.4	0.3
C0008-16	dolomite	oxy-dol-c8-16s1@6630	34.3	0.4	19.2	0.3	1.3	0.4
C0008-16	dolomite	oxy-dol-c8-16s1@6631	35.1	0.4	19.5	0.3	1.3	0.3
C0008-16	dolomite	oxy-dol-c8-16s1@6632	34.8	0.4	19.7	0.3	1.7	0.3
C0008-16	dolomite	oxy-dol-c8-16s1@6633	34.2	0.4	19.3	0.4	1.5	0.3
C0008-16	olivine	oxy-ol-c8-16s1@6614	-6.8	0.3	-10.0	0.4	-6.5	0.3

Table S7: C and N isotopic compositions of 15×15 and 50×50 μm^2 matrix-areas. The variations of δ^{13}C and δ^{15}N values (1SD) among the 15×15 μm^2 matrix-areas within the particle are shown as well.

Spot	N/C	δ^{13}C	(1SE)	δ^{15}N	(1SE)
Ryugu					
cniso-mtx-a73-5s1@6206	0.0505	-19.9	2.9	39.1	7.3
cniso-mtx-a73-5s1@6207	0.0557	-7.8	3.0	44.8	3.8
cniso-mtx-a73-5s1@6208	0.0489	-2.2	5.5	51.2	4.8
cniso-mtx-a73-5s1@6209	0.0499	-13.8	3.7	44.1	4.0
cniso-mtx-a73-5s1@6210	0.0520	-5.3	2.2	53.6	3.4
cniso-mtx-a73-5s1@6215	0.0378	26.6	2.7	278.0	3.6
cniso-mtx-a73-5s1@6216	0.0561	-7.6	2.5	130.0	2.3
cniso-mtx-a73-5s1@6217	0.0412	-1.4	2.6	165.0	1.6
cniso-mtx-a73-5s1@6218	0.0282	-4.9	5.6	22.0	7.0
cniso-mtx-a73-5s1@6219	0.0464	-14.2	1.8	63.8	5.0
cniso-mtx-a73-5s1@6220	0.0456	-8.6	3.2	40.0	4.7
cniso-mtx-a73-5s1@6221	0.0433	-5.1	4.7	52.3	4.6
cniso-mtx-a73-5s1@6222	0.0447	-10.5	6.5	29.2	6.2
cniso-mtx-a73-5s1@6223	0.0541	-11.9	3.1	43.2	5.7
cniso-mtx-a73-5s1@6224	0.0512	-17.4	3.1	34.1	4.2
cniso-mtx-a73-5s1@6228	0.0428	-6.0	3.8	32.6	6.2
cniso-mtx-a73-5s1@6229	0.0455	-4.8	2.0	202.0	7.1
cniso-mtx-a73-5s1@6230	0.0610	-8.4	3.2	89.8	3.7
cniso-mtx-a73-5s1@6231	0.0464	-0.4	1.6	81.7	2.8
cniso-mtx-a73-5s1@6232	0.0371	-16.0	5.4	29.2	6.2
cniso-mtx-a73-5s1@6233	0.0461	-4.7	6.5	73.1	5.1
cniso-mtx-a73-5s1@6234	0.0482	-3.7	2.9	33.1	6.8
cniso-mtx-a73-5s1@6235	0.0483	-13.2	5.9	65.1	9.6
cniso-mtx-a73-5s1@6236	0.0267	16.0	8.6	405.0	13.1
cniso-mtx-a73-5s1@6237	0.0409	-12.6	5.1	81.7	7.6
1SD (n=25)	0.0079	9.9		89.7	
cniso-mtx-a78-12s1@6159	0.0534	-18.2	2.3	44.5	1.4
cniso-mtx-a78-12s1@6160	0.045	-8.0	2.8	149.0	3.9
cniso-mtx-a78-12s1@6161	0.0467	-9.8	3.5	47.5	3.7
cniso-mtx-a78-12s1@6162	0.0439	-10.7	2.3	52.2	2.7
cniso-mtx-a78-12s1@6163	0.0497	-9.6	2.8	52.0	5.2
cniso-mtx-a78-12s1@6164	0.0496	-13.4	2.6	49.1	4.6
cniso-mtx-a78-12s1@6165	0.0531	-10.5	3.0	55.2	4.0
cniso-mtx-a78-12s1@6166	0.0431	-3.6	3.5	55.9	5.0
cniso-mtx-a78-12s1@6167	0.0468	-9.0	2.6	44.5	4.0
cniso-mtx-a78-12s1@6168	0.051	8.3	3.4	260.0	4.8
cniso-mtx-a78-12s1@6177	0.0383	-2.7	3.1	77.2	4.8
cniso-mtx-a78-12s1@6178	0.039	4.3	5.5	66.1	5.9
cniso-mtx-a78-12s1@6179	0.0418	-9.9	3.3	51.2	6.3
cniso-mtx-a78-12s1@6184	0.0506	-15.6	2.3	26.6	5.1
cniso-mtx-a78-12s1@6185	0.0527	-14.3	3.1	60.8	5.4
cniso-mtx-a78-12s1@6186	0.0431	-3.1	1.7	39.6	4.1
cniso-mtx-a78-12s1@6187	0.0418	-13.0	2.0	53.8	5.3
cniso-mtx-a78-12s1@6188	0.0439	3.2	3.4	58.9	5.6
cniso-mtx-a78-12s1@6189	0.0394	-16.8	3.2	51.0	3.6
cniso-mtx-a78-12s1@6190	0.0430	-6.6	3.3	46.0	7.6
cniso-mtx-a78-12s1@6191	0.0360	-14.3	1.8	62.8	2.4
cniso-mtx-a78-12s1@6192	0.0468	-10.7	4.0	41.1	4.9
cniso-mtx-a78-12s1@6193	0.0410	-8.2	3.2	39.5	5.5
cniso-mtx-a78-12s1@6198	0.0449	-9.0	3.4	23.6	2.0
cniso-mtx-a78-12s1@6199	0.0489	1.0	1.6	61.3	4.3
cniso-mtx-a78-12s1@6200	0.0441	-9.1	3.1	56.2	3.3
cniso-mtx-a78-12s1@6180 (50 × 50)	0.0435	36.5	1.2	-2.1	1.5

Table S7: Continued

Spot	N/C	δ^{13}C	(1SE)	δ^{15}N	(1SE)
cniso-mtx-a78-12s1@6201 (50 × 50)	0.0434	64.5	1.9	0.2	1.0
1SD (n=26)	0.0048	46.1		6.6	
cniso-mtx-a85-1s1@5786	0.0325	-19.7	4.8	21.6	11.4
cniso-mtx-a85-1s1@5787 (50 × 50)	0.0357	43.9	1.2	-9.1	0.8
cniso-mtx-c19-10s1@6124	0.0274	-5.5	2.7	23.0	4.5
cniso-mtx-c19-10s1@6125	0.0290	-3.7	2.8	31.0	3.3
cniso-mtx-c19-10s1@6126	0.0239	4.0	11.4	17.7	7.5
cniso-mtx-c19-10s1@6127	0.0225	3.7	4.3	5.1	13.1
cniso-mtx-c19-10s1@6128	0.0284	-6.7	2.0	49.4	1.8
cniso-mtx-c19-10s1@6137	0.0327	-5.6	2.1	36.3	4.2
cniso-mtx-c19-10s1@6138	0.0278	-7.8	2.5	35.1	3.8
cniso-mtx-c19-10s1@6139	0.0287	-2.4	2.8	30.7	5.1
cniso-mtx-c19-10s1@6140	0.0278	-15.0	2.6	1.2	4.4
cniso-mtx-c19-10s1@6145	0.0287	-16.7	2.9	18.5	4.4
cniso-mtx-c19-10s1@6146	0.0313	-10.2	5.4	22.9	4.4
cniso-mtx-c19-10s1@6147	0.0258	-17.9	3.7	16.7	7.2
cniso-mtx-c19-10s1@6152	0.0271	-3.7	4.7	32.6	2.4
cniso-mtx-c19-10s1@6153	0.0241	-11.1	4.4	32.2	5.0
cniso-mtx-c19-10s1@6154	0.0248	-4.5	4.4	24.0	6.4
cniso-mtx-c19-10s1@6148 (50 × 50)	0.0300	25.2	0.9	-9.2	0.7
cniso-mtx-c19-10s1@6155 (50 × 50)	0.0277	41.5	1.9	-0.8	1.4
1SD (n=15)	0.0028	12.4		6.5	
cniso-mtx-c53-1s1@5794	0.0461	-3.6	2.1	71.6	2.6
cniso-mtx-c53-1s1@5795	0.0376	-10.1	1.4	56.6	4.1
cniso-mtx-c53-1s1@5796	0.0296	-6.1	2.6	59.4	1.6
cniso-mtx-c53-1s1@5797	0.0256	-10.9	2.5	42.3	3.9
cniso-mtx-c53-1s1@5798	0.0325	-17.2	2.9	46.6	4.0
cniso-mtx-c53-1s1@5803	0.0256	-4.7	1.3	37.9	3.6
cniso-mtx-c53-1s1@5805	0.0353	-12.2	5.1	47.3	4.4
cniso-mtx-c53-1s1@5806	0.0259	-9.8	5.3	77.9	6.1
cniso-mtx-c53-1s1@5808	0.0261	-5.1	4.0	47.2	2.8
cniso-mtx-c53-1s1@5809	0.0225	-6.8	3.1	68.8	5.3
cniso-mtx-c53-1s1@6060	0.0290	-7.3	2.2	78.6	2.1
cniso-mtx-c53-1s1@6061	0.0403	-8.8	2.5	44.6	2.3
cniso-mtx-c53-1s1@6062	0.0291	-7.2	1.7	48.6	2.3
cniso-mtx-c53-1s1@6063	0.0234	-11.1	5.6	47.0	6.0
cniso-mtx-c53-1s1@6064	0.0289	-5.9	1.0	48.1	2.6
cniso-mtx-c53-1s1@6065	0.0334	-11.6	2.1	66.7	4.3
cniso-mtx-c53-1s1@6089	0.0292	-12.8	3.9	51.2	3.4
cniso-mtx-c53-1s1@6090	0.0351	-3.6	2.4	80.5	4.3
cniso-mtx-c53-1s1@6095	0.0374	-7.6	4.1	43.9	5.2
cniso-mtx-c53-1s1@6096	0.0308	-4.6	2.8	47.1	2.3
cniso-mtx-c53-1s1@6097	0.0326	-10.3	1.4	58.7	2.5
cniso-mtx-c53-1s1@6098	0.0305	-13.0	2.0	67.5	5.1
cniso-mtx-c53-1s1@6099	0.0384	-15.0	3.4	59.3	6.2
cniso-mtx-c53-1s1@6106	0.0301	-0.1	2.5	41.6	1.9
cniso-mtx-c53-1s1@6107	0.0295	-5.7	1.8	54.5	4.2
cniso-mtx-c53-1s1@6113	0.0278	-9.8	4.0	21.7	4.6
cniso-mtx-c53-1s1@6114	0.0311	-17.0	2.9	39.0	4.1
cniso-mtx-c53-1s1@6119	0.0281	-10.8	2.9	50.9	3.4
cniso-mtx-c53-1s1@6120	0.0328	-16.8	3.6	73.9	4.6
cniso-mtx-c53-1s1@6121	0.0321	-11.2	4.8	68.6	2.4
cniso-mtx-c53-1s1@6122	0.0273	-3.1	3.3	27.1	2.8
cniso-mtx-c53-1s1@6123	0.0273	-15.2	2.9	79.1	5.2
cniso-mtx-c53-1s1@6132	0.0305	-7.4	2.8	86.5	3.7
cniso-mtx-c53-1s1@6133	0.0322	-5.1	4.4	85.1	5.9

Table S7: Continued

Spot	N/C	δ^{13}C	(1SE)	δ^{15}N	(1SE)
cniso-mtx-c53-1s1@6134	0.0291	-1.7	3.1	59.6	2.7
cniso-mtx-c53-1s1@6135	0.0284	1.4	0.7	43.4	2.8
cniso-mtx-c53-1s1@6136	0.0325	-3.2	3.4	65.3	6.1
cniso-mtx-c53-1s1@5799 (50 × 50)	0.0376	70.8	1.6	-12.2	1.0
cniso-mtx-c53-1s1@5810 (50 × 50)	0.0305	58.1	1.7	-13.8	1.3
cniso-mtx-c53-1s1@5814 (50 × 50)	0.0258	51.1	1.2	-7.5	0.9
cniso-mtx-c53-1s1@5815 (50 × 50)	0.0291	225.0	0.8	20.8	0.3
cniso-mtx-c53-1s1@6100 (50 × 50)	0.0286	50.5	0.9	-7.0	0.5
cniso-mtx-c53-1s1@6105 (50 × 50)	0.0330	2.6	0.8	19.5	0.6
cniso-mtx-c53-1s1@6112 (50 × 50)	0.0437	94.5	0.5	4.4	0.3
1SD (n=37)	0.0048	16.0		4.7	
Orgueil					
cniso-mtx-ogl1-2@4114	0.0546	-30.6	3.8	66.0	3.5
cniso-mtx-ogl1-2@4115	0.0511	-11.7	6.6	49.5	4.1
cniso-mtx-ogl1-2@4117	0.0500	-14.5	4.0	71.1	5.6
cniso-mtx-ogl1-2@4118	0.0547	-7.7	4.0	78.1	4.3
cniso-mtx-ogl1-2@4119	0.0377	-16.2	4.1	144.0	5.2
cniso-mtx-ogl1-2@4124	0.0419	-2.6	4.2	74.1	5.9
cniso-mtx-ogl1-2@4125	0.0482	-9.9	2.5	54.7	4.1
cniso-mtx-ogl1-2@4126	0.0539	-11.7	4.9	72.5	4.8
cniso-mtx-ogl1-2@4127	0.0412	-16.0	5.3	85.3	5.4
cniso-mtx-ogl1-2@4128	0.0474	-32.7	14.7	73.4	6.7
cniso-mtx-ogl1-2@4129	0.0495	-4.2	3.3	63.2	4.6
cniso-mtx-ogl1-2@4130	0.0408	-19.7	5.7	52.9	7.1
cniso-mtx-ogl1-2@4131	0.0461	-3.9	4.3	64.1	3.7
cniso-mtx-ogl1-2@4132	0.0553	-6.4	3.0	51.3	5.3
cniso-mtx-ogl1-2@4133	0.0451	-10.0	6.8	46.1	4.8
cniso-mtx-ogl1-2@4134	0.0485	-14.4	3.9	37.9	5.1
cniso-mtx-ogl1-2@4135	0.0479	-10.6	2.6	73.3	4.3
cniso-mtx-ogl1-2@4136	0.0483	-0.8	2.6	99.4	3.8
cniso-mtx-ogl1-2@6044	0.0562	-2.7	3.2	41.3	4.3
cniso-mtx-ogl1-2@6045	0.0473	-16.4	1.4	47.6	4.3
cniso-mtx-ogl1-2@6046	0.0597	-16.9	3.4	96.8	10.7
cniso-mtx-ogl1-2@6047	0.0532	-4.4	2.7	97.5	3.7
cniso-mtx-ogl1-2@6056	0.0455	-7.1	3.0	52.4	3.6
cniso-mtx-ogl1-2@6057	0.0444	-12.5	2.4	55.7	2.4
cniso-mtx-ogl1-2@6058	0.0443	-18.6	2.9	46.0	6.0
cniso-mtx-ogl1-2@6059	0.0428	-17.6	2.5	84.9	4.2
cniso-mtx-ogl1-2@6081	0.0420	-17.0	2.3	71.8	3.3
cniso-mtx-ogl1-2@6082	0.0470	-12.0	4.8	57.3	4.4
cniso-mtx-ogl1-2@6083	0.0438	-8.4	3.1	77.5	3.7
cniso-mtx-ogl1-2@6084	0.0425	-8.5	4.7	66.3	4.1
cniso-mtx-ogl1-2@6085	0.0613	-13.7	5.4	44.1	3.3
1SD (n=31)	0.0058	7.3		22.0	

Isotopic compositions of Orgueil (CI1) determined in this study are also shown.

Table S8: C and N isotopic compositions of micro-OM.

Sample & area	Size (μm^2)	δ^{13}C	(1SE)	δ^{15}N	(1SE)
A0073-5 (n = 16)					
@6206	4.0	5	50	526	58
@6215	29.7	59	17	511	20
@6215	1.1	33	96	762	105
@6216	19.1	29	22	368	27
@6217	20.4	1	19	480	22
@6217	9.5	-4	38	92	51
@6217	2.4	-4	77	14	109
@6218	19.3	5	44	-87	66
@6221	2.4	5	123	317	153
@6222	3.5	36	77	-108	119
@6229	7.0	36	47	751	52
@6229	1.3	-5	99	345	121
@6231	4.2	31	49	212	64
@6231	3.3	23	62	121	85
@6233	1.5	13	139	442	167
@6236	18.9	31	69	633	78
A0078-12 (n = 14)					
@6160	4.4	28	46	544	53
@6168	4.6	66	38	1131	38
@6177	4.2	2	69	442	82
@6180	1.2	-10	175	-8	250
@6180	1.2	30	171	7	247
@6180	7.9	-5	73	44	102
@6180	5.5	-17	90	0	128
@6180	1.8	6	155	37	218
@6180	4.3	2	119	184	157
@6184	4.8	20	35	-133	54
@6184	5.5	16	39	395	48
@6201	5.5	14	67	869	71
@6201	3.7	28	77	244	100
@6201	1.2	-15	146	51	203
A0085-1 (n = 1)					
@5787	23.2	13	36	-61	53
C0019-10 (n = 59)					
@6124	22.0	2	30	38	42
@6124	2.2	-13	110	57	152
@6124	26.4	-5	27	16	38
@6124	1.3	-2	132	9	188
@6124	1.3	-26	155	-6	220
@6124	1.5	-4	137	51	192
@6125	2.4	-23	93	59	127
@6125	7.9	-14	50	24	70
@6125	5.3	-9	58	22	81
@6125	1.3	-3	110	29	156
@6127	6.8	7	108	-76	162
@6128	1.3	8	115	13	164
@6128	4.8	3	57	130	77
@6128	10.8	-10	38	17	53
@6128	1.5	1	112	60	155
@6128	1.3	0	109	38	154
@6128	4.6	-7	52	140	70
@6137	16.0	7	27	39	38
@6138	2.0	-9	91	122	123
@6138	9.9	9	37	53	52
@6138	6.6	0	46	38	65

Table S8: Continued

Sample & area	Size (μm^2)	δ^{13}C	(1SE)	δ^{15}N	(1SE)
@6139	15.6	-5	34	9	49
@6139	4.8	11	55	36	78
@6139	1.3	2	128	6	183
@6139	7.5	5	44	89	60
@6140	18.7	-27	33	-22	47
@6140	2.4	-3	87	17	124
@6140	1.1	-19	150	61	207
@6145	3.7	-8	85	148	113
@6147	11.2	-6	59	34	84
@6148	25.0	3	26	19	37
@6148	15.9	13	29	-7	42
@6148	4.9	15	63	51	89
@6148	12.8	4	37	46	51
@6148	3.1	-9	76	36	107
@6148	2.4	-15	88	7	125
@6148	29.9	20	16	-75	24
@6148	1.2	17	94	160	126
@6148	6.7	15	42	381	52
@6148	4.9	-16	88	24	124
@6148	1.2	-18	137	15	193
@6148	4.9	-5	95	61	131
@6148	1.8	3	118	51	165
@6148	3.7	-4	62	70	85
@6148	16.5	-13	38	17	53
@6148	2.4	-33	146	-18	208
@6148	1.8	-4	195	-6	279
@6148	3.1	-19	74	136	98
@6148	11.6	-5	46	39	64
@6148	7.3	-15	88	-36	127
@6152	23.5	-7	25	37	35
@6152	6.6	-9	57	42	80
@6153	18.7	9	33	50	46
@6153	1.3	-11	153	37	215
@6155	5.5	8	118	45	165
@6155	30.5	40	38	283	49
@6155	1.2	-12	205	12	290
@6155	4.3	12	142	165	190
@6155	34.2	1	44	-3	63
C0053-1 (n = 79)					
@5799	26.3	-14	51	40	70
@5799	1.8	-7	132	232	169
@5810	6.1	22	97	161	129
@5810	4.3	-18	121	17	170
@5814	1.2	20	117	51	164
@5814	2.4	9	85	106	115
@5814	5.5	2	56	30	79
@5815	22.0	6	25	173	34
@5815	39.7	5	22	157	29
@5815	4.9	-2	56	106	76
@6062	4.8	3	45	-2	64
@6062	3.5	-29	64	63	88
@6065	41.3	-5	17	90	23
@6090	2.0	-16	93	63	128
@6090	10.3	-9	37	69	52
@6090	2.0	6	83	96	113
@6090	1.1	24	112	32	160

Table S8: Continued

Sample & area	Size (μm^2)	δ^{13}C	(1SE)	δ^{15}N	(1SE)
@6098	7.5	-11	48	59	67
@6100	1.2	22	138	193	183
@6100	3.7	6	69	56	97
@6100	1.8	-22	109	58	150
@6100	7.3	-13	47	115	63
@6100	1.2	4	151	141	202
@6100	5.5	5	165	27	234
@6100	10.4	-7	40	39	56
@6100	27.5	0	23	28	32
@6100	29.3	-1	26	30	37
@6100	14.7	-1	36	72	49
@6100	1.8	19	105	66	146
@6100	1.8	17	99	-50	146
@6100	4.9	6	64	276	81
@6100	19.5	4	29	-93	44
@6100	7.9	1	54	34	75
@6105	8.5	4	50	85	69
@6105	1.8	-3	109	45	152
@6105	4.3	8	75	150	100
@6105	1.2	48	134	125	186
@6105	103.8	96	6	-147	10
@6105	3.1	8	86	132	116
@6105	6.7	-8	48	15	68
@6105	2.4	7	94	32	133
@6105	6.1	11	53	43	75
@6105	12.2	1	37	71	51
@6105	3.1	-11	70	-10	100
@6105	26.9	1	27	64	37
@6105	11.6	2	36	132	49
@6105	1.8	5	97	44	137
@6105	5.5	-5	60	24	85
@6106	5.9	-4	52	62	73
@6106	1.5	-35	96	-20	137
@6106	5.9	14	52	33	74
@6106	3.7	3	58	39	82
@6106	3.7	9	63	95	86
@6107	2.0	6	86	128	116
@6112	53.1	-6	18	65	25
@6112	40.9	-5	20	48	28
@6112	1.2	25	132	99	182
@6112	5.5	-9	55	93	75
@6112	1.8	-10	96	50	134
@6112	7.3	-9	53	60	74
@6112	3.1	-21	109	47	152
@6112	7.3	-11	52	57	73
@6112	5.5	2	57	71	79
@6112	1.8	-12	110	126	147
@6112	7.3	-8	53	63	73
@6112	9.2	-3	47	80	65
@6112	4.3	-4	64	72	89
@6112	9.2	-3	41	74	57
@6112	3.7	1	62	105	84
@6112	1.2	-13	119	134	159
@6112	2.4	17	67	221	88
@6112	1.2	4	95	111	130
@6112	4.3	7	62	89	85

Table S8: Continued

Sample & area	Size (μm^2)	δ^{13}C	(1SE)	δ^{15}N	(1SE)
@6112	1.2	0	131	101	179
@6112	1.2	6	104	54	146
@6112	1.8	18	72	152	97
@6120	1.5	-21	142	289	177
@6133	1.8	-10	102	109	138
@6134	5.5	-7	71	96	97

The total number of micro-OMs identified is 169. Micro-OM with error more than 300‰ in either δ^{13}C and δ^{15}N is not listed.

Table S9: The temperatures estimated from O isotopic compositions of magnetite and dolomite.

Sample	Phase	δ^{18}O	(2SD)	$\Delta\delta^{18}$O		(B95%)	T /°C		(B95%)
C0008-16	magnetite	−2.0	4.8		+	2.4		+	14.7
C0008-16	dolomite	33.3	3.9	35.4	−	2.5	8.5	−	13.0
A0022-15	magnetite	4.9	2.9		+	2.0		+	13.6
A0022-15	dolomite	38.4	5.9	33.5	−	2.1	19.7	−	11.8

The O isotope equilibrium temperature was calculated using the parameters of Zheng 286, 287)

Table S10: The Cr isotopic composition and ^{55}Mn/^{52}Cr of dolomites in A0022-15, A0033-15, and C0008-16.

Spot	^{55}Mn/^{52}Cr	(1SE)	^{53}Cr/^{52}Cr	(1SE)
mncr-dol-a22-15s1@6960	10772	319	0.1554	0.0081
mncr-dol-a22-15s1@6961	3167	67	0.1273	0.0051
mncr-dol-a22-15s1@6962	2187	40	0.1235	0.0043
mncr-dol-a22-15s1@6963	90.1	0.4	0.1144	0.0008
mncr-dol-a22-15s1@6964	96.9	0.4	0.1133	0.0008
mncr-dol-a22-15s1@6965	606	4	0.1154	0.0015
mncr-dol-a22-15s1@6966	63.7	0.1	0.1141	0.0003
mncr-dol-a22-15s1@6967	1011	6	0.1172	0.0013
mncr-dol-a22-15s1@6968	287	1	0.1144	0.0010
mncr-dol-a22-15s1@6970	243	1	0.1156	0.0009
mncr-dol-a22-15s1@6971	1228	23	0.1154	0.0041
mncr-dol-a22-15s1@6972	352	2	0.1143	0.0015
mncr-dol-a22-15s1@6973	161.2	0.4	0.1156	0.0006
mncr-dol-a22-15s1@6974	922	6	0.1186	0.0015
mncr-dol-a22-15s1@6975	460	3	0.1151	0.0016
mncr-dol-a22-15s1@6977	628	4	0.1178	0.0016
mncr-dol-a22-15s1@6978	734	8	0.1134	0.0024
mncr-dol-a33-15s1@6980	146.2	0.6	0.1149	0.0009
mncr-dol-a33-15s1@6982	322	1	0.1143	0.0010
mncr-dol-a33-15s1@6983	1455	18	0.1233	0.0029
mncr-dol-a33-15s1@6984	55.45	0.08	0.1138	0.0003
mncr-dol-a33-15s1@6985	36.67	0.04	0.1136	0.0002
mncr-dol-a33-15s1@6986	1891	23	0.1189	0.0028
mncr-dol-a33-15s1@6988	235.3	0.9	0.1141	0.0009
mncr-dol-a33-15s1@6989	1528	21	0.1251	0.0032
mncr-dol-a33-15s1@6991	7005	172	0.1428	0.0063
mncr-dol-a33-15s1@6993	158.6	0.5	0.1123	0.0007
mncr-dol-a33-15s1@6994	115.4	0.4	0.1141	0.0008
mncr-dol-a33-15s1@6995	278	1	0.1157	0.0008
mncr-dol-a33-15s1@6996	83.6	0.2	0.1141	0.0005
mncr-dol-a33-15s1@6998	128.5	0.4	0.1136	0.0007
mncr-dol-a33-15s1@6999	92.8	0.3	0.1136	0.0007
mncr-dol-a33-15s1@7000	90.2	0.3	0.1138	0.0007
mncr-dol-a33-15s1@7001	142.9	0.3	0.1160	0.0005
mncr-dol-a33-15s1@7002	1625	19	0.1216	0.0027
mncr-dol-a33-15s1@7003	49.97	0.09	0.1143	0.0004
mncr-dol-a33-15s1@7007	346	1	0.1165	0.0009
mncr-dol-a33-15s1@7008	1339	11	0.1188	0.0019
mncr-dol-a33-15s1@7009	636	3	0.1170	0.0011
mncr-dol-a33-15s1@7010	1063	7	0.1203	0.0015
mncr-dol-a33-15s1@7011	1199	16	0.1194	0.0031
mncr-dol-a33-15s1@7012	1327	16	0.1180	0.0028
mncr-dol-c8-16s1@7020	8215	118	0.1503	0.0038
mncr-dol-c8-16s1@7021	4821	80	0.1283	0.0040
mncr-dol-c8-16s1@7022	19601	463	0.2017	0.0077
mncr-dol-c8-16s1@7023	15127	291	0.1720	0.0056
mncr-dol-c8-16s1@7024	6201	82	0.1434	0.0034
mncr-dol-c8-16s1@7025	209.8	0.9	0.1143	0.0010
mncr-dol-c8-16s1@7026	5011	86	0.1334	0.0042
mncr-dol-c8-16s1@7028	5075	69	0.1369	0.0034
mncr-dol-c8-16s1@7029	4321	56	0.1322	0.0032
mncr-dol-c8-16s1@7030	8254	164	0.1430	0.0051
mncr-dol-c8-16s1@7031	6978	178	0.1445	0.0066
mncr-dol-c8-16s1@7032	13126	318	0.1670	0.0069
mncr-dol-c8-16s1@7033	12731	357	0.1683	0.0081

Table S10: Continued

Spot	^{55}Mn/^{52}Cr	(1SE)	^{53}Cr/^{52}Cr	(1SE)
mncr-dol-c8-16s1@7034	14502	280	0.1694	0.0056
mncr-dol-c8-16s1@7035	485	3	0.1152	0.0013
mncr-dol-c8-16s1@7036	402	2	0.1152	0.0012
mncr-dol-c8-16s1@7037	1772	15	0.1186	0.0019
mncr-dol-c8-16s1@7039	144.2	0.5	0.1147	0.0007
mncr-dol-c8-16s1@7040	342	2	0.1174	0.0014
mncr-dol-c8-16s1@7041	3134	61	0.1255	0.0046

Table S11: Aliquots used for bulk analyses.

Session	Acquisition		A0022	A0033	A0035	A0048	A0073	A0078	A0085	C0008	C0019	C0027	C0039	C0047
I	Major, Minor & Trace	Aliquot	A0022-4	A0033-10	A0035-2	A0048-4	A0073-6	A0078-16	A0085-5	C0008-11	C0019-7	C0027-4	C0039-6	C0047-7
		Weight (g)	0.000372	0.000197	0.000523	0.000210	0.000189	0.000169	0.000148	0.000281	0.000218	0.000250	0.000203	0.000151
		Remarks	h	h	m	m	m	m	m	h	h	h	m	m
II	B, HFSE & Ti	Aliquot	A0022-5	A0033-11		A0048-6		A0078-18		C0008-13	C0019-9	C0027-5		
		Weight (g)	0.000242	0.000148		0.000146		0.000090		0.000221	0.000242	0.000143		
		Remarks	h, Al	h		h		h, Al		h	h, Al	h, Al		
III	Cr & S	Aliquot	A0022-3	A0033-9		A0048-5		A0078-17		C0008-12	C0019-8	C0027-3		
		Weight (g)	0.000181	0.000108		0.000146		0.000045		0.000155	0.000108	0.000153		
		Remarks	h	h		h		h		h	h	h		
IV	HSE	Aliquot	*A0022-17 A0022-19 A0022-20 *A0022-21	*A0033-19 A0033-21		*A0048-11 A0048-13				*C0008-17 C0008-21 C0008-22 *C0008-23	*C0019-16 C0019-18			
		Weight (g)	*0.000154 0.000205 0.000265 *0.000161	*0.000254 0.000276		*0.000157 0.000232				*0.000250 0.000259 0.000216 *0.000177	*0.000164 0.000247			
		Remarks	h	h		h								
V	Ge,As,Se & Te	Aliquot	A0022-18	A0033-20		A0048-12				C0008-19	C0019-17			
		Weight (g)	0.000128	0.000212		0.000143				0.000200	0.000152			
		Remarks	h	h		h				h	h			
VI	Ca & Cr isotopes	Aliquot	A0022-16											
		Weight (g)	0.000444											
		Remarks	h											
VII	H isotope	Aliquot	A0022-7	A0033-5	A0035-9	A0048-8		A0078-14	A0085-3	C0008-6	C0019-4	C0027-7		
		Weight (g)	0.000137	0.000172	0.000074	0.000119		0.000124	0.000057	0.000317	0.000121	0.000147		
		Remarks	h	h	h	h		h	h	h	h	h		
VIII	C & N isotopes	Aliquot	A0022-8	A0033-16	A0035-4	A0048-7	A0073-3	A0078-2˜9		C0008-7	C0019-3	C0027-6	C0039-3	C0047-4
		Weight (g)	0.000557	0.000532	0.000131	0.000578	0.000113	0.000757		0.000765	0.000583	0.000538	0.000173	0.000103
		Remarks	h	h	h	h	h	h		h	h	h	h	h
IX	C_{TOC}	Aliquot	A0022-10	A0033-18		A0048-9	A0073-4	A0078-19		C0008-14	C0019-6	C0027-9	C0039-4	C0047-5
		Weight (g)	0.000114	0.000092		0.000118	0.000096	0.000027		0.000114	0.000106	0.000107	0.000116	0.000111
		Remarks	h	h		h	h	h		h	h	h	h	h
X	O isotope	Aliquot	A0022-9	A0033-4						C0008-9	C0019-5			
		Weight (g)	0.000373	0.000568						0.000343	0.000361			
		Remarks	h	h						h	h			
XI	Ne isotope	Aliquot	A0022-2	A0033-13,14	A0035-7,8,10,11	A0048-2	A0073-2	A0078-11	A0085-2	C0008-5	C0019-2	C0027-2	C0039-2	C0047-2,3
		Weight (g)	0.000011	0.000051	0.000126	0.000063	0.000018	0.000024	0.000122	0.000072	0.000024	0.000066	0.000012	0.000046
		Remarks	h	h	h	h	h	h	h	h, (n=2)	h	h	h	h
		Weight total (g)	0.003344	0.002610	0.000854	0.001912	0.000416	0.001236	0.000327	0.003370	0.002326	0.001404	0.000504	0.000411

Table S11: Continued

Session	Acquisition		C0053_F1	C0053_F2	C0053	C0079	C0081	C0082	TD1	TD2	Total	Orgueil	Allende
I	Major, Minor & Trace	Aliquot	C0053-2	C0053-6	C0053-2,6	C0079-8	C0081-4	C0082-3				(n=9)	(n=4)
		Weight (g)	0.000403	0.000178	0.000581	0.000228	0.000322	0.000367	0.001808	0.002601	0.004409	0.002920	0.02196
		Remarks	m	h, b		h	m	m					
II	B, HFSE & Ti	Aliquot			C0053-3	C0079-9	C0081-3	C0082-4				(n=5)	(n=4)
		Weight (g)			0.000165	0.000191	0.000247	0.000234	0.000626	0.001443	0.002069	0.001563	0.01749
		Remarks			m	h, Al	m	m					
III	Cr & S	Aliquot			C0053-4	C0079-7	C0081-2	C0082-5				(n=4)	(n=4)
		Weight (g)			0.000131	0.000126	0.000270	0.000251	0.000480	0.001194	0.001674	0.000779	0.01669
		Remarks			m	m	m	m					
IV	HSE	Aliquot				*C0079-13						(n=4)	(n=2)
		Weight (g)				*0.000139			0.001704	0.001452	0.003156	0.002195	*0.00468
												(n=2)	
									(*0.000726)	(*0.000730)	(*0.001456)	(*0.000769)	
		Remarks				h							
V	Ge,As,Se & Te	Aliquot				C0079-14						(n=5)	(n=4)
		Weight (g)				0.000106			0.000483	0.000458	0.000941	0.001412	0.02389
		Remarks				h							
VI	Ca & Cr isotopes	Aliquot					C0081-5						
		Weight (g)					0.000457		0.000444	0.000457	0.000901		
		Remarks					m						
VII	H isotope	Aliquot			C0053-8	C0079-3	C0081-8	C0082-10					
		Weight (g)			0.000135	0.000145	0.000130	0.000126	0.000683	0.001121	0.001804		
		Remarks			h	h	h	h					
VIII	C & N isotopes	Aliquot				C0079-4	C0081-7	C0082-9					
		Weight (g)				0.000571	0.000568	0.000650	0.002668	0.003951	0.006619		
		Remarks				h	h	h					
IX	C_{TOC}	Aliquot				C0079-10	C0081-9	C0082-11					
		Weight (g)				0.000122	0.000088	0.000107	0.000447	0.000871	0.001318		
		Remarks				h	h	h					
X	O isotope	Aliquot				C0079-5							
		Weight (g)				0.000330			0.000941	0.001034	0.001975		
		Remarks				h							
XI	Ne isotope	Aliquot			C0053-5	C0079-2	C0081-6	C0082-2					
		Weight (g)			0.000025	0.000036	0.000048	0.000015	0.000415	0.000344	0.000759		
		Remarks			h	h	h	h					
		Weight total (g)	0.000403	0.000178	0.001037	0.001994	0.002130	0.001750	0.010699	0.014926	0.025625	0.008869	0.084710

Remarks on aliquots denote: [m], prepared by the ultra-microtome; [h], hand-picked; [b], decomposed using bomb; [Al], decomposed with Al addition. The aliquots marked with * in Session IV were analyzed for Os concentration. Weight of Orgueil (CI1) and Allende (CV3) show total weight of aliquot for each session. Further details are described in Supplementary Text ST1.4.

Table S12: Elemental abundances of bulk Ryugu particles.

	Session	Equipment	Method	Unit	DL	A0022	A0033	A0035	A0048	A0073	A0078	A0085	C0008	C0019	C0027	C0039	C0047	C0053_F1
[H]	VII			cg g^{-1}		1.11	0.694	1.3	1.12	N.A.	1.03	0.98	0.974	1.02	1.07	N.A.	N.A.	-
[Li]	I-1	ICP-QMS	Sm-IS	μg g^{-1}	0.01	1.39	1.26	1.52	1.55	1.50	1.83	1.23	1.44	1.55	1.62	1.81	1.38	1.52
[Be]	I-1	ICP-QMS	Sm-IS	μg g^{-1}	0.005	B.D.L.	0.00860	0.0235	0.0228	0.0237	0.0292	B.D.L.	0.0203	0.0220	0.00381	0.0159	0.0295	0.0175
[B]	II-1	ICP-QMS	ID	μg g^{-1}	0.2	1.15	0.878	N.A.	2.96	N.A.	2.0	N.A.	0.881	0.993	1.75	N.A.	N.A.	-
[C]$_{\mathrm{TC}}$	VIII			cg g^{-1}		4.02	5.39	4.12	3.39	3.40	3.48	N.A.	3.70	3.17	3.16	3.34	2.79	-
[C]$_{\mathrm{TOC}}$	IX			cg g^{-1}		1.88	2.4	N.A.	3.08	3.1	1.8	N.A.	3.27	2.95	2.82	3.35	3.03	-
[C]$_{\mathrm{carb}}$	VIII,IX			cg g^{-1}		2.14	3.0	N.A.	0.32	0.3	1.7	N.A.	0.43	0.22	0.34	N.D.	N.D.	-
[N]	VIII			cg g^{-1}		0.117	0.166	0.193	0.129	0.193	0.181	N.A.	0.159	0.101	0.103	0.110	0.096	-
[Ne]	XI			ng g^{-1}		0.67	0.20	1.47	3.8	7.1	98	12.3	0.62	1.4	0.73	2.7	1.8	-
[Na]	I-2	ICP-SFMS	Sr-IS	cg g^{-1}	0.0002	0.576	0.543	0.678	0.726	0.810	0.481	0.415	0.620	0.541	0.573	0.594	0.619	0.548
[Mg]	I-2	ICP-SFMS	Sr-IS	cg g^{-1}	0.00004	10.5	11.4	11.6	13.0	13.7	12.1	9.96	11.9	10.3	11.5	12.0	10.2	11.3
[Al]	I-2	ICP-SFMS	Sr-IS	cg g^{-1}	0.00005	0.844	0.841	1.05	1.14	1.08	1.07	0.893	0.986	0.910	0.978	1.02	0.905	0.908
[Si]	I-2		Calc	cg g^{-1}		12.2	13.9	12.6	14.3	15.0	12.9	10.2	12.9	11.4	12.9	13.2	11.7	12.6
[P]	I-2	ICP-SFMS	Sr-IS	cg g^{-1}	0.00002	0.194	0.149	0.100	0.0856	0.120	0.0779	0.0178	0.121	0.166	0.199	0.186	0.136	0.117
[S]	III	ICP-SFMS	ID	cg g^{-1}	0.0001	5.70	5.40	N.A.	5.40	N.A.	5.5	N.A.	5.38	5.56	6.22	N.A.	N.A.	-
[K]	I-2	ICP-SFMS	Sr-IS	cg g^{-1}	0.00004	0.0489	0.0427	0.0639	0.0559	0.0697	0.0646	0.0519	0.0545	0.0540	0.0522	0.0558	0.0566	0.0625
[Ca]	I-2	ICP-SFMS	Sr-IS	cg g^{-1}	0.00004	2.45	2.02	0.910	0.501	1.06	0.556	0.789	1.00	0.947	1.04	1.06	1.25	1.26
[Sc]	I-2	ICP-SFMS	Sr-IS	μg g^{-1}	0.004	6.12	6.31	7.21	8.04	7.72	7.59	5.58	6.22	5.13	6.28	7.34	6.31	6.85
[Ti]	II-2	ICP-SFMS	Nb-IS	cg g^{-1}	0.0002	0.0537	0.0513	N.A.	0.0393	N.A.	0.053	N.A.	0.0449	0.0464	0.0452	N.A.	N.A.	-
[V]	I-2	ICP-SFMS	Sr-IS	μg g^{-1}	0.008	52.5	53.9	66.7	68.8	66.7	64.0	55.0	58.4	58.7	61.4	62.2	57.2	58.6
[Cr]	III	ICP-SFMS	ID	cg g^{-1}	0.000007	0.215	0.210	N.A.	0.264	N.A.	0.24	N.A.	0.235	0.266	0.264	N.A.	N.A.	-
[Mn]	I-2	ICP-SFMS	Sr-IS	cg g^{-1}	0.000005	0.281	0.369	0.182	0.138	0.216	0.131	0.187	0.225	0.142	0.155	0.167	0.262	0.256
[Fe]	I-2	ICP-SFMS	Sr-IS	cg g^{-1}	0.00002	17.3	18.8	20.8	23.6	24.6	23.9	19.1	23.3	20.1	23.6	23.5	20.1	21.2
[Co]	I-2	ICP-SFMS	Sr-IS	μg g^{-1}	0.004	485	493	646	732	685	632	534	640	589	626	642	564	587
[Ni]	I-2	ICP-SFMS	Sr-IS	cg g^{-1}	0.000003	1.15	1.04	1.31	1.43	1.49	1.51	1.11	1.14	1.07	1.20	1.38	1.18	1.31
[Cu]	I-2	ICP-SFMS	Sr-IS	μg g^{-1}	0.03	62.5	92.7	145	108	170	87.7	96.2	130	62.0	62.9	72.2	174	131
[Zn]	I-2	ICP-SFMS	Sr-IS	μg g^{-1}	0.05	333	308	367	435	366	421	336	361	329	353	387	321	366
[Ga]	I-2	ICP-SFMS	Sr-IS	μg g^{-1}	0.01	10.9	9.76	11.8	10.8	15.2	13.1	6.98	8.51	9.18	11.0	12.3	10.3	8.95
[Ge]	V	ICP-QMS	ID	μg g^{-1}	0.04	34.1	36.2	N.A.	34.0	N.A.	N.A.	N.A.	31.8	32.9	N.A.	N.A.	N.A.	N.A.
[As]	V	ICP-QMS	Ge-IS	μg g^{-1}	0.06	1.63	1.50	N.A.	2.15	N.A.	N.A.	N.A.	2.24	1.99	N.A.	N.A.	N.A.	N.A.
[Se]	V	ICP-QMS	ID	μg g^{-1}	0.1	17.2	20.1	N.A.	24.5	N.A.	N.A.	N.A.	21.9	23.4	N.A.	N.A.	N.A.	N.A.
[Rb]	I-1	ICP-QMS	Sm-IS	μg g^{-1}	0.003	1.98	1.73	2.59	1.92	3.61	2.74	2.23	2.39	2.26	2.24	1.92	2.32	2.67
[Sr]	I-1	ICP-QMS	Sm-IS	μg g^{-1}	0.09	22.1	15.8	6.83	4.55	8.90	5.23	5.37	7.86	9.76	10.5	10.6	8.84	10.0
[Y]	I-1	ICP-QMS	Sm-IS	μg g^{-1}	0.002	3.56	2.93	1.52	1.56	1.43	1.01	0.209	1.51	1.67	1.67	1.62	1.66	1.56
[Zr]	II-1	ICP-QMS	ID	μg g^{-1}	0.02	3.24	3.29	N.A.	4.33	N.A.	4.5	N.A.	3.79	4.27	4.23	N.A.	N.A.	-
[Nb]	II-1	ICP-QMS	Zr-IS	μg g^{-1}	0.006	0.309	0.285	N.A.	0.266	N.A.	0.35	N.A.	0.279	0.283	0.290	N.A.	N.A.	-
[Mo]	II-1	ICP-QMS	ID	μg g^{-1}	0.02	0.911	0.809	N.A.	1.12	N.A.	1.1	N.A.	0.885	1.07	1.05	N.A.	N.A.	-
[Ru]	IV-1	ICP-QMS	ID	μg g^{-1}	0.03	0.504	0.537	N.A.	0.654	N.A.	N.A.	N.A.	0.617	0.770	N.A.	N.A.	N.A.	-
[Pd]	IV-1	ICP-QMS	ID	μg g^{-1}	0.02	0.444	0.504	N.A.	0.603	N.A.	N.A.	N.A.	0.601	0.872	N.A.	N.A.	N.A.	-
[Cd]	I-1	ICP-QMS	Sm-IS	μg g^{-1}	0.003	0.642	0.511	0.712	0.794	0.691	0.781	0.641	0.673	0.701	0.688	0.760	0.696	0.664
[In]	I-1	ICP-QMS	Sm-IS	μg g^{-1}	0.0008	0.0724	*0.329	N.D.	N.D.	N.D.	N.D.	N.D.	0.0850	N.D.	*0.119	N.D.	N.D.	N.D.
[Sn]	II-1	ICP-QMS	ID	μg g^{-1}	0.2	1.31	1.35	N.A.	1.53	N.A.	0.86	N.A.	1.51	1.63	1.51	N.A.	N.A.	-
[Sb]	II-1	ICP-QMS	ID	μg g^{-1}	0.001	0.125	0.112	N.A.	0.191	N.A.	0.17	N.A.	0.169	0.151	0.152	N.A.	N.A.	-
[Te]	V	ICP-QMS	ID	μg g^{-1}	0.07	2.15	1.86	N.A.	2.69	N.A.	N.A.	N.A.	2.51	2.75	N.A.	N.A.	N.A.	-

Table S12: Continued

	Session	Equipment	Method	Unit	DL	A0022	A0033	A0035	A0048	A0073	A0078	A0085	C0008	C0019	C0027	C0039	C0047	C0053_F1
[Cs]	I-1	ICP-QMS	Sm-IS	$\mu g\ g^{-1}$	0.0007	0.203	0.176	0.262	0.154	0.316	0.241	0.176	0.230	0.120	0.138	0.144	0.232	0.310
[Ba]	I-1	ICP-QMS	Sm-IS	$\mu g\ g^{-1}$	0.02	4.54	4.25	2.80	2.09	2.96	2.25	2.06	2.47	3.26	3.12	3.58	3.11	3.24
[La]	I-1	ICP-QMS	Sm-IS	$\mu g\ g^{-1}$	0.0006	0.356	0.376	0.278	0.297	0.263	0.160	0.0932	0.251	0.272	0.261	0.253	0.301	0.287
[Ce]	I-1	ICP-QMS	Sm-IS	$\mu g\ g^{-1}$	0.001	0.966	1.02	0.709	0.747	0.699	0.428	0.235	0.631	0.721	0.690	0.666	0.775	0.731
[Pr]	I-1	ICP-QMS	Sm-IS	$\mu g\ g^{-1}$	0.0004	0.157	0.169	0.107	0.110	0.103	0.0640	0.0414	0.0962	0.111	0.105	0.0955	0.115	0.113
[Nd]	I-1	ICP-QMS	Sm-IS	$\mu g\ g^{-1}$	0.002	0.924	0.886	0.587	0.603	0.553	0.347	0.277	0.499	0.565	0.535	0.510	0.628	0.572
[Sm]	I-1	ICP-QMS	ID	$\mu g\ g^{-1}$	0.002	0.299	0.294	0.175	0.191	0.157	0.0988	0.0661	0.161	0.180	0.175	0.154	0.197	0.192
[Eu]	I-1	ICP-QMS	Sm-IS	$\mu g\ g^{-1}$	0.0002	0.123	0.127	0.0678	0.0732	0.0630	0.0429	0.0146	0.0585	0.0703	0.0694	0.0628	0.0797	0.0689
[Gd]	I-1	ICP-QMS	Sm-IS	$\mu g\ g^{-1}$	0.001	0.463	0.461	0.251	0.268	0.223	0.135	0.0542	0.225	0.268	0.234	0.236	0.274	0.237
[Tb]	I-1	ICP-QMS	Sm-IS	$\mu g\ g^{-1}$	0.001	0.0833	0.0808	0.0455	0.0451	0.0393	0.0265	0.00942	0.0411	0.0454	0.0428	0.0434	0.0513	0.0455
[Dy]	I-1	ICP-QMS	Sm-IS	$\mu g\ g^{-1}$	0.0001	0.614	0.578	0.304	0.321	0.274	0.194	0.0511	0.294	0.322	0.316	0.313	0.355	0.319
[Ho]	I-1	ICP-QMS	Sm-IS	$\mu g\ g^{-1}$	0.001	0.138	0.118	0.0647	0.0686	0.0578	0.0423	0.00850	0.0602	0.0698	0.0667	0.0659	0.0767	0.0666
[Er]	I-1	ICP-QMS	Sm-IS	$\mu g\ g^{-1}$	0.0001	0.420	0.363	0.193	0.191	0.180	0.137	0.0232	0.183	0.212	0.209	0.196	0.220	0.206
[Tm]	I-1	ICP-QMS	Sm-IS	$\mu g\ g^{-1}$	0.0005	0.0635	0.0544	0.0285	0.0302	0.0269	0.0208	0.00383	0.0271	0.0322	0.0332	0.0309	0.0341	0.0296
[Yb]	I-1	ICP-QMS	Sm-IS	$\mu g\ g^{-1}$	0.00004	0.404	0.358	0.198	0.200	0.188	0.138	0.0233	0.183	0.222	0.221	0.208	0.227	0.212
[Lu]	I-1	ICP-QMS	Sm-IS	$\mu g\ g^{-1}$	0.0004	0.0591	0.0535	0.0290	0.0289	0.0290	0.0205	0.00314	0.0276	0.0326	0.0323	0.0314	0.0343	0.0309
[Hf]	II-1	ICP-QMS	ID	$\mu g\ g^{-1}$	0.001	0.0938	0.0970	N.A.	0.121	N.A.	0.13	N.A.	0.108	0.121	0.121	N.A.	N.A.	-
[Ta]	II-1	ICP-QMS	Hf-IS	$\mu g\ g^{-1}$	0.0004	0.0465	0.0192	N.A.	0.0112	N.A.	0.010	N.A.	0.0128	*1.30	0.0161	N.A.	N.A.	-
[W]	II-1	ICP-QMS	ID	$\mu g\ g^{-1}$	0.04	0.105	0.0708	N.A.	0.0679	N.A.	0.16	N.A.	0.158	0.0789	0.0898	N.A.	N.A.	-
[Re]	IV-1	ICP-QMS	ID	$\mu g\ g^{-1}$	0.005	0.0337	0.0340	N.A.	0.0445	N.A.	N.A.	N.A.	0.0429	0.0579	N.A.	N.A.	N.A.	-
[Os]	IV-2	N-TIMS	ID	$\mu g\ g^{-1}$		0.420	0.400	N.A.	0.583	N.A.	N.A.	N.A.	0.475	0.477	N.A.	N.A.	N.A.	-
[Ir]	IV-1	ICP-QMS	ID	$\mu g\ g^{-1}$	0.006	0.360	0.373	N.A.	0.512	N.A.	N.A.	N.A.	0.448	0.708	N.A.	N.A.	N.A.	-
[Pt]	IV-1	ICP-QMS	ID	$\mu g\ g^{-1}$	0.009	0.716	0.718	N.A.	0.923	N.A.	N.A.	N.A.	0.859	0.931	N.A.	N.A.	N.A.	-
[Tl]	I-1	ICP-QMS	Sm-IS	$\mu g\ g^{-1}$	0.0004	0.0277	0.0737	0.0836	0.102	0.0614	0.0935	0.0456	0.0544	0.0549	0.112	0.0718	0.0426	0.0726
[Pb]	I-1	ICP-QMS	Sm-IS	$\mu g\ g^{-1}$	0.0001	2.61	3.20	2.96	3.68	3.17	3.40	3.06	3.07	3.28	3.05	3.43	3.43	3.19
[Bi]	I-1	ICP-QMS	Sm-IS	$\mu g\ g^{-1}$	0.0008	0.0909	0.0918	0.118	0.0459	0.126	0.126	0.0459	0.0105	0.110	0.123	0.132	0.115	0.0530
[Th]	I-1	ICP-QMS	Sm-IS	$\mu g\ g^{-1}$	0.001	0.0383	0.0395	0.0345	0.0397	0.0359	0.0259	0.00914	0.0323	0.0362	0.0351	0.0341	0.0342	0.0348
[U]	I-1	ICP-QMS	Sm-IS	$\mu g\ g^{-1}$	0.0004	0.0135	0.00834	0.0108	0.00820	0.00471	0.00741	0.00204	0.00758	0.0103	0.0101	0.00822	0.00416	0.00661

Table S12: Continued

	Session	Equipment	Method	Unit	DL	C0053_F2	C0053	C0079	C0081	C0082	†TD1	†TD2	†Bulk Ryugu	Orgueil	1σ%	Allende	1σ%
[H]	VII			cg g^{-1}		-	1.22	1.14	1.07	0.937	1.00	1.05	1.03	1.54		N.A.	
[Li]	I-1	ICP-QMS	Sm-IS	μg g^{-1}	0.01	1.18	1.42	1.58	1.33	1.63	1.47	1.51	1.50	1.27	11.5	1.68	5.0
[Be]	I-1	ICP-QMS	Sm-IS	μg g^{-1}	0.005	0.0130	0.0161	0.0117	0.00853	0.0151	0.0219	0.0152	0.0179	0.0173	31.4	0.0574	7.1
[B]	II-1	ICP-QMS	ID	μg g^{-1}	0.2	-	1.24	1.36	1.38	1.05	1.63	1.20	1.33	2.86	40.3	1.31	12.5
[C]$_{TC}$	VIII			cg g^{-1}		-	N.A.	3.24	5.22	5.34	3.98	3.93	3.95	3.16		N.A.	
[C]$_{TOC}$	IX			cg g^{-1}		-	N.A.	2.85	4.0	2.80	2.56	3.11	2.92	N.A.		N.A.	
[C]$_{carb}$	VIII,IX			cg g^{-1}		-	N.A.	0.39	1.2	2.54	1.43	0.82	1.03	N.A.		N.A.	
[N]	VIII			cg g^{-1}		-	N.A.	0.107	0.216	0.191	0.154	0.145	0.149	0.179		N.A.	
[Ne]	XI			ng g^{-1}		-	0.74	0.43	0.36	0.38	11	0.88	6.2	N.A.		N.A.	
[Na]	I-2	ICP-SFMS	Sr-IS	cg g^{-1}	0.0002	0.537	0.544	0.585	0.503	0.569	0.622	0.565	0.588	0.406	16.1	0.351	4.8
[Mg]	I-2	ICP-SFMS	Sr-IS	cg g^{-1}	0.00004	11.8	11.5	11.0	10.5	11.0	11.6	11.2	11.4	9.28	11.2	15.4	12.7
[Al]	I-2	ICP-SFMS	Sr-IS	cg g^{-1}	0.00005	0.852	0.891	0.949	0.903	0.954	0.988	0.938	0.958	0.873	13.0	1.75	5.7
[Si]	I-2		Calc	cg g^{-1}		13.1	12.7	12.0	12.0	12.4	12.9	12.4	12.6	10.1		-	
[P]	I-2	ICP-SFMS	Sr-IS	cg g^{-1}	0.00002	0.0985	0.111	0.127	0.110	0.205	0.116	0.147	0.135	0.0789	17.4	0.113	7.9
[S]	III	ICP-SFMS	ID	cg g^{-1}	0.0001	-	5.59	6.73	6.07	6.65	5.52	6.09	5.93	4.95	13.3	2.11	1.3
[K]	I-2	ICP-SFMS	Sr-IS	cg g^{-1}	0.00004	0.0439	0.0568	0.0546	0.0460	0.0560	0.0573	0.0542	0.0554	0.0508	19.6	0.0327	5.9
[Ca]	I-2	ICP-SFMS	Sr-IS	cg g^{-1}	0.00004	2.13	1.53	0.778	1.15	1.14	1.27	1.15	1.20	0.617	35.1	1.89	6.6
[Sc]	I-2	ICP-SFMS	Sr-IS	μg g^{-1}	0.004	5.81	6.53	7.57	6.38	7.26	6.94	6.58	6.73	5.74	8.2	11.8	2.7
[Ti]	II-2	ICP-SFMS	Nb-IS	cg g^{-1}	0.0002	-	0.0408	0.0509	0.0443	0.0540	0.0497	0.0469	0.0477	0.0428	6.9	0.0890	4.4
[V]	I-2	ICP-SFMS	Sr-IS	μg g^{-1}	0.008	69.2	61.8	67.0	68.2	60.1	61.4	61.9	61.7	52.0	16.6	96.7	6.6
[Cr]	III	ICP-SFMS	ID	cg g^{-1}	0.000007	-	0.231	0.276	0.248	0.285	0.231	0.259	0.251	0.204	1.4	0.321	1.9
[Mn]	I-2	ICP-SFMS	Sr-IS	cg g^{-1}	0.000005	0.433	0.310	0.145	0.230	0.171	0.217	0.214	0.215	0.196	20.8	0.153	6.0
[Fe]	I-2	ICP-SFMS	Sr-IS	cg g^{-1}	0.00002	20.9	21.1	22.8	19.9	21.4	20.7	21.7	21.3	19.4	11.3	24.6	13.3
[Co]	I-2	ICP-SFMS	Sr-IS	μg g^{-1}	0.004	546	575	659	579	606	600	605	603	620	29.5	684	10.1
[Ni]	I-2	ICP-SFMS	Sr-IS	cg g^{-1}	0.000003	1.04	1.22	1.49	1.29	1.34	1.28	1.26	1.27	1.48	33.0	1.51	4.5
[Cu]	I-2	ICP-SFMS	Sr-IS	μg g^{-1}	0.03	N.D.	131	86.3	134	156	111	116	114	137	40.5	113	5.6
[Zn]	I-2	ICP-SFMS	Sr-IS	μg g^{-1}	0.05	302	346	403	353	375	364	359	361	325	14.4	124	5.5
[Ga]	I-2	ICP-SFMS	Sr-IS	μg g^{-1}	0.01	7.98	8.65	11.4	9.68	11.7	11.4	10.1	10.6	8.84	19.6	5.12	12.4
[Ge]	V	ICP-QMS	ID	μg g^{-1}	0.04	N.A.	N.A.	31.0	N.A.	N.A.	35.0	32.0	33.5	36.3	8.9	15.1	2.9
[As]	V	ICP-QMS	Ge-IS	μg g^{-1}	0.06	N.A.	N.A.	2.40	N.A.	N.A.	1.73	2.19	1.95	2.01	10.6	1.65	9.1
[Se]	V	ICP-QMS	ID	μg g^{-1}	0.1	N.A.	N.A.	19.8	N.A.	N.A.	20.7	21.9	21.3	18.5	16.0	8.15	7.5
[Rb]	I-1	ICP-QMS	Sm-IS	μg g^{-1}	0.003	2.04	2.48	1.99	1.78	2.44	2.38	2.24	2.30	2.25	19.3	1.20	4.2
[Sr]	I-1	ICP-QMS	Sm-IS	μg g^{-1}	0.09	13.8	11.2	7.87	8.65	11.6	10.6	9.91	10.2	7.21	53.0	15.2	5.4
[Y]	I-1	ICP-QMS	Sm-IS	μg g^{-1}	0.002	1.82	1.64	1.53	1.67	1.86	1.93	1.66	1.77	1.22	9.5	2.63	1.2
[Zr]	II-1	ICP-QMS	ID	μg g^{-1}	0.02	-	3.48	4.33	4.01	4.76	3.69	4.14	4.01	3.53	7.4	6.75	3.9
[Nb]	II-1	ICP-QMS	Zr-IS	μg g^{-1}	0.006	-	0.276	0.310	0.285	0.308	0.300	0.290	0.293	0.258	9.5	0.508	3.9
[Mo]	II-1	ICP-QMS	ID	μg g^{-1}	0.02	-	0.953	1.11	1.00	1.15	0.959	1.03	1.01	0.857	8.8	1.63	4.5
[Ru]	IV-1	ICP-QMS	ID	μg g^{-1}	0.03	-	N.A.	0.701	N.A.	N.A.	0.548	0.669	0.604	0.603	9.5	1.10	21.0
[Pd]	IV-1	ICP-QMS	ID	μg g^{-1}	0.02	-	N.A.	0.633	N.A.	N.A.	0.499	0.681	0.583	0.537	3.4	0.741	23.3
[Cd]	I-1	ICP-QMS	Sm-IS	μg g^{-1}	0.003	0.568	0.634	0.710	0.740	0.760	0.684	0.700	0.693	0.793	18.9	0.426	8.2
[In]	I-1	ICP-QMS	Sm-IS	μg g^{-1}	0.0008	*0.0732	0.0732	N.D.	N.D.	N.D.	0.0724	0.0864	0.0829	N.A.		0.0293	4.2
[Sn]	II-1	ICP-QMS	ID	μg g^{-1}	0.2	-	1.81	1.95	1.73	2.06	1.31	1.75	1.62	1.32	5.7	0.546	4.6
[Sb]	II-1	ICP-QMS	ID	μg g^{-1}	0.001	-	0.161	0.146	0.183	0.265	0.143	0.178	0.168	0.179	24.1	0.0943	8.9
[Te]	V	ICP-QMS	ID	μg g^{-1}	0.07	-	N.A.	2.86	N.A.	N.A.	2.18	2.67	2.42	2.39	4.2	0.941	8.4

Table S12: Continued

	Session	Equipment	Method	Unit	DL	C0053_F2	C0053	C0079	C0081	C0082	†TD1	†TD2	†Bulk Ryugu	Orgueil	$1\sigma\%$	Allende	$1\sigma\%$
[Cs]	I-1	ICP-QMS	Sm-IS	μg g^{-1}	0.0007	0.211	0.280	0.144	0.200	0.150	0.225	0.194	0.207	0.192	14.9	0.0882	3.5
[Ba]	I-1	ICP-QMS	Sm-IS	μg g^{-1}	0.02	4.16	3.52	2.83	2.51	3.70	3.14	3.17	3.16	2.23	17.6	4.61	4.9
[La]	I-1	ICP-QMS	Sm-IS	μg g^{-1}	0.0006	0.319	0.297	0.289	0.254	0.302	0.279	0.278	0.278	0.207	35.7	0.531	3.5
[Ce]	I-1	ICP-QMS	Sm-IS	μg g^{-1}	0.001	0.821	0.759	0.762	0.660	0.791	0.734	0.721	0.727	0.527	29.6	1.32	2.9
[Pr]	I-1	ICP-QMS	Sm-IS	μg g^{-1}	0.0004	0.130	0.118	0.113	0.100	0.120	0.114	0.110	0.112	0.0773	25.8	0.202	4.4
[Nd]	I-1	ICP-QMS	Sm-IS	μg g^{-1}	0.002	0.708	0.613	0.604	0.510	0.636	0.639	0.572	0.599	0.396	22.8	1.08	2.8
[Sm]	I-1	ICP-QMS	ID	μg g^{-1}	0.002	0.211	0.198	0.186	0.154	0.197	0.197	0.180	0.187	0.130	12.9	0.333	2.6
[Eu]	I-1	ICP-QMS	Sm-IS	μg g^{-1}	0.0002	0.0833	0.0733	0.0687	0.0667	0.0785	0.0790	0.0701	0.0738	0.0518	9.8	0.110	3.5
[Gd]	I-1	ICP-QMS	Sm-IS	μg g^{-1}	0.001	0.303	0.257	0.237	0.233	0.263	0.290	0.248	0.265	0.193	9.7	0.448	4.5
[Tb]	I-1	ICP-QMS	Sm-IS	μg g^{-1}	0.001	0.0526	0.0477	0.0425	0.0436	0.0532	0.0517	0.0460	0.0483	0.0355	9.1	0.0772	4.5
[Dy]	I-1	ICP-QMS	Sm-IS	μg g^{-1}	0.0001	0.361	0.332	0.303	0.299	0.360	0.365	0.323	0.340	0.247	10.0	0.543	3.2
[Ho]	I-1	ICP-QMS	Sm-IS	μg g^{-1}	0.001	0.0745	0.0690	0.0642	0.0663	0.0796	0.0786	0.0688	0.0728	0.0527	10.8	0.111	2.0
[Er]	I-1	ICP-QMS	Sm-IS	μg g^{-1}	0.0001	0.225	0.212	0.190	0.207	0.234	0.238	0.208	0.220	0.155	8.2	0.321	1.2
[Tm]	I-1	ICP-QMS	Sm-IS	μg g^{-1}	0.0005	0.0354	0.0314	0.0292	0.0299	0.0364	0.0358	0.0316	0.0333	0.0236	9.4	0.0554	1.3
[Yb]	I-1	ICP-QMS	Sm-IS	μg g^{-1}	0.00004	0.235	0.219	0.195	0.199	0.235	0.237	0.213	0.223	0.159	9.0	0.337	1.4
[Lu]	I-1	ICP-QMS	Sm-IS	μg g^{-1}	0.0004	0.0351	0.0322	0.0283	0.0330	0.0367	0.0349	0.0322	0.0333	0.0240	8.5	0.0494	4.2
[Hf]	II-1	ICP-QMS	ID	μg g^{-1}	0.001	-	0.103	0.119	0.108	0.141	0.106	0.118	0.114	0.100	7.7	0.200	3.3
[Ta]	II-1	ICP-QMS	Hf-IS	μg g^{-1}	0.0004	-	0.0121	0.0151	*0.658	0.00735	0.0140	0.0123	0.0128	0.0117	10.0	0.0283	4.1
[W]	II-1	ICP-QMS	ID	μg g^{-1}	0.04	-	0.111	0.0960	0.0889	0.0924	0.0966	0.102	0.100	0.0916	9.1	0.190	6.8
[Re]	IV-1	ICP-QMS	ID	μg g^{-1}	0.005	-	N.A.	0.0386	N.A.	N.A.	0.0362	0.0467	0.0411	0.0389	8.8	0.0668	16.3
[Os]	IV-2	N-TIMS	ID	μg g^{-1}		-	N.A.	0.521	N.A.	N.A.	0.449	0.484	0.466	0.460	2.9	0.787	13.8
[Ir]	IV-1	ICP-QMS	ID	μg g^{-1}	0.006	-	N.A.	0.481	N.A.	N.A.	0.399	0.525	0.457	0.413	3.9	0.714	15.0
[Pt]	IV-1	ICP-QMS	ID	μg g^{-1}	0.009	-	N.A.	0.897	N.A.	N.A.	0.764	0.883	0.819	0.799	4.8	1.40	17.2
[Tl]	I-1	ICP-QMS	Sm-IS	μg g^{-1}	0.0004	B.D.L.	0.0726	0.114	0.0535	0.0797	0.0687	0.0734	0.0715	0.101	51.3	**0.0135	29.6
[Pb]	I-1	ICP-QMS	Sm-IS	μg g^{-1}	0.0001	2.57	3.00	3.57	3.09	3.44	3.07	3.22	3.16	2.90	12.2	1.19	4.5
[Bi]	I-1	ICP-QMS	Sm-IS	μg g^{-1}	0.0008	B.D.L.	0.0530	0.125	0.104	0.144	0.0968	0.0951	0.0958	0.0738	56.2	**0.0272	43.2
[Th]	I-1	ICP-QMS	Sm-IS	μg g^{-1}	0.001	0.0341	0.0346	0.0388	0.0338	0.0491	0.0337	0.0368	0.0355	0.0291	7.6	0.0619	2.1
[U]	I-1	ICP-QMS	Sm-IS	μg g^{-1}	0.0004	0.00923	0.00741	0.0150	0.00660	0.0103	0.00909	0.00877	0.00890	0.00685	25.6	0.0157	9.4

DL = 3σ detection limit, N.A. = not analyzed, B.D.L. = below detection limit, N.D. = not determined, ID = isotope dilution methods, X-IS = internal standardization method using an element X as internal standard, Calc = calculated using Si/Mg ratio by SEM-EDS data and Mg abundance by ICPMS. Values with * were excluded for the weighted mean elemental abundances. **The significant deficiencies in Tl and Bi concentrations in the results of Smithonian Allende could be attributed to sample heterogeneity with small sample digestions (4-7 mg); analyses with samples >10 mg showed that Tl and Bi concentrations were 0.0561 and 0.0446 μg g^{-1} (n=4), respectively, in agreement within 7% of the reference values. The Ru, Pd, Re, Ir, and Pt values in IV-1 are weighted means, except for C0079. C0053_F1 = fraction of C0053 prepared by the ultra-microtome, C0053_F2 = fraction of C0053 prepared by hand-pick and decomposed by using bomb. †TD1, TD2, and Bulk Ryugu denote weighted mean elemental abundances of TD1 particles, TD2 particles, and all particles, respectively. Further details are described in Supplementary Text ST1.4.

Table S13: Abundances of highly siderophile elements and Os isotopic composition of Ryugu particles.

Sample	HF digestion	Weight (g)	[Ru] (μg g^{-1})	[Pd] (μg g^{-1})	[Ir] (μg g^{-1})	[Pt] (μg g^{-1})	[Re] (μg g^{-1})	[Os] (μg g^{-1})	^{187}Re/^{188}Os	2SE	^{187}Os/^{188}Os	2SE
A0022-17	Y	0.000154	0.441	0.391	0.325	0.677	0.0298	0.400	0.357	0.108	-	-
A0022-20	Y	0.000265	0.508	0.454	0.366	0.714	0.0332	-	-	-	-	-
*A0022-21	N	0.000161	0.590	0.519	0.434	0.867	0.0435	0.440	0.477	0.097	0.1258	0.0072
A0022-19	N	0.000205	0.478	0.412	0.323	0.627	0.0294	-	-	-	-	-
*A0033-19	Y	0.000254	0.532	0.511	0.381	0.715	0.0361	0.400	0.435	0.070	0.1256	0.0056
A0033-21	N	0.000276	0.541	0.497	0.367	0.721	0.0320	-	-	-	-	-
*A0048-11	Y	0.000157	0.637	0.558	0.553	0.876	0.0489	0.583	0.404	0.076	0.1243	0.0115
A0048-13	N	0.000232	0.666	0.633	0.484	0.955	0.0414	-	-	-	-	-
C0008-17	Y	0.000250	0.613	0.576	0.433	0.840	0.0387	0.476	0.388	0.060	-	-
C0008-22	Y	0.000216	0.611	0.566	0.438	0.823	0.0395	-	-	-	-	-
*C0008-23	N	0.000177	0.624	0.702	0.435	0.921	0.0484	0.473	0.493	0.084	0.1268	0.0061
C0008-21	N	0.000259	0.622	0.586	0.479	0.867	0.0461	-	-	-	-	-
*C0019-16	Y	0.000164	0.832	1.25	1.08	0.914	0.0593	0.477	0.598	0.092	0.1256	0.0072
C0019-18	N	0.000247	0.729	0.620	0.462	0.943	0.0569	-	-	-	-	-
*C0079-13	Y	0.000139	0.701	0.633	0.481	0.897	0.0386	0.521	0.357	0.093	0.1248	0.0077
				(Pd/Ru)	(Ir/Ru)	(Pt/Ru)		(Os/Ru)				
Fe-sulfide	N	0.000004		0.083	0.42	1.5		0.40			0.3037	0.2449
Bulk Ryugu									0.459		0.1255	
Orgueil	Y	0.000599	0.679	0.505	0.432	0.806	0.0411	0.464	0.427	0.036	0.1264	0.0056
Allende 1	Y	0.00347	0.987	0.655	0.661	1.28	0.0614	0.732	0.399	0.024	0.1265	0.0056
Allende 2	Y	0.00121	1.22	0.828	0.768	1.52	0.0723	0.841	0.436	0.027	0.1262	0.0074
Murchison 1	Y	0.00202	-	-	-	-	0.0341	0.535	0.307	0.020	0.1271	0.0056
Murchison 2	Y	0.00118	-	-	-	-	0.0332	0.537	0.298	0.021	0.1254	0.0055

Fe-sulfide is hand-picked fraction of euhedral pyrrhotites (several tens of μm in size) from the fraction C0019-19; Bulk Ryugu is weighted mean of samples marked with *; Orgueil (CI1) is ultra-microtomed; Allende (CV3) and Murchison (CM2) are powdered samples. Y and N in HF digestion indicate the presence or absence of HF digestion after decomposition by the carious tube. ^{187}Re/^{188}Os and ^{187}Os/^{188}Os and their 2SEs represent blank-corrected values. Fe-sulfide are shown as elemental abundance ratios based on Ru. The Re/Ru ratio could not be determined (N.D.) due to the extremely small sample amount. Details are described in Supplementary Text ST1.4.5.

Table S14: H, C, N, O, Ca, and Cr isotopic compositions of Ryugu fragments.

	δD_{VSMOW}	$\delta^{13}C_{TC}$	$\delta^{13}C_{TOC}$	$\delta^{13}C_{carb}$	2SD	$\delta^{15}N$	$\delta^{17}O$	2SE	$\delta^{18}O$	2SE	$\Delta^{17}O$	2SE	$\epsilon^{48}Ca$	2SE	$\epsilon^{54}Cr$	2SE
A0022	178	14.07	-18.18	42.5	7.6	40.53	11.033	0.018	20.084	0.010	0.506	0.019	1.97	0.33 (3)	1.49	0.16 (8)
A0033	202	-2.44	-18.92	10.9	2.6	17.82	10.227	0.014	18.551	0.007	0.503	0.015	—	—	—	—
A0035	158	-7.07	—	—	—	52.08	—	—	—	—		—	—	—	—	—
A0048	218	-10.25	-16.89	—	—	35.00	—	—	—	—	—	—	—	—	—	—
A0073	—	-9.68	-15.38	—	—	52.34	—	—	—	—	—	—	—	—	—	—
A0078	183	-9.36	-20.48	2.2	2.9	50.94	—	—	—	—	—	—	—	—	—	—
A0085	301	—	—	—	—	—	—	—	—	—	—	—	—	—	—	—
C0008	341	-3.03	-18.16	—	—	46.23	10.136	0.022	18.376	0.011	0.503	0.022	—	—	—	—
C0019	100	-6.26	-18.32	—	—	26.80	10.499	0.020	18.855	0.022	0.615	0.019	—	—	—	—
C0027	123	-7.29	-18.00	—	—	22.66	—	—	—	—	—	—	—	—	—	—
C0039	—	-7.72	-23.09	—	—	—	—	—	—	—	—	—	—	—	—	—
C0047	—	-10.53	-20.26	—	—	—	—	—	—	—	—	—	—	—	—	—
C0053	210	—	—	—	—	—	—	—	—	—	—	—	—	—	—	—
C0079	159	-8.98	-17.93	—	—	22.85	9.843	0.027	17.720	0.013	0.554	0.026	—	—	—	—
C0081	345	-9.78	-15.65	9.5	7.8	53.01	—	—	—	—	—	—	2.21	0.27 (2)	1.77	0.10 (8)
C0082	108	-15.28	-18.41	-11.9	4.2	0.37	—	—	—	—	—	—	—	—	—	—

Remarks: Hydrogen, carbon, nitrogen, and oxygen isotopic compositions are obtained by using IRMS. Calcium and chromium isotopic compositions are obtained by using TIMS. The number of analyses is shown in parenthesis.

Table S15: Ne elemental abundances and isotopic compositions.

Sample no.	Sample mass (mg)	[Ne] (10^{-8} ccSTP · g^{-1})	$^{20}Ne/^{22}Ne$	$^{21}Ne/^{22}Ne$
Ryugu				
TD1				
A0022-2	0.011	75 (8)	10.76 (0.54)	0.1063 (0.0155)
†A0033-13	0.022	21 (3)	7.70 (0.63)	0.1856 (0.0398)
A0033-14	0.029	23 (3)	7.18 (0.33)	0.2191 (0.0240)
A0035-7§	0.025	100 (10)	11.59 (0.31)	0.0478 (0.0035)
A0035-11§	0.011	720 (80)	12.42 (0.43)	0.0343 (0.0020)
A0035-8§	0.023	95 (10)	9.79 (0.35)	0.0486 (0.0038)
A0035-10§	0.067	120 (10)	9.67 (0.31)	0.0455 (0.0028)
A0048-2	0.063	430 (40)	12.28 (0.26)	0.0427 (0.0021)
†A0073-2	0.018	790 (90)	12.08 (0.31)	0.0491 (0.0026)
†A0078-11	0.024	11000 (1200)	13.25 (0.49)	0.0326 (0.0011)
A0085-2	0.122	1370 (140)	13.29 (0.50)	0.0381 (0.0005)
TD2				
†C0008-5§	0.072	77 (8)	10.62 (0.63)	0.0994 (0.0073)
‡C0008-5 (2nd)§	ibid	62 (7)	10.30 (0.26)	0.0959 (0.0067)
C0019-2	0.024	160 (20)	11.75 (0.17)	0.0665 (0.0043)
C0027-2	0.066	82 (9)	10.66 (0.28)	0.0918 (0.0047)
C0039-2	0.012	310 (30)	12.64 (0.23)	0.0473 (0.0050)
C0047-2	0.013	350 (40)	12.57 (0.54)	0.0626 (0.0048)
C0047-3	0.033	150 (20)	11.29 (0.46)	0.0788 (0.0034)
C0053-5	0.025	84 (9)	10.43 (0.48)	0.0905 (0.0095)
C0079-2	0.036	48 (5)	10.95 (0.41)	0.0948 (0.0093)
C0081-6	0.048	40 (4)	9.30 (0.29)	0.1109 (0.0059)
C0082-2	0.015	42 (5)	10.31 (0.57)	0.1094 (0.0166)
Allende				
AL-01	1.07	9.48 (1.02)	2.46 (0.10)	0.7359 (0.0076)
AL-02	1.81	11.1 (1.2)	3.20 (0.12)	0.6581 (0.0135)
AL-03	0.53	13 (1)	3.87 (0.16)	0.5881 (0.0145)
AL-04	1.16	9.56 (1.00)	2.53 (0.10)	0.7068 (0.0174)
AL-05	0.63	8.0 (0.9)	1.90 (0.08)	0.8018 (0.0227)
AL-06	0.743	9.66 (0.67)	2.47 (0.06)	0.7010 (0.0119)
AL-07	0.414	8.95 (0.63)	2.49 (0.07)	0.6831 (0.0167)
Orgueil				
Org 2E-A	0.31	29 (1)	6.71 (0.25)	0.1541 (0.0047)
Org 2E-B	0.46	31 (2)	6.47 (0.37)	0.1849 (0.0035)
∗Org 2E-C	0.42	26 (1)	7.17 (0.40)	0.1449 (0.0034)
Org 2E-1	0.95	59 (3)	8.94 (0.34)	0.1512 (0.0021)
Org 2E-2	0.27	31 (1)	6.46 (0.25)	0.2087 (0.0040)
Org 2E-3	0.32	27 (1)	6.49 (0.15)	0.2420 (0.0083)
Org 2E-4	0.15	30 (2)	6.30 (0.15)	0.2020 (0.0090)
Org 2E-5	0.21	31 (1)	6.69 (0.28)	0.2305 (0.0038)
Org 2E-6	0.37	29 (1)	5.85 (0.22)	0.2163 (0.0038)
Org 2E-7	0.26	160 (10)	10.44 (0.22)	0.0977 (0.0016)
Org 2E-8	0.195	25.6 (1.4)	4.61 (0.09)	0.2233 (0.0050)
Org 2E-9	0.205	120 (6)	10.43 (0.27)	0.1084 (0.0031)
Org 2E-10	0.058	23 (1)	5.90 (0.13)	0.3123 (0.0130)
Org 2E-11	0.207	21.5 (1.1)	5.02 (0.07)	0.4185 (0.0083)
Org 2E-12	0.155	30.3 (1.5)	7.09 (0.17)	0.2532 (0.0086)
Org 2E-13	0.166	29.8 (1.5)	6.48 (0.18)	0.2136 (0.0061)
Org 2E-14	0.121	26.6 (1.3)	6.12 (0.21)	0.2800 (0.0110)

Isotopic compositions of Allende (CV3) and Orgueil (CI1) determined in this study are also shown.

Uncertainties of $^{20}Ne/^{22}Ne$ and $^{21}Ne/^{22}Ne$ in parentheses are within-run deviation of beam current ratios (10 cycles)

†, Trap current 200 μA (others, 400 μA)

‡, Re-analysis of Ne resided in a flight tube

∗, partially fused

§, A0035-8 and A0035-10, light-colored domain; A0035-7 and A0035-11, dark-colored domain

Table S16: Summary of D and G bands fitting result.

Sample	n	D/G ratio	D/G ratio SD	D-band peak pos. (cm^{-1})	D pos. SD	G-band peak pos. (cm^{-1})	G pos. SD	FWHM_G (cm^{-1})	FWHM_G SD	FWHM_D (cm^{-1})	FWHM_D SD
A0022	375	1.38	0.35	1364	8	1583	9	122	27	233	18
A0033	990	1.54	0.14	1358	3	1592	3	113	9	231	11
A0035	289	1.27	0.08	1355	2	1585	2	120	5	223	8
A0048	1213	1.34	0.20	1363	4	1589	3	121	11	237	12
A0073	2077	1.12	0.12	1368	12	1584	2	129	7	232	10
A0078	2574	1.47	0.09	1360	4	1591	4	115	16	235	14
A0085	515	1.47	0.07	1358	3	1592	3	112	15	233	12
C0008	2035	1.34	0.11	1360	4	1590	4	118	14	227	13
C0019	2021	1.23	0.16	1361	6	1591	2	111	5	214	14
C0027	972	1.29	0.29	1365	5	1589	4	113	9	220	15
C0039	1198	1.39	0.15	1362	3	1591	2	117	7	239	12
C0047	3122	1.24	0.26	1367	5	1588	5	123	11	235	15
C0053	5939	1.50	0.14	1359	6	1585	3	115	11	247	15
C0079	795	1.71	0.08	1356	4	1595	3	100	10	233	9
C0081	1285	1.54	0.08	1358	3	1589	4	123	14	248	11
C0082	2398	1.68	0.07	1358	6	1596	3	101	15	232	19
Murchison	359	1.46	0.08	1355	2	1593	1	103	6	206	12
Murray	867	1.31	0.06	1355	2	1595	1	97	4	190	7
Orgueil	435	1.39	0.13	1365	3	1590	2	120	7	227	12

The data for Murchison (CM2), Murray (CM2) and Orgueil (CI1) determined in this study are also shown.

Table S17: The FTIR mode peak center and intensity ratio values for A0035, C0008 and Orgueil (CI1).

Mode Peak Center/Ratio	A0035 Av.	A0035 S.D.	Orgueil Av.	Orgueil S.D.
νC-O	1057.1	6.5	1037.2	0.3
νC-O	1149.7	10.9	1158.8	3.3
Aro. Skel.	1235.0	10.0	1233.8	7.8
βC-H$_{3\text{ Sym.}}$	1369.3	17.1	1381.0	11.0
βC-H$_{3\text{ Asym.}}$	1453.4	2.1	1455.0	1.5
νC=C$_{\text{Aro.}}$	1608.7	3.6	1605.3	1.5
νC=O	1715.8	0.8	1712.8	1.8
νC-H$_{2\text{ Sym.}}$	2869.2	5.3	2853.8	0.4
νC-H$_{3\text{ Sym.}}$			2872.1	0.7
νC-H$_{\text{Ali.}}$	2904.5	2.0	2905.7	5.2
νC-H$_{2\text{ Asym.}}$	2929.5	2.4	2926.8	1.7
νC-H$_{3\text{ Asym.}}$	2961.8	3.2	2961.7	0.2
CH$_2$/CH$_{3\text{ Asym.}}$	0.77	0.24	1.17	0.13
Aliphatics/C=C	0.40	0.12	0.49	0.20
Aliphatics/C=O	0.42	0.13	0.51	0.18
C=O/C=C	0.96	0.08	0.94	0.10

Av. = average, S.D. = standard deviation, Aro. = aromatic, Skel. = skeletal, ν = stretching vibration, β = bending vibration, Sym. = symmetric, Asym. = asymmetric and Ali = aliphatic. Note that aliphatics refers to the sum of the CH$_x$ band intensities, where the asymmetric stretch of the CH$_2$ and CH$_3$ modes was used for the calculation.

Table S18: Information concerning the organic compounds detected in C0008-15 and A0048-10 (indicated by*) by DESI-OT-MS.

Gen. Formula	C#	Formula	Mass	[M+H]	Gen. Formula	C#	Formula	Mass	[M+H]	[M+Na]
$CnH_{2n-5}N$	n=10	$C_{10}H_{15}N$	149.120998	150.128275	$CnH_{2n-17}N$	n=20	$C_{20}H_{23}N$	277.183050	278.190326	-
	n=11	$C_{11}H_{17}N$	163.136648	164.143925		n=21	$C_{21}H_{25}N$	291.198700	292.205976	-
	n=12	$C_{12}H_{19}N$	177.152298	178.159575		n=22	$C_{22}H_{27}N$	305.214350	306.221626	-
	n=13*	$C_{13}H_{21}N$	191.167948	192.175225		n=23	$C_{23}H_{29}N$	319.230000	320.237277	-
	n=14*	$C_{14}H_{23}N$	205.183598	206.190875		n=24	$C_{24}H_{31}N$	333.245650	334.252927	-
	n=15*	$C_{15}H_{25}N$	219.198700	220.205976		n=25	$C_{25}H_{33}N$	347.261300	348.268577	-
	n=16*	$C_{16}H_{27}N$	233.214350	234.221626		n=26	$C_{26}H_{35}N$	361.276950	362.284227	-
	n=17*	$C_{17}H_{29}N$	247.230000	248.237277						
	n=18*	$C_{18}H_{31}N$	261.245650	262.252927	$CnH_{2n-9}N$	n=15*	$C_{15}H_{21}N$	215.167400	216.174676	-
	n=19	$C_{19}H_{33}N$	276.269125	276.268577		n=16*	$C_{16}H_{23}N$	229.183050	230.190326	-
						n=17*	$C_{17}H_{25}N$	243.198700	244.205976	-
$CnH_{2n-11}N$	n=15	$C_{15}H_{19}N$	213.151750	214.159026		n=18*	$C_{18}H_{27}N$	257.214350	258.221626	-
	n=16*	$C_{16}H_{21}N$	227.167400	228.174676		n=19*	$C_{19}H_{29}N$	271.230000	272.237277	-
	n=17*	$C_{17}H_{23}N$	241.183050	242.190326		n=20*	$C_{20}H_{31}N$	285.245650	286.252927	-
	n=18*	$C_{18}H_{25}N$	255.198700	256.205976		n=21*	$C_{21}H_{33}N$	299.261300	300.268577	-
	n=19*	$C_{19}H_{27}N$	269.214350	270.221626		n=22	$C_{22}H_{35}N$	313.276950	314.284227	-
	n=20*	$C_{20}H_{29}N$	283.230000	284.237277		n=23	$C_{23}H_{37}N$	327.292600	328.299877	-
	n=21	$C_{21}H_{31}N$	297.245650	298.252927		n=24	$C_{24}H_{39}N$	341.308250	342.315527	-
	n=22	$C_{22}H_{33}N$	311.261300	312.268577						
	n=23	$C_{23}H_{35}N$	325.276950	326.284227	$CnH_{2n-13}N$	n=15	$C_{15}H_{17}N$	211.136100	212.143376	-
	n=24	$C_{24}H_{37}N$	339.292600	340.299877		n=16	$C_{16}H_{19}N$	225.151750	226.159026	-
						n=17	$C_{17}H_{21}N$	239.167400	240.174676	-
$CnH_{2n-15}N$	n=18	$C_{18}H_{21}N$	251.167400	252.174676		n=18	$C_{18}H_{23}N$	253.183050	254.190326	-
	n=19*	$C_{19}H_{23}N$	265.183050	266.190326		n=19	$C_{19}H_{25}N$	267.198700	268.205976	-
	n=20*	$C_{20}H_{25}N$	279.198700	280.205976		n=20	$C_{20}H_{27}N$	281.214350	282.221626	-
	n=21*	$C_{21}H_{27}N$	293.214350	294.221626		n=21	$C_{21}H_{29}N$	295.230000	296.237277	-
	n=22*	$C_{22}H_{29}N$	307.230000	308.237277		n=22	$C_{22}H_{31}N$	309.245650	310.252927	-
	n=23	$C_{23}H_{31}N$	321.245650	322.252927		n=23	$C_{23}H_{33}N$	323.261300	324.268577	-
	n=24	$C_{24}H_{33}N$	335.261300	336.268577		n=24	$C_{24}H_{35}N$	337.276950	338.284227	-
	n=25	$C_{25}H_{35}N$	349.276950	350.284227						
	n=26	$C_{26}H_{37}N$	363.292600	364.299877	Other compounds					
							$C_6H_{11}ON$	113.084064	114.091341	136.073285
$CnH_{2n-7}N$	n=13	$C_{13}H_{19}N$	189.151750	190.159026			$C_5H_{11}N$	85.089149	86.096426	-
	n=14*	$C_{14}H_{21}N$	203.167400	204.174676			$C_5H_{12}N_2O$	116.094963	-	139.084184
	n=15*	$C_{15}H_{23}N$	217.183050	218.190326			$C_9H_{14}O$	138.104465	-	161.093686
	n=16*	$C_{16}H_{25}N$	231.198700	232.205976			$C_2H_3ClOS_2$	-	-	164.920490
	n=17*	$C_{17}H_{27}N$	245.214350	246.221626			$C_9H_{23}N_4P$	218.166033	219.173310	-
	n=18*	$C_{18}H_{29}N$	259.230000	260.237277			$C_5H_6N_2SBr_2$†	218.166033	219.173310	-
	n=19*	$C_{19}H_{31}N$	273.245650	274.252927						
	n=20*	$C_{20}H_{33}N$	287.261300	288.268577						
	n=21	$C_{21}H_{35}N$	301.276950	302.284227						
	n=22	$C_{22}H_{37}N$	315.292600	316.299877						

Chemical formulas were determined from the masses and most ions were found to be H adducts, but for some compounds, which were not part of the homologue series, Na adducts were instead recorded. C# = carbon number, Gen. = general, [M+H] = molecule + 1 hydrogen ion, [M+Na] = molecule + 1 sodium ion. The masses given in the table are the calculated masses for the detected ions, with the detected values all within a mass range of 2.5 ppm of the calculated values. †Note that $C_5H_6N_2SBr_2$ only gave a response for A0048-10.

Table S19: The organic compounds detected in Orgueil (CI1) by DESI-OT-MS.

Name/Gen. Formula	C#	Formula	Mass	[M+H]	[M+Na]
$C_nH_{2n-13}N$	n=16	$C_{16}H_{25}N$	231.198700	232.205976	-
	n=17	$C_{17}H_{27}N$	245.214350	246.221626	-
	n=18	$C_{18}H_{29}N$	259.230000	260.237277	-
	n=19	$C_{19}H_{31}N$	273.245650	274.252927	-
					-
		Other compounds			
		$C_5H_{11}N$	85.089149	86.096426	-
		$C_5H_{12}N_2O$	116.094963	-	139.084184
		$C_2H_3C_lOS_2$	-	-	164.920490
		$C_4H_4O_3N_2S_2$	191.966333	-	214.955555
		$C_9H_{11}N_2O_4P$	242.045643	243.052920	-
		$C_2H_5ON_2$	96.029957	-	119.019179
		$C_2H_8O_4N$	110.045333	-	133.034554
		$C_4H_{14}O_3N_3$	152.103516	-	175.092738
		$C_4H_2O_2N_2S_2$	173.955769	-	196.944990
		$C_{16}H_9O_4N_3$	307.059306	308.066582	-
		$C_5H_6N_2SBr_2$	283.861844	-	306.851065

Chemical formulas were determined from the masses and most ions were found to be H adducts, but for some compounds, which were not part of the homologue series, Na adducts were instead recorded. C# = carbon number, Gen. = general, [M+H] = molecule + 1 hydrogen ion, [M+Na] = molecule + 1 sodium ion. The masses given in the table are the calculated masses for the detected ions, with the detected values all within a mass range of 2.5 ppm of the calculated values.

Table S20: The organic compounds detected by HPLC-OT-MS.

					C0008			Orgueil		
C#	Compound	Code	Mass [M+H]	RT (Std.)	RT	FM	Intensity	RT	FM	Intensity
1	*Urea	Ure	61.0396	8.50	8.56	-	1.88E+04	8.83	-	5.93E+04
2	Glycine	Gly	118.0863	13.63	13.54	-	1.80E+05	13.55	Y	4.82E+05
3	Sarcosine + Alanine	Sar+Ala	132.1019	13.29	13.14	Y	2.46E+05	13.12	Y	1.17E+06
3	β-Alanine	β-Ala	132.1019	14.52	14.40	Y	5.29E+05	14.48	Y	1.94E+06
3	Serine	Ser	148.0968	14.46	14.34	-	1.63E+04	14.40	Y	2.77E+05
4	Threonine	Thr	162.1125	13.01	13.18	-	5.82E+03	13.24	Y	1.97E+05
4	α-Aminobutyric Acid	α-Ab	146.1176	12.21	12.10	-	3.10E+04	12.15	Y	2.00E+05
4	α-Aminoisobutyric Acid	α-Aib	146.1176	13.06	12.98	-	9.23E+04	12.96	Y	2.30E+05
4	β-Aminobutyric + β-Aminoisobutyric Acid	β-Ab+β-Aib	146.1176	14.01	13.88	Y	3.89E+05	13.95	Y	1.43E+06
4	DL-Aspartic Acid	Asp	218.1387	4.39	4.35	Y	6.27E+05	4.40	Y	4.30E+06
5	L-Valine	Val	160.1332	10.20	10.24	-	2.74E+04	10.17	Y	2.47E+06
5	Norvaline	Nov	160.1332	11.66	11.58	Y	2.61E+04	11.65	Y	3.24E+05
5	Glutamic Acid	Glu	232.1543	6.33	6.42	Y	5.51E+05	6.32	Y	1.23E+07
5	*Proline	Pro	158.1176	13.30	13.35	Y	8.70E+04	13.39	Y	1.91E+06
5	*Hydroxyproline	Hpr	174.1125	14.20	14.17	-	9.44E+03	14.34	Y	2.05E+04
6	Leucine	leu	174.1489	10.69	10.71	Y	3.36E+04	10.68	Y	4.08E+06
6	Isoleucine	Ile	174.1489	10.52	10.55	-	1.14E+04	10.50	Y	2.60E+06
6	Alloleucine	Ale	174.1489	9.14	9.24	-	6.47E+03	9.12	Y	1.03E+05
6	α-Aminoadipic Acid	α-Adp	246.1700	10.04	10.01	Y	5.14E+04	10.00	Y	3.63E+05
6	Cycloleucine	Cle	172.1332	12.82	12.71	-	3.64E+04	12.69	Y	7.02E+04
6	Pipecolic Acid	Pip	172.1332	13.35	13.23	-	2.96E+04	13.22	Y	9.48E+04
6	Aminocaproic Acid	Aca	174.1489	13.94	13.79	Y	4.78E+05	13.95	Y	7.64E+05
7	α-Aminopimelic Acid	α-Apm	260.1856	10.69	10.70	-	7.86E+03	10.78	-	1.15E+04
7	Homocycloleucine	Hcl	186.1489	11.00	10.97	-	4.34E+03	10.72	-	7.68E+03
9	Phenylalanine	Pha	208.1332	5.62	5.68	Y	2.71E+04	5.68	Y	2.19E+06
9	Tyrosine	Tyr	224.1281	11.30	ND	ND	1.00E+00	11.28	Y	5.12E+05

Extracted ion chromatograms (EIC) were produced from the TIC and peaks were matched against those obtained for several standards. A custom standard consisting of the majority of the amino acids detected here was prepared and run after the C0008-18 and Orgueil (CI1) samples. Data for another standard, AN-2 standard run previously, was compared with the sample EICs to detect further amino acids (those denoted with an *). C# = carbon number, Code = the shorthand used to identify the amino acid in text and in other figures, RT = retention time and FM = fragmentation pattern match. Fragmentation patterns for tandem mass spectrometry (MS^2) were compared between the standards and samples. If a fragmentation pattern was obtained for the sample and it matched that in the standard, then a Y is recorded in the FM section. If no fragmentation pattern was recorded, then a – is recorded in the FM section. There were no cases where a fragmentation pattern was recorded that did not match the standard.

Table S21: The absolute intensity ratios for amino acid isomers detected in C0008 and Orgueil (CI1) by UHPLC-OT-MS.

	Intensity Ratio	
Ratio	C0008	Orgueil
Sarcosine + Alanine/β-Alanine	0.46	0.60
α-Aminobutyric Acid/α-Aminoisobutyric Acid	0.34	0.87
β-Aminobutyric + β-Aminoisobutyric Acid/α-Aminobutyric Acid	12.56	7.18
β-Aminobutyric + β-Aminoisobutyric Acid/α-Aminoisobutyric Acid	4.22	6.22
Valine/Norvaline	1.05	7.62
Leucine/Isoleucine	2.94	1.57
Alloleucine/Leucine	0.19	0.03
Alloleucine/Isoleucine	0.57	0.04

Table S22: Parameters to deconvolve bulk Ne into cosmogenic Ne, trapped Ne, and solar-wind Ne.

Shielding depth ($g \cdot cm^{-2}$)	Cosmic-ray species	$P(^{21}Ne_{cos})$ $[10^{-8}$ ccSTP $\cdot (g \cdot Myr)^{-1}]$	$(^{20}Ne/^{22}Ne)_{cos}$	$(^{21}Ne/^{22}Ne)_{cos}$	$(^{20}Ne/^{22}Ne)_{trap}$	$(^{21}Ne/^{22}Ne)_{trap}$	$(^{20}Ne/^{22}Ne)_{SW}$	$(^{21}Ne/^{22}Ne)_{SW}$
0–1.5 (Option 1)	GCR + SCR	0.200 ± 0.008	2.3†	0.707 ± 0.005	8.9	0.029	13.78 ± 0.03	0.0329 ± 0.0001
1.5–5 (Option 2)	GCR + SCR	0.133 ± 0.008	1.0†	0.841 ± 0.004	8.9	0.029	13.78 ± 0.03	0.0329 ± 0.0001
5–10 (Option 3)	GCR + SCR	0.130 ± 0.008	0.9†	0.900 ± 0.003	8.5	0.029	13.78 ± 0.03	0.0329 ± 0.0001
10–15 (Option 4)	GCR + SCR	0.137 ± 0.009	0.9†	0.927 ± 0.003	8.5	0.029	13.78 ± 0.03	0.0329 ± 0.0001
15–20 (Option 5)	GCR	0.133 ± 0.009	0.723 ± 0.004	0.953 ± 0.003	8.5	0.029	13.78 ± 0.03	0.0329 ± 0.0001
45–50 (Option 6)	GCR	0.150 ± 0.010	0.725 ± 0.004	0.976 ± 0.004	8.5	0.029	13.78 ± 0.03	0.0329 ± 0.0001
100–120 (Option 7)	GCR	0.133 ± 0.009	0.740 ± 0.004	1.007 ± 0.004	8.5	0.029	13.78 ± 0.03	0.0329 ± 0.0001
250–270 (Option 8)	GCR	0.0658 ± 0.0046	0.730 ± 0.005	1.003 ± 0.004	8.5	0.029	13.78 ± 0.03	0.0329 ± 0.0001

Cosmic-ray species: GCR, galactic cosmic ray; SCR, solar cosmic ray

$P(^{21}Ne)$ denotes the production rate of cosmogenic ^{21}Ne.

$(^{20}Ne/^{22}Ne)_{cos}$ and $(^{21}Ne/^{22}Ne)_{cos}$ denote $^{20}Ne/^{22}Ne$ and $^{21}Ne/^{22}Ne$ ratios of a cosmogenic Ne.

$(^{20}Ne/^{22}Ne)_{trap}$ and $(^{21}Ne/^{22}Ne)_{trap}$ denote $^{20}Ne/^{22}Ne$ and $^{21}Ne/^{22}Ne$ ratios of a trapped Ne.

$(^{20}Ne/^{22}Ne)_{SW}$ and $(^{21}Ne/^{22}Ne)_{SW}$ denote $^{20}Ne/^{22}Ne$ and $^{21}Ne/^{22}Ne$ ratios of the solar-wind Ne.

Table S23: The Ne abundances of solar wind, cosmogenic, and trapped components in the TD1 samples.

Option	Sample	A0022-2	A0033-12	A0033-13	A0033-14	A0035-7	A0035-11	A0035-8	A0035-10	A0048-2	A0073-2	A0078-11	A0085-2
1	$[\mathrm{Ne}]_{\mathrm{SW}}$	49.6		2.35	1.07	68.1	578	28.5	31.5	339	613	10178	1294
	$1\sigma_{\mathrm{m}}$	12.2		5.31	3.41	10.6	95	9.9	11.0	43	88	1592	203
	$[\mathrm{Ne}]_{\mathrm{cos}}$	2.80		2.20	3.12	0.772	0.783	0.973	1.05	2.06	6.20	0.56	3.15
	$1\sigma_{\mathrm{m}}$	0.66		0.63	0.53	0.184	0.646	0.224	0.22	0.44	1.16	5.10	0.49
	$[\mathrm{Ne}]_{\mathrm{trap}}$	22.4		16.6	19.1	30.7	145	65.9	87.7	85.6	172	824	76.6
	$1\sigma_{\mathrm{m}}$	8.1		5.0	3.7	6.1	49	9.8	12.0	19.0	42	756	96.5
2	$[\mathrm{Ne}]_{\mathrm{SW}}$	49.6		2.35	1.06	68.1	578	28.5	31.5	339	613	10178	1294
	$1\sigma_{\mathrm{m}}$	12.2		5.31	3.41	10.6	95	9.9	11.0	43	88	1592	203
	$[\mathrm{Ne}]_{\mathrm{cos}}$	1.66		1.30	1.85	0.457	0.463	0.576	0.620	1.22	3.67	0.332	1.86
	$1\sigma_{\mathrm{m}}$	0.39		0.37	0.31	0.109	0.382	0.133	0.129	0.26	0.69	3.017	0.29
	$[\mathrm{Ne}]_{\mathrm{trap}}$	23.5		17.5	20.4	31.0	145	66.3	88.1	86.4	175	825	77.9
	$1\sigma_{\mathrm{m}}$	8.0		4.9	3.7	6.1	49	9.8	12.0	19.0	43	757	96.6
3	$[\mathrm{Ne}]_{\mathrm{SW}}$	51.6		3.78	2.60	71.4	594	35.7	41.2	348	631	10271	1302
	$1\sigma_{\mathrm{m}}$	11.5		4.80	3.07	10.5	92	9.5	10.7	43	87	1542	197
	$[\mathrm{Ne}]_{\mathrm{cos}}$	1.52		1.19	1.69	0.417	0.412	0.523	0.561	1.11	3.36	0.23	1.70
	$1\sigma_{\mathrm{m}}$	0.36		0.34	0.29	0.100	0.351	0.122	0.118	0.24	0.63	2.75	0.26
	$[\mathrm{Ne}]_{\mathrm{trap}}$	21.7		16.2	19.0	27.8	129	59.1	78.6	77.3	157	732	70.1
	$1\sigma_{\mathrm{m}}$	7.1		4.3	3.3	5.4	43	8.7	10.7	16.9	38	672	85.8
4	$[\mathrm{Ne}]_{\mathrm{SW}}$	51.2		3.51	2.22	71.3	594	35.6	41.0	348	630	10271	1302
	$1\sigma_{\mathrm{m}}$	11.5		4.76	3.04	10.5	92	9.5	10.7	43	87	1542	197
	$[\mathrm{Ne}]_{\mathrm{cos}}$	1.49		1.17	1.66	0.409	0.404	0.512	0.550	1.09	3.29	0.22	1.67
	$1\sigma_{\mathrm{m}}$	0.35		0.34	0.28	0.098	0.344	0.119	0.116	0.24	0.62	2.70	0.26
	$[\mathrm{Ne}]_{\mathrm{trap}}$	22.1		16.5	19.4	27.9	129	59.3	78.7	77.6	158	732	70.5
	$1\sigma_{\mathrm{m}}$	7.1		4.3	3.3	5.4	44	8.7	10.7	16.9	38	673	85.9
5	$[\mathrm{Ne}]_{\mathrm{SW}}$	51.2		3.46	2.15	71.3	594	35.6	41.0	348	630	10271	1302
	$1\sigma_{\mathrm{m}}$	11.5		4.75	3.03	10.5	92	9.5	10.7	43	87	1542	197
	$[\mathrm{Ne}]_{\mathrm{cos}}$	1.37		1.08	1.53	0.376	0.371	0.471	0.506	1.00	3.02	0.20	1.54
	$1\sigma_{\mathrm{m}}$	0.33		0.31	0.26	0.090	0.316	0.110	0.106	0.22	0.57	2.48	0.24
	$[\mathrm{Ne}]_{\mathrm{trap}}$	22.3		16.6	19.6	27.9	129	59.3	78.8	77.7	158	732	70.7
	$1\sigma_{\mathrm{m}}$	7.1		4.3	3.3	5.4	44	8.7	10.7	16.9	38	673	85.9
6	$[\mathrm{Ne}]_{\mathrm{SW}}$	50.9		3.25	1.85	71.2	594	35.5	40.9	348	629	10271	1301
	$1\sigma_{\mathrm{m}}$	11.5		4.73	3.01	10.5	92	9.5	10.7	43	87	1542	197
	$[\mathrm{Ne}]_{\mathrm{cos}}$	1.35		1.06	1.50	0.370	0.366	0.464	0.498	0.987	2.98	0.20	1.51
	$1\sigma_{\mathrm{m}}$	0.32		0.31	0.26	0.089	0.311	0.108	0.105	0.213	0.56	2.44	0.23
	$[\mathrm{Ne}]_{\mathrm{trap}}$	22.6		16.8	20.0	28.0	129	59.4	78.9	77.9	159	732	71.0
	$1\sigma_{\mathrm{m}}$	7.1		4.3	3.3	5.4	44	8.7	10.7	16.9	38	673	85.9
7	$[\mathrm{Ne}]_{\mathrm{SW}}$	50.5		2.96	1.44	71.1	594	35.4	40.8	348	628	10271	1301
	$1\sigma_{\mathrm{m}}$	11.4		4.69	2.98	10.5	92	9.5	10.7	43	87	1542	197
	$[\mathrm{Ne}]_{\mathrm{cos}}$	1.33		1.04	1.48	0.365	0.360	0.457	0.491	0.973	2.93	0.198	1.49
	$1\sigma_{\mathrm{m}}$	0.32		0.30	0.25	0.088	0.307	0.106	0.103	0.210	0.55	2.406	0.23
	$[\mathrm{Ne}]_{\mathrm{trap}}$	22.9		17.1	20.4	28.1	129	59.6	79.0	78.2	159	732	71.5
	$1\sigma_{\mathrm{m}}$	7.1		4.2	3.3	5.4	44	8.7	10.8	16.9	38	673	85.9
8	$[\mathrm{Ne}]_{\mathrm{SW}}$	50.6		3.01	1.50	71.2	594	35.4	40.8	348	629	10271	1301
	$1\sigma_{\mathrm{m}}$	11.5		4.70	2.99	10.5	92	9.5	10.7	43	87	1542	197
	$[\mathrm{Ne}]_{\mathrm{cos}}$	1.33		1.04	1.48	0.364	0.360	0.457	0.490	0.972	2.93	0.20	1.49
	$1\sigma_{\mathrm{m}}$	0.32		0.30	0.25	0.088	0.306	0.106	0.103	0.210	0.55	2.40	0.23
	$[\mathrm{Ne}]_{\mathrm{trap}}$	22.9		17.1	20.3	28.1	129	59.5	79.0	78.2	159	732	71.4
	$1\sigma_{\mathrm{m}}$	7.1		4.2	3.3	5.4	44	8.7	10.8	16.9	38	673	85.9

†Options of shielding depth assumed for deconvolution are found in Table S22. $[\mathrm{Ne}]_{\mathrm{SW}}$, $[\mathrm{Ne}]_{\mathrm{cos}}$ and $[\mathrm{Ne}]_{\mathrm{trap}}$ in 10^{-8} ccSTP $\cdot$ g^{-1}

Table S24: The Ne abundances of solar wind, cosmogenic, and trapped components in the TD2 samples.

Option	Sample	C0008-5	C0008-5 (2nd)	C0019-2	C0027-2	C0039-2	C0047-2	C0047-3	C0053-5	C0079-2	C0081-6	C0082-2
1	$[\mathrm{Ne}]_{\mathrm{SW}}$	47.8	33.9	122	50.0	265	313	103	46.4	32.4	13.9	24.4
	$1\sigma_{\mathrm{m}}$	13.9	5.7	15	8.1	33	55	20	11.9	6.2	3.7	7.2
	$[\mathrm{Ne}]_{\mathrm{cos}}$	2.68	2.11	2.60	2.52	2.01	4.67	3.35	2.56	1.51	1.85	1.72
	$1\sigma_{\mathrm{m}}$	0.43	0.31	0.42	0.34	0.69	0.91	0.44	0.50	0.28	0.25	0.42
	$[\mathrm{Ne}]_{\mathrm{trap}}$	26.9	26.4	36.7	29.8	40.0	36.6	41.0	34.3	14.3	24.4	16.1
	$1\sigma_{\mathrm{m}}$	9.1	4.2	6.1	5.2	11.9	28.7	12.1	8.3	3.9	3.6	5.1
2	$[\mathrm{Ne}]_{\mathrm{SW}}$	47.8	33.9	122	50.0	265	313	103	46.4	32.4	13.9	24.4
	$1\sigma_{\mathrm{m}}$	13.9	5.7	15	8.1	33	55	20	11.9	6.2	3.7	7.2
	$[\mathrm{Ne}]_{\mathrm{cos}}$	1.58	1.25	1.54	1.49	1.19	2.77	1.98	1.51	0.89	1.09	1.02
	$1\sigma_{\mathrm{m}}$	0.26	0.19	0.25	0.20	0.41	0.54	0.26	0.29	0.16	0.15	0.25
	$[\mathrm{Ne}]_{\mathrm{trap}}$	28.0	27.3	37.7	30.8	40.8	38.5	42.4	35.3	14.9	25.2	16.8
	$1\sigma_{\mathrm{m}}$	9.2	4.3	6.2	5.3	11.9	28.7	12.1	8.4	3.9	3.7	5.1
3	$[\mathrm{Ne}]_{\mathrm{SW}}$	50.3	36.4	126	52.8	269	316	107	49.8	33.7	16.3	25.9
	$1\sigma_{\mathrm{m}}$	13.2	5.7	15	8.0	33	53	20	11.4	6.0	3.6	6.8
	$[\mathrm{Ne}]_{\mathrm{cos}}$	1.45	1.15	1.41	1.37	1.09	2.54	1.82	1.39	0.818	1.00	0.934
	$1\sigma_{\mathrm{m}}$	0.23	0.17	0.23	0.18	0.38	0.49	0.24	0.27	0.151	0.13	0.227
	$[\mathrm{Ne}]_{\mathrm{trap}}$	25.7	24.8	34.2	28.1	36.8	35.5	38.6	32.1	13.7	22.9	15.4
	$1\sigma_{\mathrm{m}}$	8.2	3.8	5.5	4.7	10.5	25.5	10.8	7.4	3.4	3.3	4.5
4	$[\mathrm{Ne}]_{\mathrm{SW}}$	50.0	36.2	125	52.5	268	316	107	49.5	33.5	16.0	25.7
	$1\sigma_{\mathrm{m}}$	13.2	5.6	15	8.0	33	53	20	11.3	6.0	3.6	6.8
	$[\mathrm{Ne}]_{\mathrm{cos}}$	1.42	1.12	1.38	1.34	1.07	2.49	1.78	1.36	0.801	0.982	0.915
	$1\sigma_{\mathrm{m}}$	0.23	0.17	0.22	0.18	0.37	0.48	0.24	0.27	0.148	0.131	0.223
	$[\mathrm{Ne}]_{\mathrm{trap}}$	26.0	25.1	34.6	28.4	37.1	36.2	39.0	32.5	13.9	23.1	15.6
	$1\sigma_{\mathrm{m}}$	8.2	3.8	5.5	4.8	10.5	25.5	10.8	7.4	3.4	3.3	4.5
5	$[\mathrm{Ne}]_{\mathrm{SW}}$	49.9	36.1	125	52.4	268	315	107	49.4	33.5	16.0	25.7
	$1\sigma_{\mathrm{m}}$	13.2	5.6	15	8.0	33	53	20	11.3	6.0	3.6	6.8
	$[\mathrm{Ne}]_{\mathrm{cos}}$	1.31	1.03	1.27	1.23	0.981	2.29	1.64	1.25	0.737	0.904	0.841
	$1\sigma_{\mathrm{m}}$	0.21	0.15	0.21	0.17	0.341	0.44	0.22	0.24	0.136	0.120	0.205
	$[\mathrm{Ne}]_{\mathrm{trap}}$	26.2	25.3	34.8	28.6	37.2	36.5	39.3	32.6	14.0	23.3	15.8
	$1\sigma_{\mathrm{m}}$	8.2	3.8	5.5	4.8	10.5	25.5	10.9	7.4	3.4	3.3	4.5
6	$[\mathrm{Ne}]_{\mathrm{SW}}$	49.7	35.9	125	52.2	268	315	106	49.2	33.3	15.8	25.5
	$1\sigma_{\mathrm{m}}$	13.1	5.6	15	7.9	33	53	20	11.3	6.0	3.6	6.8
	$[\mathrm{Ne}]_{\mathrm{cos}}$	1.29	1.02	1.25	1.21	0.966	2.25	1.62	1.23	0.726	0.890	0.829
	$1\sigma_{\mathrm{m}}$	0.21	0.15	0.20	0.16	0.336	0.44	0.21	0.24	0.134	0.119	0.202
	$[\mathrm{Ne}]_{\mathrm{trap}}$	26.5	25.5	35.0	28.8	37.4	37.0	39.6	32.9	14.1	23.5	15.9
	$1\sigma_{\mathrm{m}}$	8.2	3.9	5.5	4.8	10.5	25.5	10.9	7.5	3.4	3.3	4.5
7	$[\mathrm{Ne}]_{\mathrm{SW}}$	49.3	35.7	125	51.9	268	314	106	48.8	33.1	15.6	25.3
	$1\sigma_{\mathrm{m}}$	13.1	5.6	15	7.9	33	53	19	11.3	5.9	3.6	6.8
	$[\mathrm{Ne}]_{\mathrm{cos}}$	1.27	1.00	1.23	1.20	0.951	2.22	1.59	1.21	0.715	0.877	0.816
	$1\sigma_{\mathrm{m}}$	0.20	0.15	0.20	0.16	0.331	0.43	0.21	0.24	0.132	0.117	0.199
	$[\mathrm{Ne}]_{\mathrm{trap}}$	26.8	25.8	35.4	29.2	37.7	37.6	40.1	33.2	14.3	23.7	16.2
	$1\sigma_{\mathrm{m}}$	8.2	3.9	5.6	4.8	10.5	25.5	10.9	7.5	3.4	3.4	4.5
8	$[\mathrm{Ne}]_{\mathrm{SW}}$	49.4	35.7	125	51.9	268	315	106	49	33.1	15.6	25.3
	$1\sigma_{\mathrm{m}}$	13.1	5.6	15	7.9	33	53	19	11	5.9	3.6	6.8
	$[\mathrm{Ne}]_{\mathrm{cos}}$	1.27	1.00	1.23	1.19	0.950	2.22	1.59	1.21	0.714	0.875	0.816
	$1\sigma_{\mathrm{m}}$	0.20	0.15	0.20	0.16	0.330	0.43	0.21	0.24	0.132	0.117	0.198
	$[\mathrm{Ne}]_{\mathrm{trap}}$	26.8	25.7	35.3	29.1	37.7	37.5	40.0	33.2	14.3	23.7	16.1
	$1\sigma_{\mathrm{m}}$	8.2	3.9	5.6	4.8	10.5	25.5	10.9	7.5	3.4	3.3	4.5

†Options of shielding depth assumed for deconvolution are found in Table S22. $[\mathrm{Ne}]_{\mathrm{SW}}$, $[\mathrm{Ne}]_{\mathrm{cos}}$ and $[\mathrm{Ne}]_{\mathrm{trap}}$ in 10^{-8} ccSTP · g^{-1}

Table S25: The Ne abundances of the solar-wind component, cosmogenic component, and trapped component.

Sample	$[\mathrm{Ne}]_{\mathrm{SW}}$ (10^{-8} ccSTP $\cdot$ g^{-1})	$[\mathrm{Ne}]_{\mathrm{cos}}$ (10^{-8} ccSTP $\cdot$ g^{-1})	$[\mathrm{Ne}]_{\mathrm{trap}}$ (10^{-8} ccSTP $\cdot$ g^{-1})	f_{SW} (%)	f_{cos} (%)	f_{trap} (%)
TD1						
A0022-2	51 (12)	1.61 (0.38)	22.5 (7.3)	68	2.1	30
A0033-12						
A0033-13	3.1 (4.9)	1.26 (0.36)	16.8 (4.4)	15	6.0	79
A0033-14	1.7 (3.1)	1.79 (0.30)	19.8 (3.4)	7	7.7	85
A0035-7	70 (11)	0.44 (0.11)	28.7 (5.6)	71	0.44	29
A0035-11	590 (93)	0.44 (0.37)	133 (45)	82	0.061	18
A0035-8	34 (10)	0.55 (0.13)	61.1 (9.0)	35	0.58	64
A0035-10	39 (11)	0.60 (0.12)	81 (11)	32	0.50	67
A0048-2	346 (43)	1.18 (0.25)	80 (17)	81	0.28	19
A0073-2	625 (88)	3.55 (0.67)	162 (39)	79	0.45	20
A0078-11	10200 (1600)	0.3 (2.9)	760 (690)	93	0.002	6.9
A0085-2	1300 (200)	1.80 (0.28)	72 (89)	95	0.13	5.3
TD2						
C0008-5	49 (13)	1.53 (0.25)	26.6 (8.4)	64	2.0	34
C0008-5 (2nd)	35.5 (5.7)	1.21 (0.18)	25.8 (4.0)	57	1.9	41
C0019-2	124 (15)	1.49 (0.24)	35.5 (5.7)	77	0.92	22
C0027-2	51.7 (8.0)	1.44 (0.19)	29.1 (4.9)	63	1.8	35
C0039-2	267 (33)	1.15 (0.40)	38 (11)	87	0.4	12
C0047-2	315 (53)	2.68 (0.52)	37 (26)	89	0.76	10
C0047-3	106 (20)	1.92 (0.26)	40 (11)	72	1.3	27
C0053-5	49 (11)	1.47 (0.29)	33.3 (7.7)	58	1.8	40
C0079-2	33.1 (6.0)	0.86 (0.16)	14.2 (3.5)	69	1.8	29
C0081-6	15.4 (3.6)	1.06 (0.14)	23.7 (3.4)	38	2.6	59
C0082-2	25.3 (6.9)	0.99 (0.24)	16.0 (4.7)	60	2.3	38

The $[\mathrm{Ne}]_{\mathrm{SW}}$, $[\mathrm{Ne}]_{\mathrm{cos}}$ and $[\mathrm{Ne}]_{\mathrm{trap}}$ denote Ne abundances of the solar-wind component, cosmogenic component, and trapped component, respectively.

The f_{SW}, f_{cos} and f_{trap} denote relative abundances from each component expressed as

$f_{\mathrm{SW}} = [\mathrm{Ne}]_{\mathrm{SW}}/([\mathrm{Ne}]_{\mathrm{SW}} + [\mathrm{Ne}]_{\mathrm{cos}} + [\mathrm{Ne}]_{\mathrm{trap}})$,

$f_{\mathrm{cos}} = [\mathrm{Ne}]_{\mathrm{cos}}/([\mathrm{Ne}]_{\mathrm{SW}} + [\mathrm{Ne}]_{\mathrm{cos}} + [\mathrm{Ne}]_{\mathrm{trap}})$, and

$f_{\mathrm{trap}} = [\mathrm{Ne}]_{\mathrm{trap}}/([\mathrm{Ne}]_{\mathrm{SW}} + [\mathrm{Ne}]_{\mathrm{cos}} + [\mathrm{Ne}]_{\mathrm{trap}})$.

Table S26: The cosmogenic-^{21}Ne abundances and cosmic-ray exposure ages of the TD1 samples.

	A0022-2	A0033-12	A0033-13	A0033-14	A0035-7	A0035-11	A0035-8	A0035-10	A0048-2	A0073-2	A0078-11	A0085-2
$[^{21}\mathrm{Ne}]_{\mathrm{cos}}$ (10^{-8} ccSTP $\cdot$ g^{-1})												
Option 1	0.49 (0.12)		0.39 (0.11)	0.55 (0.09)	0.14 (0.03)	0.14 (0.11)	0.17 (0.04)	0.18 (0.04)	0.36 (0.08)	1.09 (0.21)	0.10 (0.90)	0.56 (0.09)
Option 2	0.49 (0.12)		0.39 (0.11)	0.55 (0.09)	0.14 (0.03)	0.14 (0.11)	0.17 (0.04)	0.18 (0.04)	0.36 (0.08)	1.09 (0.20)	0.10 (0.89)	0.55 (0.09)
Option 3	0.49 (0.12)		0.38 (0.11)	0.54 (0.09)	0.13 (0.03)	0.13 (0.11)	0.17 (0.04)	0.18 (0.04)	0.36 (0.08)	1.08 (0.20)	0.07 (0.88)	0.55 (0.08)
Option 4	0.49 (0.12)		0.38 (0.11)	0.54 (0.09)	0.13 (0.03)	0.13 (0.11)	0.17 (0.04)	0.18 (0.04)	0.36 (0.08)	1.08 (0.20)	0.07 (0.88)	0.55 (0.08)
Option 5	0.49 (0.12)		0.38 (0.11)	0.54 (0.09)	0.13 (0.03)	0.13 (0.11)	0.17 (0.04)	0.18 (0.04)	0.36 (0.08)	1.08 (0.20)	0.07 (0.88)	0.55 (0.08)
Option 6	0.49 (0.12)		0.38 (0.11)	0.54 (0.09)	0.13 (0.03)	0.13 (0.11)	0.17 (0.04)	0.18 (0.04)	0.36 (0.08)	1.08 (0.20)	0.07 (0.88)	0.55 (0.08)
Option 7	0.49 (0.12)		0.38 (0.11)	0.54 (0.09)	0.13 (0.03)	0.13 (0.11)	0.17 (0.04)	0.18 (0.04)	0.36 (0.08)	1.08 (0.20)	0.07 (0.88)	0.55 (0.08)
Option 8	0.49 (0.12)		0.38 (0.11)	0.54 (0.09)	0.13 (0.03)	0.13 (0.11)	0.17 (0.04)	0.18 (0.04)	0.36 (0.08)	1.08 (0.20)	0.07 (0.88)	0.55 (0.08)
T_{CRE} (10^6 years)												
Option 1	2.5 (0.6)		1.9 (0.6)	2.8 (0.5)	0.68 (0.16)	0.69 (0.57)	0.86 (0.20)	0.92 (0.19)	1.8 (0.4)	5.5 (1.0)	0.5 (4.5)	2.8 (0.4)
Option 2	3.7 (0.9)		2.9 (0.8)	4.1 (0.7)	1.0 (0.2)	1.0 (0.9)	1.3 (0.3)	1.4 (0.3)	2.7 (0.6)	8.2 (1.5)	0.7 (6.7)	4.1 (0.7)
Option 3	3.8 (0.9)		3.0 (0.9)	4.2 (0.7)	1.0 (0.2)	1.0 (0.9)	1.3 (0.3)	1.4 (0.3)	2.8 (0.6)	8.3 (1.6)	0.6 (6.8)	4.2 (0.7)
Option 4	3.6 (0.8)		2.8 (0.8)	4.0 (0.7)	0.98 (0.23)	0.97 (0.82)	1.2 (0.3)	1.3 (0.3)	2.6 (0.6)	7.9 (1.5)	0.5 (6.5)	4.0 (0.6)
Option 5	3.7 (0.9)		2.9 (0.8)	4.1 (0.7)	1.01 (0.24)	0.99 (0.85)	1.3 (0.3)	1.4 (0.3)	2.7 (0.6)	8.1 (1.5)	0.5 (6.6)	4.1 (0.6)
Option 6	3.3 (0.8)		2.6 (0.7)	3.6 (0.6)	0.89 (0.21)	0.88 (0.75)	1.1 (0.3)	1.2 (0.3)	2.4 (0.5)	7.2 (1.4)	0.5 (5.9)	3.6 (0.6)
Option 7	3.7 (0.9)		2.9 (0.8)	4.1 (0.7)	1.0 (0.2)	0.99 (0.85)	1.3 (0.3)	1.4 (0.3)	2.7 (0.6)	8.1 (1.5)	0.5 (6.6)	4.1 (0.6)
Option 8	7.4 (1.8)		5.8 (1.7)	8.3 (1.5)	2.0 (0.5)	2.0 (1.7)	2.5 (0.6)	2.7 (0.6)	5.4 (1.2)	16 (3)	1 (13)	8.3 (1.4)

$[^{21}\mathrm{Ne}]_{\mathrm{cos}}$ (cosmogenic ^{21}Ne abundances) and cosmic-ray exposure ages (T_{CRE}) are calculated for the shielding-depth options 1–8 (Table S22).

Table S27: The cosmogenic-^{21}Ne abundances and cosmic-ray exposure ages of the TD2 samples.

	C0008-5	C0008-5 (2nd)	C0019-2	C0027-2	C0039-2	C0047-2	C0047-3	C0053-5	C0079-2	C0081-6	C0082-2
$[^{21}\mathrm{Ne}]_{\mathrm{cos}}$ (10^{-8} ccSTP $\cdot$ g^{-1})											
Option 1	0.47 (0.08)	0.37 (0.06)	0.46 (0.07)	0.44 (0.06)	0.35 (0.12)	0.82 (0.16)	0.59 (0.08)	0.45 (0.09)	0.27 (0.05)	0.33 (0.04)	0.30 (0.07)
Option 2	0.47 (0.08)	0.37 (0.06)	0.46 (0.07)	0.44 (0.06)	0.35 (0.12)	0.82 (0.16)	0.59 (0.08)	0.45 (0.09)	0.26 (0.05)	0.32 (0.04)	0.30 (0.07)
Option 3	0.47 (0.08)	0.37 (0.05)	0.45 (0.07)	0.44 (0.06)	0.35 (0.12)	0.82 (0.16)	0.59 (0.08)	0.45 (0.09)	0.26 (0.05)	0.32 (0.04)	0.30 (0.07)
Option 4	0.47 (0.08)	0.37 (0.05)	0.45 (0.07)	0.44 (0.06)	0.35 (0.12)	0.82 (0.16)	0.58 (0.08)	0.45 (0.09)	0.26 (0.05)	0.32 (0.04)	0.30 (0.07)
Option 5	0.47 (0.08)	0.37 (0.05)	0.45 (0.07)	0.44 (0.06)	0.35 (0.12)	0.81 (0.16)	0.58 (0.08)	0.45 (0.09)	0.26 (0.05)	0.32 (0.04)	0.30 (0.07)
Option 6	0.47 (0.08)	0.37 (0.05)	0.45 (0.07)	0.44 (0.06)	0.35 (0.12)	0.81 (0.16)	0.58 (0.08)	0.44 (0.09)	0.26 (0.05)	0.32 (0.04)	0.30 (0.07)
Option 7	0.47 (0.08)	0.37 (0.05)	0.45 (0.07)	0.44 (0.06)	0.35 (0.12)	0.81 (0.16)	0.58 (0.08)	0.44 (0.09)	0.26 (0.05)	0.32 (0.04)	0.30 (0.07)
Option 8	0.47 (0.08)	0.37 (0.05)	0.45 (0.07)	0.44 (0.06)	0.35 (0.12)	0.81 (0.16)	0.58 (0.08)	0.44 (0.09)	0.26 (0.05)	0.32 (0.04)	0.30 (0.07)
T_{CRE} (10^{6} years)											
Option 1	2.4 (0.4)	1.9 (0.3)	2.3 (0.4)	2.2 (0.3)	1.8 (0.6)	4.1 (0.8)	3.0 (0.4)	2.3 (0.4)	1.3 (0.2)	1.6 (0.2)	1.5 (0.4)
Option 2	3.5 (0.6)	2.8 (0.4)	3.4 (0.6)	3.3 (0.4)	2.6 (0.9)	6.2 (1.2)	4.4 (0.6)	3.4 (0.7)	2.0 (0.4)	2.4 (0.3)	2.3 (0.6)
Option 3	3.6 (0.6)	2.8 (0.4)	3.5 (0.6)	3.4 (0.5)	2.7 (0.9)	6.3 (1.2)	4.5 (0.6)	3.4 (0.7)	2.0 (0.4)	2.5 (0.3)	2.3 (0.6)
Option 4	3.4 (0.5)	2.7 (0.4)	3.3 (0.5)	3.2 (0.4)	2.6 (0.9)	6.0 (1.2)	4.3 (0.6)	3.3 (0.6)	1.9 (0.4)	2.4 (0.3)	2.2 (0.5)
Option 5	3.5 (0.6)	2.8 (0.4)	3.4 (0.6)	3.3 (0.4)	2.6 (0.9)	6.1 (1.2)	4.4 (0.6)	3.3 (0.7)	2.0 (0.4)	2.4 (0.3)	2.3 (0.5)
Option 6	3.1 (0.5)	2.5 (0.4)	3.0 (0.5)	2.9 (0.4)	2.3 (0.8)	5.4 (1.1)	3.9 (0.5)	3.0 (0.6)	1.7 (0.3)	2.1 (0.3)	2.0 (0.5)
Option 7	3.5 (0.6)	2.8 (0.4)	3.4 (0.6)	3.3 (0.4)	2.6 (0.9)	6.1 (1.2)	4.4 (0.6)	3.3 (0.7)	2.0 (0.4)	2.4 (0.3)	2.3 (0.5)
Option 8	7.1 (1.2)	5.6 (0.9)	6.9 (1.0)	6.7 (1.0)	5.3 (1.9)	12 (3)	8.9 (1.3)	6.8 (1.4)	4.0 (0.8)	4.9 (0.7)	4.5 (1.1)

$[^{21}\mathrm{Ne}]_{\mathrm{cos}}$ (cosmogenic ^{21}Ne abundances) and cosmic-ray exposure ages (T_{CRE}) are calculated for the shielding-depth options 1–8 (Table S22).